

## Large Scale Structure at 24 Microns from Counts-in-Cells in the SWIRE Survey

Frank J. Masci<sup>1,2</sup>, Fan Fang<sup>1,2</sup>, Tracey Evans<sup>2</sup>, David L. Shupe<sup>1,2</sup>, Russ Laher<sup>1,2</sup>, Michael Rowan-Robinson<sup>3</sup>, Tom Babbedge<sup>3</sup>, Mattia Vaccari<sup>3</sup>, Maria Polletta<sup>5</sup>, Sebastian Oliver<sup>4</sup>, Kevin C. Xu<sup>2</sup>, Ian Waddington<sup>4</sup>, Eduardo Gonzalez-Solares<sup>6</sup>, Carol J. Lonsdale<sup>2</sup>, Jason A. Surace<sup>1,2</sup>, Deborah Padgett<sup>1,2</sup>, Harding E. Smith<sup>5</sup>

fmasci@ipac.caltech.edu

### ABSTRACT

We explore the projected distribution of galaxy *counts-in-cells* at 24 microns in three fields of the *Spitzer* Wide-area InfraRed Extragalactic (SWIRE) program: ELAIS-N1 (EN1), ELAIS-N2 (EN2) and a subregion in the Lockman-Hole (LH) field. The samples cover contiguous areas of respectively  $\simeq 8.62$ ,  $3.98$  and  $6.60$  deg<sup>2</sup> and contain 12040, 4979 and 8633 sources detected at  $24\mu\text{m}$  to a mean  $\simeq 9\sigma$  limit of  $450\mu\text{Jy}$ . Counts are performed in circular cells of angular diameter  $0^\circ.05$  to  $0^\circ.7$  corresponding to comoving spatial scales of  $\simeq 1.8\text{--}26h^{-1}\text{Mpc}$  at the expected median redshift of  $z \simeq 0.9$ . Statistics are analyzed in full samples and subsamples defined by flux-density ratio cuts:  $f_{24\mu\text{m}}/f_{3.6\mu\text{m}} \leq 5.5$  and  $\geq 6.5$ , which are referred to as the *blue* and *red* subsamples respectively. The count distributions fit the form predicted by the quasi-equilibrium gravitational clustering model with values of the virialization parameter  $b = -W/2K$  approaching 0.42-0.55 on the largest scales probed, consistent with studies in the

---

<sup>1</sup>*Spitzer* Science Center, California Institute of Technology, 220-6, Pasadena, CA, 91125

<sup>2</sup>Infrared Processing and Analysis Center, California Institute of Technology, 100-22, Pasadena, CA, 91125

<sup>3</sup>Astrophysics Group, Blackett Laboratory, Imperial College London, Prince Consort Road, London SW7 2BW, UK

<sup>4</sup>Astronomy Centre, CPES, University of Sussex, Falmer, Brighton BN1 9QJ, UK

<sup>5</sup>Center for Astrophysics and Space Sciences, University of California, San Diego, La Jolla, CA 92093-0424, USA

<sup>6</sup>Institute of Astronomy, Madingley Road, Cambridge CB3 0HA

optical. We also measure the angular variance and skewness from the galaxy distributions and from these, estimate *area-averaged* two and three-point correlation functions:  $\bar{w}_2(\theta)$  and  $\bar{w}_3(\theta)$  respectively. The “cosmic variance” in clustering strength amongst the three fields, as measured by the relative RMS deviation in  $\bar{w}_2(\theta)$  is  $\simeq 18\%$ . Statistically significant non-Poisson and non-Gaussian behavior is seen on all scales  $\geq 0'.1$  where both positive and negative skewnesses are detected. For the EN1 field only, the skewness and variance marginally satisfy the prediction for hierarchical gravitational clustering in the linear to mildly non-linear regime,  $\bar{w}_3(\theta) = S_3 \bar{w}_2^2(\theta)$ , where  $S_3 = 3.3 \pm 1.2$  independent of scale. The skewness estimates are too noisy and unreliable in the EN2 and LH fields to test this prediction. The traditional power-law fit parameters to the differential two-point function,  $w_2(\theta) = A\theta^{1-\gamma}$ , are estimated from an inversion of the area-averaged functions. We find that the blue subsamples have amplitudes ( $A$ ) greater by factors of 1.5-20 than the red or full samples. This is consistent with the blue galaxies being located predominately at low- $z$ , where dilution to their three-dimensional clustering by projections is diminished. Using model redshift distributions consistent with source counts, and assuming stable clustering, we invert Limber’s equation and find spatial comoving correlation lengths of  $r_0 \simeq 4.35$  to  $4.86 h^{-1}$  Mpc across all fields. Overall, the  $r_0$  values for  $24\mu\text{m}$  selected galaxies are smaller than those derived from optical surveys, but in agreement with results from IRAS and ISO in the mid-infrared. This extends the notion to higher redshifts that infrared selected surveys show weaker clustering than optical surveys.

*Subject headings:* galaxies: statistics — infrared: galaxies — surveys — large-scale structure of universe.

## 1. Introduction

The large scale structure (LSS) of the Universe is believed to be determined by physical processes that took place long before recombination. A simple case is that in which the density fluctuations are approximated by a random Gaussian process. According to the classical inflationary scenario, Gaussian perturbations are expected to originate from quantum fluctuations of a scalar field with a variance which is scale invariant (e.g., Olive 1990, and references therein). This picture is consistent with recent measurements of the Cosmic Microwave Background (CMB) with WMAP (Spergel et al. 2003; Komatsu et al. 2003) where non-Gaussian primordial fluctuation models are ruled out with a high degree of confidence. Even without inflation, the Central Limit Theorem guarantees that the superposition

of a large number of random processes in the early Universe will be Gaussian distributed. As perturbations grow by gravitational instability, an initially Gaussian distribution will remain Gaussian as long as the fluctuations remain in the linear regime where  $\delta\rho/\rho \ll 1$ . Once non-linear effects become important (e.g., gravitational collapse and star formation), the distribution will deviate from its initial Gaussian state. Evolution to a non-Gaussian distribution is also expected in the framework of “biased” models of galaxy formation (Kaiser 1984; Bardeen et al. 1986), where galaxies are identified with those peaks of the underlying Gaussian matter distribution which exceed some threshold. One therefore hopes that observations of LSS to intermediate redshifts can be used to constrain physical conditions in the early Universe and its development to non-Gaussianity in the galaxy distribution.

The traditional two-point correlation function estimator,  $\xi_2$ , has been used extensively to quantify the clustering pattern of galaxies (Peebles 1980). This is related to the second moment (or variance) of the corresponding galaxy count distribution. This estimator is limited in that it exhausts only the statistical content of a distribution which is purely Gaussian in nature. To measure higher-order statistics and characterize non-Gaussianity as predicted by non-linear growth of structure, a more general method is needed. The method of counts-in-cells (Hubble 1934; White 1979; Bernardeau et al. 2002) provides the full galaxy count distribution function within a cell of given size (either in volume or projected on the sky) from which all higher-order moments and  $n$ -point correlations can be derived. Its normalized version, the galaxy count probability distribution function (CPDF) gives the probability of finding  $N$  galaxies in a randomly placed cell. Numerous authors have used moments of the CPDF to gain more accurate information on the higher-order correlations  $\xi_n$  (Balian & Schaeffer 1989; Saunders et al. 1991; Coles & Frenk 1991; Szapudi et al. 1992; Gaztañaga 1994). These studies calculated the second and third moments of the number density, showing that scaling relations between them are consistent with the expectations of a gravitational clustering hierarchy, i.e., the so called hierarchical model where  $\bar{\xi}_n \propto \bar{\xi}_2^{n-1}$ . The moments of the CPDF are related to volume-averaged ( $\bar{\xi}_n$ ) or in the case of a projected catalogue, area-averaged  $n$ -point correlation functions ( $\bar{w}_n$ ). These can be inverted to obtain the  $n$ -point amplitude, smoothed on a scale defined by the CPDF cell size. The advantages of using the CPDF to infer  $n$ -point statistics over traditional direct binning methods (e.g., which compute the two-point estimator) are that first, the data do not require binning; second, the CPDF method has better signal-to-noise ratio properties, since statistics are generally better when sampled and averaged over larger regions; third, no random comparison sample is needed; and fourth, systematic effects from catalogue boundaries and finite sampling, i.e., the “integral constraint” bias, are more easily handled (e.g., Infante 1994).

Various authors have explored models to describe the observed galaxy CPDF. Saslaw & Hamilton (1984, hereafter SH84) constructed a discrete thermodynamic model of the CPDF

parameterized in terms of the ratio  $b = -W/2K$ , representing the volume-averaged gravitational correlation energy to kinetic energy of peculiar velocities in a gravitating system. Other theoretical distributions are the discrete negative-binomial model (Carruthers & Shih 1983), a hierarchical scaling ansatz (Schaeffer 1985), the lognormal distribution (Coles & Jones 1991) and the Edgeworth expansion representation (Juszkiewicz et al. 1995). See Borgani (1996) for a review of their strengths and weaknesses. Due to the widespread success of the SH84 model in representing the observed CPDF of galaxies in optical and infrared surveys (e.g., Sheth et al. 1994), we primarily use this model to compare with the results of previous studies.

Galaxy surveys at optical and infrared wavelengths have revealed the rich structure of the local Universe on large scales through the two-point correlation function estimator, or equivalently its power spectrum: e.g., CfA (Huchra et al. 1983); APM, (Maddox et al. 1990); EDSGC, (Szapudi et al. 1996); 2dFGRS (Colless et al. 2001; Peacock 2003); and IRAS, (Fisher et al. 1994; Saunders et al. 1992; Bouchet et al. 1993). Interestingly, it was found that the Root Mean Square (RMS) fluctuation in the distribution of IRAS galaxies on  $8h^{-1}\text{Mpc}$  scales is smaller than that of optically selected galaxies by a factor  $\sim 0.65$  (Moore et al. 1994). This is also consistent with the finding that infrared galaxies have smaller correlation lengths on average than in the optical. By computing the spatial variance from galaxy counts-in-cells, Efstathiou et al. (1990) were able to rule out the standard ( $\Omega = 1$ ) cold dark matter model to a high degree of confidence. More recently, analysis of galaxy clustering is being extended to redshifts  $z \simeq 0.5 - 1$  in the optical with the SDSS (York et al. 2000; Zehavi et al. 1994) and the near-infrared ( $3.6\text{-}8.0\mu\text{m}$ ) with *Spitzer* (Fang et al. 2004; Oliver et al. 2004; Waddington et al. 2005). Gonzalez-Solares et al. (2004) provided a first estimate of clustering in the mid-infrared ( $15\mu\text{m}$ ) from the ELAIS-S1 survey with ISO to a median redshift of  $z \simeq 0.2$ . Their results are consistent with the IRAS findings. Deeper surveys are now being conducted in the mid-infrared ( $24\mu\text{m}$ ) with *Spitzer* to allow studies of the distribution of infrared-luminous galaxies to redshifts  $z \simeq 1.5$ .

The *Spitzer* Wide-area Infrared Extragalactic legacy program (SWIRE; Lonsdale et al. 2003, 2004) is one such survey. This is expected to detect over two million galaxies at infrared wavelengths from  $3.6$  to  $160\mu\text{m}$  over six fields covering  $49\text{ deg}^2$ . The survey is intended to study galaxy evolution, the history of star formation and accretion processes, and due to its large sampled volume, how these are influenced by galaxy clustering and environment on all scales. We focus on three fields in this study: the ELAIS-N1 (EN1), ELAIS-N2 (EN2) and a contiguous region in the Lockman-Hole (LH) field. The EN1 and EN2 fields were originally part of the European Large-Area ISO program (Rowan-Robinson et al. 1999) and cover  $\simeq 8.62$  and  $\simeq 3.98\text{ deg}^2$  respectively. The LH sub-field used in this study covers  $\simeq 6.60\text{ deg}^2$  and was originally discovered by Lockman et al. (1986) to contain the smallest

known amount of galactic HI, making it ideal for extragalactic observations. These are the first SWIRE fields containing the largest validated multi-wavelength imaged regions: from high quality ground-based imaging in the optical ( $U, g', r', i', Z$ ), to imaging with *Spitzer* in the IRAC and MIPS bands (3.6, 4.5, 5.8, 8.0, 24, 70 and  $160\mu\text{m}$ ). Shupe et al. (2005) presented a detailed analysis of  $24\mu\text{m}$  galaxy counts in the EN1 field, and by performing counts in subfields of  $\simeq 1.5 \text{ deg}^2$ , found that the Euclidean-normalized counts varied by at least 10% at flux densities  $\gtrsim 1 \text{ mJy}$ . Significant “cosmic variance” was also seen by comparing these counts to those from other fields (e.g., Marleau et al. 2004; Papovich et al. 2004). These discrepancies are most likely due to the effects of galaxy clustering on large scales.

In this paper, we present initial results of galaxy clustering at  $24\mu\text{m}$  by analyzing statistics of the projected galaxy distribution using the *counts-in-cells* method. This study is the first of its kind at this wavelength and sensitivity, reaching a factor of  $\simeq 700$  deeper in flux density than the IRAS  $25\mu\text{m}$  galaxy surveys. We explore clustering statistics as a function of  $3.6\text{--}24\mu\text{m}$  color and explore their variation across three separate fields to estimate the level of cosmic variance. We compare distributions of counts-in-cells with the quasi-equilibrium gravitational clustering model of SH84 and constrain the dimensionless parameter  $b = -W/2K$  as a function of angular scale. We focus on the second and third moments of the galaxy distribution (variance and skewness) and use these to test qualitatively the hierarchical model. We estimate two-point correlation amplitudes from a power-law inversion of the angular-averaged variance from counts-in-cells that uses the full error-covariance matrix between angular bins. These are then deprojected using model redshift distributions and Limber’s (Limber 1953) equation to obtain estimates of three-dimensional clustering for all samples.

This paper is organized as follows. § 2 describes the observations, samples, completeness and star-galaxy separation. § 3 presents a summary of the counts-in-cells method, statistical measures and error estimation. § 4 presents counts-in-cells results, an analysis of systematics from finite sampling, and distribution function model fits. § 5 presents results of power-law fits to the angular two-point correlation function for all samples and compares the two and three-point angular-averaged statistics to predictions of the hierarchical model. § 6 presents the deprojection of our angular two-point statistics to infer the three-dimensional clustering, and results are discussed and compared to previous studies. A summary and concluding remarks are given in § 7. We assume a spatially flat Friedmann-Robertson Walker Cosmology throughout with  $\Omega_m = 0.3$  and  $\Omega_\Lambda = 0.7$ . Unless otherwise stated, Hubble’s constant is scaled according to  $h = H_0/100 \text{ km s}^{-1} \text{ Mpc}^{-1}$ .

## 2. Observations, Processing and Sample Selection

The SWIRE EN1, EN2, and LH (sub-region) fields are centered at (RA, Dec; J2000) =  $(16^h11^m15^s, 55^\circ4'24'')$ ;  $(16^h36^m36^s, 40^\circ59'11'')$  and  $(10^h42^m23^s, 58^\circ21'21'')$  respectively, and by design, are located in regions of moderately low cirrus noise and background where  $I_{100\mu\text{m}} \lesssim 0.5 \text{MJy sr}^{-1}$  (Lonsdale et al. 2003). These fields were observed with the Multi-band Imaging Photometer for *Spitzer* (MIPS) and the InfraRed Array Camera (IRAC) instruments during 2004 January, 2004 July, and 2004 April-May respectively. The MIPS and IRAC instrument performances are described by Rieke et al. (2004) and Fazio et al. (2004) respectively. The nominal coverage (redundancy) per pixel for the MIPS-24 $\mu\text{m}$  observations is 40, although it varied from about 30 at the boundaries to a maximum of 74 over the central regions of the fields (see Figure 1). This gave a nominal total integration of 160 s per pointing, yielding a *nominal* 24 $\mu\text{m}$  RMS sensitivity of  $\simeq 56\mu\text{Jy}$ . All Basic Calibrated image Data (BCD) products are available from the *Spitzer* Science Center (SSC) Archive under programs (PIDs) 185, 183 and 142 for EN1, EN2 and LH respectively. All full field mosaics, bandmerged *Spitzer* data and optical cross-identifications are available from the *Spitzer* popular products archive<sup>7</sup>. The data used in this paper comprise the second incremental release of SWIRE products. A description of all products, data processing and analysis is given in Surace et al. (2005).

### 2.1. Selection Function, Completeness and Reliability

We distinguish between two types of “selection function” which we quantify in terms of the completeness of a sample. First, that introduced by the finite resolution of a detector and other instrumental signatures or artifacts affecting source detection (e.g., bad pixels, bright stars) and second, that due to the flux limit of the sample which limits detectability across the full luminosity range as a function of redshift. The latter is important for estimates of spatial clustering and will be considered in § 6. In this section, we focus on the instrumental limitations.

The relatively small (0.86 m) size of the *Spitzer* primary mirror limits the spatial resolution to relatively large beams compared to ground-based telescopes. The beamsize at 24 $\mu\text{m}$  is 5.8 $''$ . Confusion due to overlapping beams of unresolved faint sources therefore becomes a significant source of incompleteness. The completeness level of the initially extracted 24 $\mu\text{m}$  samples was estimated using the EN1 field where 130,000 simulated sources were added to a

---

<sup>7</sup><http://data.spitzer.caltech.edu/popular/swire/>

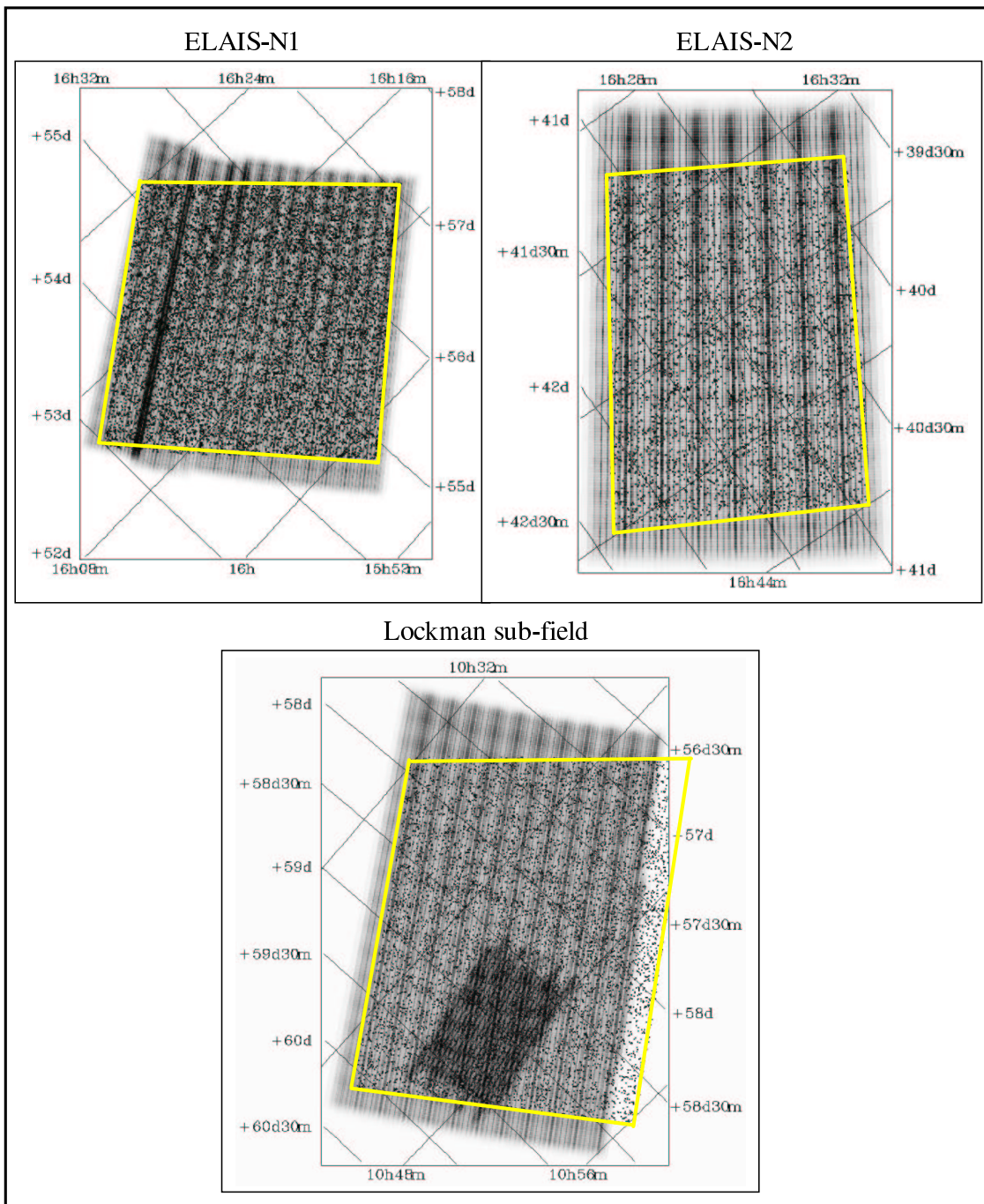


Fig. 1.—  $24\mu\text{m}$  coverage maps and geometries for three SWIRE fields: ELAIS-N1 (EN1), ELAIS-N2 (EN2) and a subfield of the Lockman-Hole (LH) field. The  $3.6\text{--}24\mu\text{m}$  bandmerged sources (shown as dots) are selected from regions enclosed by the grey boundaries where the coverage is  $\gtrsim 37$  pixels. Dark striped patterns correspond to coverages of  $\gtrsim 60$  and the brightest stripes to coverages of  $\lesssim 47$ . The full LH field is actually composed of two mosaics and only the coverage-map containing the largest contiguous portion is shown.

high coverage  $5.34 \text{ deg}^2$  central region. This number of sources corresponds to  $\simeq 200$  beams per source. These sources were then extracted using the SExtractor software with a Gaussian filter (which was found to be more robust against spurious detections) and matched against the input simulated list (see Shupe et al. 2005, for details of the method). The fraction of simulated sources recovered with flux densities  $\geq 450 \mu\text{Jy}$  ( $\simeq 9\sigma$ ) was  $> 99\%$ . This is consistent with comparisons to counts in two deeper fields within EN1 where the fainter SWIRE sources are detected with much higher confidence. One was taken as part of the *Spitzer* Extragalactic First Look Survey (FLS) program (Marleau et al. 2004) and covers 54 square arcminutes to a depth of  $\simeq 90 \mu\text{Jy}$  (scaled to  $9\sigma$ ), and another is the *Spitzer*-GOODS Validation Field covering 165 square arcminutes to  $\simeq 54 \mu\text{Jy}$  ( $9\sigma$ ). There is very good agreement between the fluxes from all studies down to  $200 \mu\text{Jy}$  ( $\simeq 4\sigma$  for SWIRE), where the completeness from our simulation was  $\gtrsim 90\%$ .

Any significant variation in the completeness on scales of interest will manifest itself as an artificial clustering signal. Variations in sky coverage lead to fluctuations in local noise, thus affecting source detectability and reliability. Given our high completeness level however, we can be confident that it is also uniform (on average) across each of the fields. For all fields, the  $24 \mu\text{m}$  detections were limited to regions with coverages of  $\gtrsim 37$  pixels as defined by the dashed boundaries in Figure 1. Of all  $24 \mu\text{m}$  detections in the EN1 field for example,  $\simeq 98.5\%$  were found to be centered on coverages with  $\gtrsim 40$  pixels. The effective RMS noise over these regions for a coverage of  $N_c$  pixels scales as  $\sigma \simeq 50 \sqrt{50/N_c} \mu\text{Jy}$ . For a coverage range  $37 \lesssim N_c \lesssim 73$ , our  $450 \mu\text{Jy}$  flux limit therefore implies a SNR range of  $7.7 \lesssim \text{SNR} \lesssim 10.8$ , with a mean of  $\simeq 9\sigma$  corresponding to  $\langle N_c \rangle \simeq 50$  pixels. We have therefore adopted a simple but conservative selection function. Our  $450 \mu\text{Jy}$  flux limit shows that even in regions of higher than average noise (low coverage), the minimum SNR of  $\simeq 7.7$  still puts us at a very high completeness level where most detections can be considered reliable (see below) and independent of position in our maps.

As evaluated by Shupe et al. (2005) for the EN1 field, and as discussed in the SWIRE Second Data Release document (Surace et al. 2005), the spurious (unreliable) source fraction is expected to be  $\lesssim 0.5\%$  at  $f_{24 \mu\text{m}} \geq 450 \mu\text{Jy}$ . In fact, to minimize the incidence of spurious (unreliable)  $24 \mu\text{m}$  extractions, we have retained only those  $24 \mu\text{m}$  sources which were also detected by IRAC at  $3.6 \mu\text{m}$  above a flux limit of  $10 \mu\text{Jy}$ . This limit corresponds to  $\text{SNR} \simeq 10\sigma$  in the lowest coverage (noisiest) regions of the IRAC maps, and the overall noise range is  $0.63 \lesssim (\sigma/\mu\text{Jy}) \lesssim 1.00$  (Surace et al. 2005). The fraction of  $24 \mu\text{m}$  sources with multiple  $3.6 \mu\text{m}$  matches was very low ( $\simeq 0.07\%$  in EN1). The  $24\text{-}3.6 \mu\text{m}$  bandmerge reliability was estimated from cumulative distributions of positional offsets (Surace et al. 2005). For over  $99\%$  of the merges with fluxes greater than the limits quoted above, matches within  $3''$  can be considered reliable. In the EN1 field, the fraction of initially extracted  $24 \mu\text{m}$  sources

with *no*  $3.6\mu\text{m}$  detection (which were eventually discarded) in the IRAC+MIPS mapped common-overlap region was  $\simeq 0.17\%$ .

## 2.2. Star-Galaxy Separation

Stars will weaken the inferred galaxy clustering signal and must be removed. Stars are not expected to be a major contributor in our samples since all fields are located at moderately high galactic latitudes:  $42^\circ \lesssim b \lesssim 52^\circ$ . The stellar contamination is also expected to be low at  $24\mu\text{m}$  since we are sampling the Rayleigh-Jeans tail of the spectral energy distribution of most stars. Conservatively speaking, the dominant stellar population has effective photospheric temperatures  $> 2000$  K, corresponding to peak wavelengths  $\lesssim 2.5\mu\text{m}$  (e.g., Lada 1987). For  $T > 2000$  K, Rayleigh-Jeans scaling predicts a flux density ratio  $f_\nu(24\mu\text{m})/f_\nu(3.6\mu\text{m}) < 0.06$ , although we cannot rule out the possibility of excess non-photospheric emission (e.g., by dust), however low, at mid-infrared wavelengths, thereby increasing this ratio. Radiative transfer calculations by Kurosawa et al. (2004) do indeed indicate that near-to-mid-infrared colors can be substantially redder by an order of magnitude than blackbody predictions. Conservatively speaking, even assuming blackbody temperatures  $T > 2000$  K and our sample limit of  $f(24\mu\text{m}) \simeq 450\mu\text{Jy}$  predicts  $3.6\mu\text{m}$  flux densities  $\gtrsim 7300\mu\text{Jy}$  (see bottom panel in Figure 2), well above our  $3.6\mu\text{m}$  detection limit used to ensure reliability. Stellar contamination in our samples therefore cannot be ruled out.

We have used two criteria based on the flux density ratio  $C = f_\nu(24\mu\text{m})/f_\nu(3.6\mu\text{m})$ ,  $3.6\mu\text{m}$  flux density, and  $3.6\mu\text{m}$  stellarity index to classify and flag potential stellar candidates:

$$C \leq 0.5 \quad \& \quad f_\nu(3.6\mu\text{m}) \geq 500\mu\text{Jy} \quad \& \quad 3.6\mu\text{m stellarity} \geq 0.9 \quad (1)$$

or

$$C \leq 3.8 \quad \& \quad f_\nu(24\mu\text{m}) \geq 7 \times 10^3\mu\text{Jy}. \quad (2)$$

Criterion 1 uses the  $3.6\mu\text{m}$  stellarity index as output by the SExtractor software. This ranges from 0.0 for significantly extended sources to 1.0 for those with perfectly stellar Point Spread Functions (PSFs). We picked a threshold of 0.9. Figure 2 shows the ratio  $C$  as a function of  $3.6\mu\text{m}$  and  $24\mu\text{m}$  flux densities for the EN1 field. From an examination of the distribution of sources in these diagrams, we see that there are two distinct populations, one of which we declare to be stars from visual examination. Coupled with the stellarity index in criterion 1, we also find that the populations can be more-or-less separated by the further criteria:  $C \leq 0.5$  and  $f_\nu(3.6\mu\text{m}) \geq 500\mu\text{Jy}$ . These are in accord with expectations for the general stellar population discussed earlier.

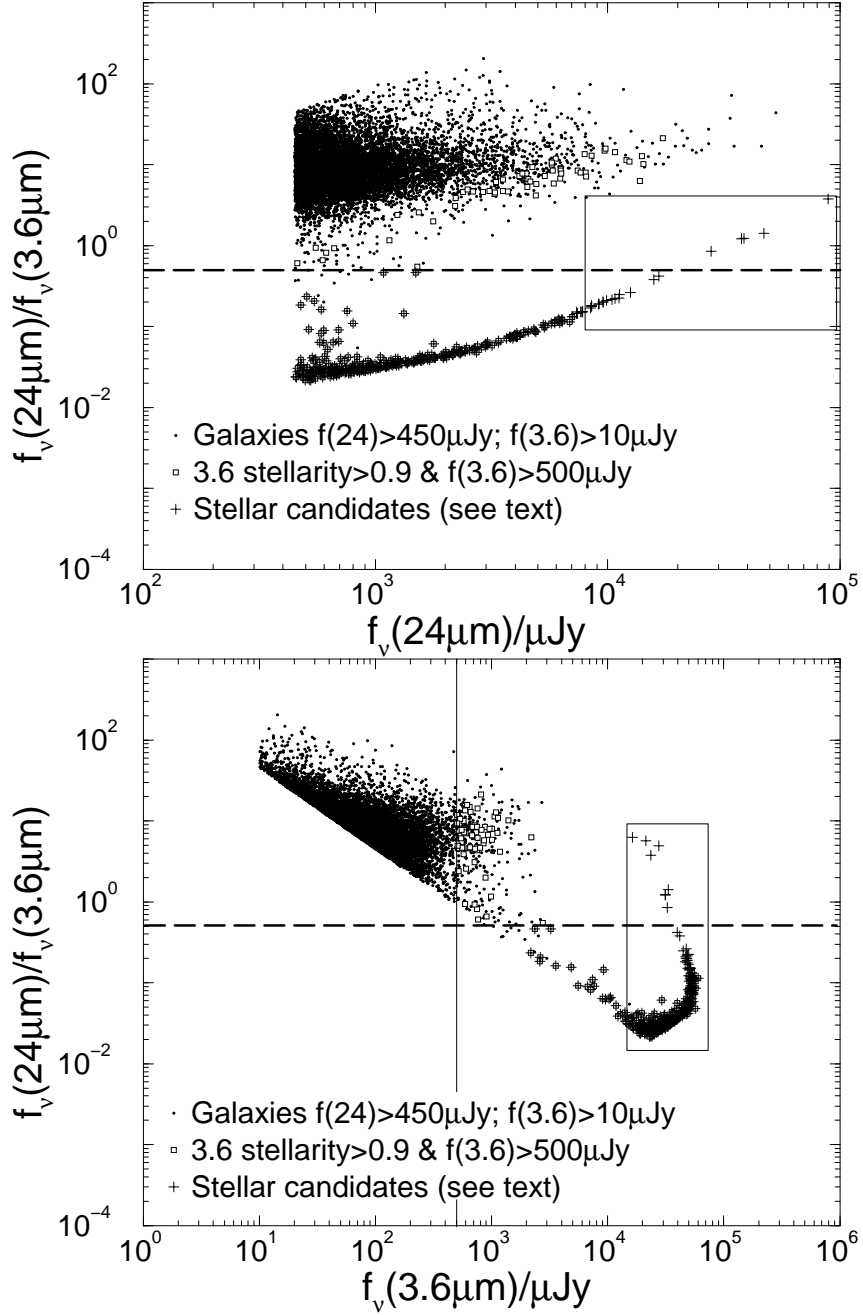


Fig. 2.— Ratio of flux densities  $f_{24}/f_{3.6}$  versus  $24\mu\text{m}$  flux density (*top*) and  $3.6\mu\text{m}$  flux density (*bottom*) for the EN1 field. Sources marked with a “+” are flagged as stellar (see § 2.2). Dashed horizontal lines represent  $f_{24}/f_{3.6} = 0.5$ , the vertical solid line in the bottom panel represents  $f_{\nu}(3.6\mu\text{m}) = 500\mu\text{Jy}$  and the boxes delineate those sources near or at the  $3.6\mu\text{m}$  saturation limit which renders the stellerity index unreliable. These sources are identified as stars on visual examination.

We find that the  $3.6\mu\text{m}$  stellarity index correlates strongly with flux density in our samples, but the stellarity becomes unreliable for sources at or near the  $3.6\mu\text{m}$  saturation limit. SExtractor classifications become degenerate when attempting to separate these from extended sources. These sources are delineated by boxes in Figure 2 and are at the bright end of flux distribution. On visual examination, these sources are identified with bonafide stars. Such sources are found to satisfy Criterion 2. We have fine tuned the stellar criteria (1 and 2) using predominately data from EN1 since this is the largest of all fields with good  $3.6\text{-}24\mu\text{m}$  bandmerge statistics. Excellent independent agreement was found using data from the EN2 and LH fields.

The small squares in Figure 2 indicate those sources which only satisfy the second two conditions in Criterion 1 (i.e., with no cut on  $C$ ). Such sources are likely to include a large proportion of galaxies with  $C \gtrsim 0.5$  and their high stellarity indices indicate that they are predominately unresolved. All sources classified as stellar by Criteria 1 and 2 were visually inspected for confirmation. We found that  $\simeq 2.9\%$  of all reliable ( $3.6\mu\text{m}$  detected)  $24\mu\text{m}$  sources above  $450\mu\text{Jy}$  in each field were classified as stellar and discarded. These are indicated by a “+” in Figure 2. It is also interesting to note that the stellar fraction reported in other  $24\mu\text{m}$  *Spitzer* surveys at approximately the same galactic latitudes and depth is of order 4-8% (e.g., Marleau et al. 2004; Yan et al. 2004). These studies used a single stellar-flagging criterion based on discarding sources with R-band optical stellarity index  $> 0.8$ , and it’s possible that the stellar fraction was overestimated.

Figure 3 is an effective “color-color” plot using the addition of IRAC  $4.5\mu\text{m}$  band detections with flux densities  $\geq 10\mu\text{Jy}$  (minimum local SNR of  $\simeq 5\sigma$ ) in the EN1 field. Stellar candidates from criteria 1 and 2 are shown by grey squares. Overplotted are the tracks expected of a S0 and old elliptical galaxy (E) for redshifts  $z = 0\text{-}1$  from the SED template library of M. Polletta et al. (2005, in preparation). See also Lonsdale et al. (2004) for the tracks of a number of other galaxy templates. Even though the locus of E/S0-type galaxies overlap with the location of candidate stars, the stellar criteria are stringent enough to avoid extended sources (i.e., galaxies) from being mistakingly classified as stars. Even more, typical ellipticals (with  $3.6\mu\text{m}$  emission dominated by old stars) will drop out of a  $24\mu\text{m}$  flux limited ( $> 450\mu\text{Jy}$ ) sample at  $z \gtrsim 0.08$ . Therefore if seen, such galaxies are likely to be resolved and extended. As seen in Figures 2 and 3, there is indeed a population of sources with  $f_\nu(24\mu\text{m})/f_\nu(3.6\mu\text{m}) < 0.5$  which *do not* satisfy the stellar criteria. These comprise  $\simeq 7\%$  of all sources below this color cut (and incidentally have  $f_\nu(3.6\mu\text{m}) > 500\mu\text{Jy}$ ) which on visual examination at  $3.6$  and  $4.5\mu\text{m}$ , are resolved and extended. In conclusion, our stellar classification scheme is likely to be very reliable.

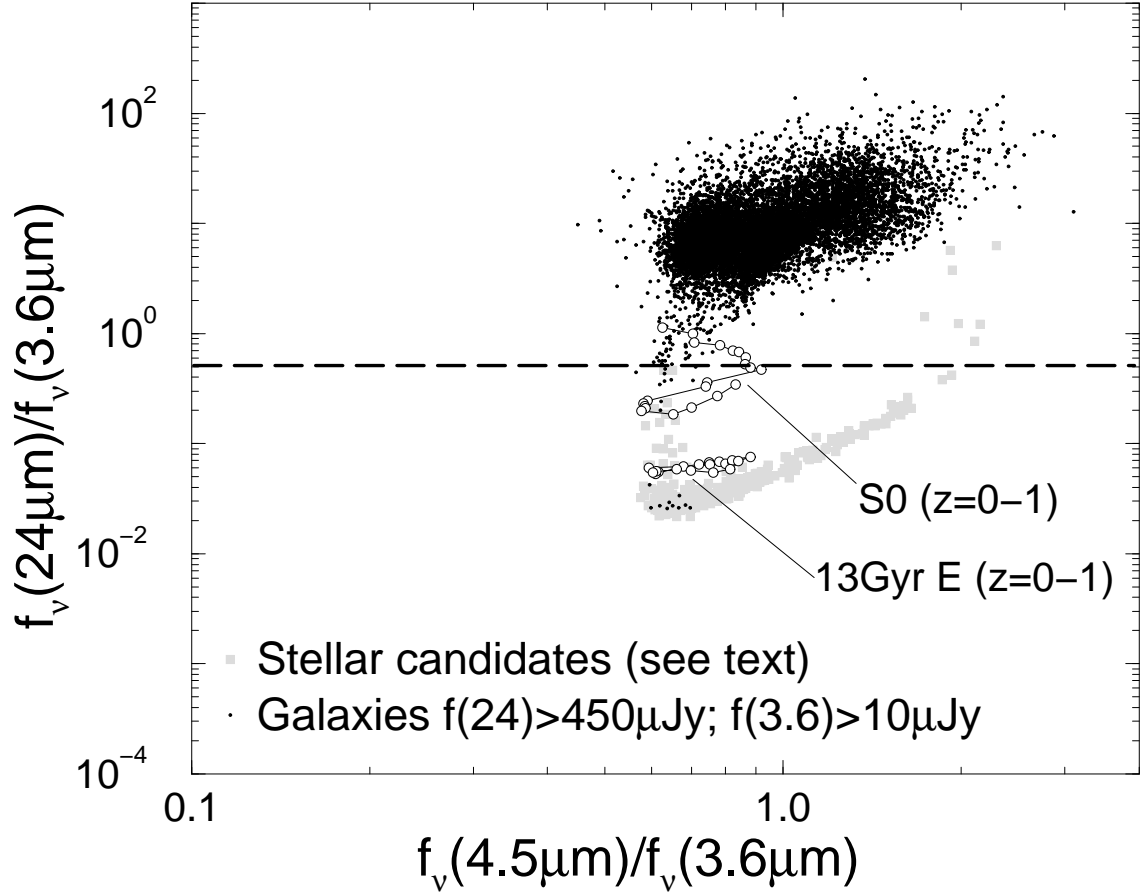


Fig. 3.— Effective “color-color” plot represented by flux density ratios  $f_{24}/f_{3.6}$  versus  $f_{4.5}/f_{3.6}$  for the EN1 field. Tracks of a typical S0 and 13 Gyr E-type galaxy SED within  $0 \leq z \leq 1$  in increments  $\Delta z = 0.05$  are labelled (from the SED template library of M. Polletta et al. 2005, in preparation). Grey boxes are sources classified as stellar. Most sources at  $f_{24}/f_{3.6} \leq 0.5$  which *do not* satisfy the stellar flagging criteria are resolved and bright at  $3.6\mu\text{m}$  with fluxes  $> 500\mu\text{Jy}$  (see bottom panel of Figure 2).

### 2.3. Sample Definitions

After discarding stellar candidates and all unreliable  $24\mu\text{m}$  detections (i.e., with no  $3.6\mu\text{m}$  association above  $10\sigma$ ), final statistics for all  $24\mu\text{m}$  field samples are summarized in Table 1. Note that a deeper version of the EN1 full-sample covering slightly larger area was used by Shupe et al. (2005) to study galaxy-counts. The samples used here have been optimized to measure galaxy clustering by using maximal contiguous areas of fixed (higher) minimum coverage, and using higher SNR cuts at 24 and  $3.6\mu\text{m}$  to ensure high and uniform completeness and reliability levels.

Since we will also explore clustering as a function of  $f_{24\mu\text{m}}/f_{3.6\mu\text{m}}$  flux ratio (effectively observed-frame near-to-mid-infrared color), we have subdivided each full sample into two broad subsamples defined by the flux ratio cuts:  $f_{24}/f_{3.6} \leq 5.5$  and  $f_{24}/f_{3.6} \geq 6.5$ . We refer to these as the *blue* and *red* subsamples respectively.

## 3. Counts-in-Cells Formalism

The galaxy count probability distribution function (CPDF or *counts-in-cells* distribution) gives the probability of finding  $N$  galaxies in a cell of a particular size and shape. Its moments have been used extensively to quantify the clustering pattern of galaxies (e.g., White 1979; Peebles 1980; Borgani 1996). In principle, the counts-in-cells distribution is straightforward to compute. One typically throws a number of cells of fixed volume at random within the survey boundaries, counts the number of galaxies in each cell and histograms the results. With no loss of generality (and as used in this study), the counts-in-cells can also be performed within projected cells subtending a solid angle  $\Omega$ . In this section, we outline the counts-in-cells approach, statistical measures and notation, and how the area-averaged  $n$ -point correlations are related to moments of the counts-in-cells distribution.

### 3.1. A Physically Motivated Galaxy CPDF Model

To interpret the statistics and shape of galaxy distribution functions in terms of physical clustering, we will compare our results to the discrete thermodynamic model of Saslaw & Hamilton (1984, hereafter SH84). See also Saslaw et al. (1990) and Saslaw & Fang (1996) for refinements thereof. This has attained widespread success in representing the observed CPDF in both 3-D and 2-D (projected) catalogs, such as the Zwicky catalog (Crane & Saslaw 1986), the CfA slice (Crane & Saslaw 1988), the UGC and ESO catalogs (Lahav & Saslaw 1992), the IRAS catalog (Sheth et al. 1994) and the Southern Sky Redshift Survey (SSRS,

Fang & Zou 1994). It has also been successfully applied to  $N$ -body simulations (e.g., Itoh et al. 1988), where it was shown that the model distribution function can describe both the 3-D spatial distribution and the projected distribution with the same value of the model parameter  $b$  (see below).

The theoretical CPDF,  $f(N)$ , of SH84 describes a statistically homogeneous system of point objects interacting under gravity in a quasi-equilibrium state:

$$f(N) = \frac{\bar{N}(1-b)}{N!} [\bar{N}(1-b) + Nb]^{N-1} e^{-[\bar{N}(1-b)+Nb]}, \quad (3)$$

where  $\bar{N}$  is the mean number of galaxies in a projected cell (e.g., see eq. [11]) and

$$b = -\frac{W}{2K} \quad (4)$$

is the ratio of gravitational potential energy (or “correlation energy” as quoted by SH84) to twice the kinetic energy of peculiar velocities  $v_i$ ,

$$K = \frac{1}{2} \sum_{i=1}^N m_i v_i^2, \quad (5)$$

where  $m_i$  is the mass of a galaxy member.

This model CPDF is therefore parameterized in terms of a single parameter  $b$ . For an uncorrelated (non-interacting) system of galaxies,  $b = 0$ , and equation (3) reduces to the well known Poisson formula:

$$f(N) = \frac{\bar{N}^N}{N!} e^{-\bar{N}}. \quad (6)$$

As the system relaxes and galaxies form into virialized clusters,  $b \rightarrow 1$ . For some  $N > 0$ , we see that  $f(N) \rightarrow 0$  as  $b \rightarrow 1$  unless we consider increasingly large volumes such that  $\bar{N} \rightarrow \infty$  and  $\bar{N}(1-b) \rightarrow \text{constant}$ . This is the virial limit and describes a hierarchy of clusters all in virial equilibrium. For virialized systems, the distribution represented by equation (3) therefore requires sampling over large volumes (or projected area) to ensure that  $\bar{N}(1-b)$  has converged to a constant value.

### 3.2. Angular Correlation Functions

Since we will be measuring *angular* (or projected) correlation functions, we briefly review these first. The two-point angular correlation function  $w_2(\theta)$  is defined from the joint

probability  $dP_2$  that two galaxies are centered in each of the elements of solid angle  $d\Omega_1$  and  $d\Omega_2$  at angular separation  $\theta = \theta_{12}$ :

$$dP_2 = \bar{n}^2 [1 + w_2(\theta)] d\Omega_1 d\Omega_2, \quad (7)$$

where  $\bar{n}$  is the mean surface density of galaxies.  $w_2(\theta)$  therefore measures the “excess” probability of finding two galaxies in  $d\Omega_1$  and  $d\Omega_2$  above that predicted by random (*Poisson*) sampling: ( $\simeq \bar{n}^2 d\Omega_1 d\Omega_2$ ). Following popular convention, we assume in this paper that  $w_2(\theta)$  can be parameterized as a power-law, with  $\theta$  measured in degrees:

$$w_2(\theta) = A\theta^{1-\gamma}, \quad (8)$$

where  $A$  is the correlation amplitude and  $\gamma$  the slope.

The three-point angular correlation function  $w_3(\theta_{123})$  is defined from the joint probability that three galaxies are found in the solid angle elements  $d\Omega_1$ ,  $d\Omega_2$  and  $d\Omega_3$ :

$$dP_3 = \bar{n}^3 [1 + w_2(\theta_{12}) + w_2(\theta_{13}) + w_2(\theta_{23}) + w_3(\theta_{123})] d\Omega_1 d\Omega_2 d\Omega_3. \quad (9)$$

The first term in equation (9) is the Poisson term, and accounts for uncorrelated triplets that may appear clustered just by chance or because of projection. The next three terms correspond to a combination of a correlated pair with an uncorrelated galaxy that forms a triplet also by chance or projections. The last term corresponds to true clustering, represented as an “excess” joint probability above all possible random associations. By studying  $w_3(\theta_{123})$ , we therefore avoid artificial clustering from projection effects.

### 3.3. Moments and Area-averaged Correlation Functions

The  $p^{\text{th}}$  moment about the mean of the galaxy counts-in-cells distribution, can be written

$$\mu_p = \langle (N - \bar{N})^p \rangle = \sum_{N=0}^{\infty} P_N(\Omega) (N - \bar{N})^p, \quad (10)$$

where  $\bar{N} = \bar{n}\Omega$  is the mean count in the solid angle  $\Omega$  for some mean density  $n$ :

$$\bar{N} = \sum_{N=0}^{\infty} N P_N(\Omega), \quad (11)$$

and  $P_N$  is the (discrete) normalized galaxy count probability distribution function (CPDF) of the underlying population, computed from randomly placed cells of size  $\Omega$ . In practice, one only has a *finite* sampling of the underlying population, so that the true  $P_N$  is not known

apriori, unless the survey region under consideration is infinitely sampled. In this case, it is more accurate to use *unbiased* estimators for the *population* moments. This arises from the fact that  $\bar{N}$  ( $\approx \bar{n}\Omega$ ) is computed empirically from the same sample from which the moments are estimated. The sample mean and *unbiased* estimators of the second and third moments are given by:

$$\begin{aligned}\bar{N} &= \frac{1}{N_T} \sum_{i=1}^{N_T} N_i, \\ \mu_2 &= \frac{1}{N_T - 1} \sum_{i=1}^{N_T} (N_i - \bar{N})^2, \\ \mu_3 &= \frac{N_T}{(N_T - 1)(N_T - 2)} \sum_{i=1}^{N_T} (N_i - \bar{N})^3,\end{aligned}\tag{12}$$

where  $N_T$  is the total number of randomly drawn cells which fall within the catalog boundaries (Kenney & Keeping 1962). The last two expressions in equation (12) are also known as the *population* variance and skewness respectively. These corrections for *finite* sample bias become important when the total number of cells thrown,  $N_T$ , is small. For our purposes, we typically have  $1000 < N_T < 2250$  for the range of cell sizes considered (see § 4), so that this estimation bias only accounts for at most 0.1%. Other biases due to finite sampling are discussed in § 4.1. The moments derived from equation (12) are valid only if  $\bar{N} \gg 1$  or as one approaches the continuum limit. Owing to discreteness however, the moments  $\mu_p$  must be corrected for (Poisson) shot-noise. In this limit, the first few moments,  $k_p$ , of discrete counts are related to  $\mu_p$  as follows (e.g., Gaztañaga 1994):

$$\begin{aligned}k_2 &= \mu_2 - \bar{N}, \\ k_3 &= \mu_3 - 3k_2 - \bar{N}, \\ k_4 &= \mu_4 - 7k_2 - 6k_3 - \bar{N}.\end{aligned}\tag{13}$$

The  $p$ -point *area-averaged* angular galaxy correlation function,  $\bar{w}_p(\Omega)$ , can be written in terms of a multi-dimensional integral of the  $p$ -point differential angular correlation  $w_p(\theta)$ , over the sampling area,  $\Omega$  (Peebles 1980):

$$\bar{w}_p(\Omega) = \frac{1}{\Omega^p} \int_{\Omega} d\Omega_1 \dots d\Omega_p w_p(\theta_1, \dots, \theta_p),\tag{14}$$

The  $\bar{w}_p$  are related to the corresponding discrete moments,  $k_p$ , of the CPDF through

$$k_p = \bar{N}^p \bar{w}_p(\Omega).\tag{15}$$

Using equations (13) and (15), the two and three-point *area-averaged* correlation functions for instance can be written:

$$\bar{w}_2(\Omega) = \frac{\mu_2}{N^2} - \frac{1}{N}. \quad (16)$$

$$\bar{w}_3(\Omega) = \frac{\mu_3}{N^3} - \frac{1}{N^2} - \frac{3\bar{w}_2(\Omega)}{N} \quad (17)$$

All quantities on the right of these equations are computable from the galaxy CPDF for a given cell size  $\Omega$ .

In general, clustering estimates from area-averaged angular correlations (eqs. [16] and [17]) lead to a considerable simplification in the data analysis, and give better signal-to-noise ratio properties. The statistics in equation (13) also represent respectively, the *variance*, *skewness* and *kurtosis* of the counts distribution, which are in turn are related to the two, three and four-point correlation functions. This paper only considers variance and skewness. We do not study kurtosis (four-point correlations) since as shown by previous studies (e.g., Kim & Strauss 1998), its estimated value is dominated by noise and good statistics are needed to measure it robustly.

We can evaluate the parameters  $A$  and  $\gamma$  in the traditional power-law parameterization for the differential two-point correlation function (eq. [8]) from the area-averaged function as follows. Inserting equation (8) into the definition for  $\bar{w}_{p=2}(\Omega)$  (eq. [14]), we have

$$\bar{w}_2(\Omega) = \frac{1}{\Omega^2} \int_{\Omega_1} \int_{\Omega_2} A \theta_{12}^{1-\gamma} d\Omega_1 d\Omega_2. \quad (18)$$

This integral is actually a two-dimensional integral over all possible pairs of elements  $d\Omega_1$  and  $d\Omega_2$  separated by  $\theta_{12}$  in the cell region bounded by  $\Omega$  (see Appendix A). Assuming *circular cells* of diameter  $\Theta_d$ , we find that this simplifies to

$$\bar{w}_2(\Theta_d) = \frac{16}{\pi^2} A C(\gamma) \Theta_d^{1-\gamma}, \quad (19)$$

where  $C(\gamma)$  is a coefficient depending on  $\gamma$  and is evaluated using numerical quadrature as outlined in Appendix A. From equations (16) and (19), we can therefore examine  $\bar{w}_2(\Theta_d)$  as a function of  $\Theta_d$  and fit for the parameters  $A$  and  $\gamma$  (see § 5.1).

We also compute the RMS fluctuation in galaxy counts relative to the mean count on angular scales represented by a specific cell diameter  $\Theta_d$ . This is related to the second moment of the CPDF and  $\bar{w}_2(\Theta_d)$  as follows:

$$\sigma_\Omega = \left\langle \left( \frac{\delta N}{N} \right)^2 \right\rangle^{1/2} = \sqrt{\frac{k_2}{N^2}} = \sqrt{\bar{w}_2(\Theta_d)}, \quad (20)$$

where  $k_2$  is the second moment corrected for shot-noise ( $\langle(N - \bar{N})^2\rangle - \bar{N}$ ; see eq. [13]), and the last step follows from equation (15). If shot-noise corrections to the second moment are ignored, then  $k_2$  is replaced by  $\mu_2$  ( $\equiv k_2 + \bar{N}$ ) in equation (20) and the RMS fluctuation becomes:

$$\sigma_\Omega = \sqrt{\frac{1}{\bar{N}} + \bar{w}_2(\Theta_d)}. \quad (21)$$

### 3.4. Error and Covariance Estimation

To estimate errors in statistics derived from *counts-in-cells*, we use the “bootstrap resampling method” (see e.g., Ling et al. 1986). This method is based on first generating  $N$  independent realizations (bootstrap samples) of random cell placements and measuring the desired statistic from each, e.g.,  $S_{i=1} \dots S_N$ , (which may be  $\bar{w}_2(\Theta_d)$  or skewness). An estimate for the statistic is then given by the average over all realizations:

$$\langle S \rangle = \frac{1}{N} \sum_{i=1}^N S_i, \quad (22)$$

and the uncertainty is computed from the variance of the realizations:

$$\sigma^2(S) = \frac{1}{N-1} \sum_{i=1}^N (S_i - \langle S \rangle)^2. \quad (23)$$

Previous studies (e.g., Hamilton 1993; Gaztañaga 1994; Magliocchetti et al. 1998) estimated the uncertainty by subdividing the survey region into different zones and computing the dispersion across all zones. Such methods however are conservative and errors are dominated by cosmic variance in the subregions. The above prescription provides an unbiased method of estimating sampling errors which are more representative for the whole survey field, rather than regions where cosmic variance (or real clustering) dominates. Errors estimated from the “bootstrap resampling method” also have good convergence properties, requiring at most 20 realizations of well sampled random cell placements.

The general error-covariance matrix describing correlations between (and variances within) measurements is computed from

$$\begin{aligned} \text{cov}(S_i, S_j) &= \langle (S_i - \langle S \rangle_i) (S_j - \langle S \rangle_j) \rangle_{realizations} \\ &\equiv \langle S_i S_j \rangle - \langle S \rangle_i \langle S \rangle_j, \end{aligned} \quad (24)$$

where  $S_i, S_j$  are two statistical quantities of interest which may be for example,  $\bar{w}_2(\Theta_i), \bar{w}_2(\Theta_j)$  estimated at two angular scales  $\Theta_i \neq \Theta_j$  and computed from single bootstrap realizations, and  $\langle S \rangle_i, \langle S \rangle_j$  are the respective ensemble averages of the quantities over their

bootstrapped realizations  $(i, j) = (1 \dots N, 1 \dots N)$  (as defined by eq. [22]). A final average ( $\langle \dots \rangle_{realizations}$ ) over all possible pairs of realizations  $(i, j)$  is then performed to compute  $\text{cov}(S_i, S_j)$ . Equation (24) reduces to the variance definition (eq. [23]) when  $i = j$  and  $\text{cov}(S_i, S_j)$  will refer to the diagonal elements of the covariance matrix. For  $i \neq j$  (non-diagonal elements), the  $\text{cov}(S_i, S_j)$  will refer to covariances between measurements, and these will be non-zero if they are not statistically independent. We will use this covariance matrix in § 5 when performing  $\chi^2$ -minimization fits to estimate the correlation function power-law parameters ( $A, \gamma$  in eq. [8]), since in general, the  $\bar{w}_2$  on different scales are *not* independent and the errors are correlated.

### 3.5. The Hierarchical Model and Scale Invariance

In the hierarchical model of galaxy clustering, all  $p$ -point volume or area-averaged correlation functions can be expressed in terms of the two-point function,  $\bar{\xi}_2(r)$  or  $\bar{w}_2(\Theta)$ , and dimensionless scaling coefficients  $S_p$ , e.g.,

$$\bar{w}_p(\Theta) = S_p \bar{w}_2^{p-1}(\Theta) \quad (25)$$

(Juszkiewicz et al. 1993; Bernardeau 1994; Fosalba & Gaztañaga 1998). This hierarchical scaling of the higher order moments is a signature of the evolution of an initially Gaussian distribution of density perturbations growing under gravity on linear to mildly non-linear scales. The coefficients  $S_p$  are the so-called *hierarchical amplitudes* and have the property of being scale invariant and insensitive to cosmic time and cosmology (Balian & Schaeffer 1989). Although initially derived and generalized for 3-D space, equation (25) also holds for a 2-D projected distribution.

In 3-D space, the amplitudes  $S_p$  can be computed using  $(p - 1)$ th order perturbation theory in the mildly non-linear regime (where  $\delta\rho/\rho$  or  $\bar{\xi}_2 \lesssim 1$ ). By applying second-order perturbation theory in a gravitational instability analysis, Bernardeau (1994) found that that  $S_3$  depends on the primordial power spectrum of fluctuations and, for a top-hat window, is given by

$$S_3 = \frac{34}{7} - (n + 3), \quad (26)$$

where  $n$  is the spectral index of the power spectrum,  $P(k) \propto k^n$ .  $S_3$  is also termed the “spatial skewness” and equation (26) and has been confirmed with  $N$ -body simulations (Lahav et al. 1993; Lucchin et al. 1994).

Evidence for the hierarchical model and scale invariance of  $S_3$  and  $S_4$  was first found in projected angular catalogues of optically selected galaxies (e.g., Groth & Peebles 1977;

Sharp et al. 1984). Since we derive clustering statistics from projected catalogs, our values for  $S_3$  cannot be directly compared to the spatial prediction in equation (26). Due to galaxy projections and mixing of scale lengths, it is a complicated procedure to derive the spatial skewness from projected statistics. Nonetheless, some authors have tried (e.g., Gaztañaga 1994; Magliocchetti et al. 1998), but results were extremely sensitive to the assumed redshift distribution. In light of the various (and complicated) estimation biases involved in computing  $\bar{w}_3$  and  $S_3$  (e.g., Hui & Gaztañaga 1999), we shall primarily concern ourselves on testing *qualitatively* the  $p = 3$  hierarchical model as described by equation (25).

We close this section by summarizing the main statistical measures derived from angular counts-in-cells that will be used in the analysis sections (§ 4 and 5) of this paper. First, we will compare observed CPDFs to the quasi-equilibrium gravitational clustering model of SH84 (eq. [3]) as a function of angular scale. Second, we will compute area-averaged two and three-point correlation functions from discrete moments of the CPDF (eqs. [16] and [17]). Third, the traditional power-law fit parameters  $A$  and  $\gamma$  in the parameterization for  $w_2(\theta)$  (eq. [8]) will be estimated from fits to the averaged correlations using equation (19). Finally, we will explore the hierarchical model (eq. [25]) and dependence of the  $S_3$  amplitude on angular scale.

#### 4. Counts-in-Cells Results

We computed 14 distributions of counts-in-cells using circular cells with angular diameters in the range  $\Theta_d = 0^\circ.05$  to  $0^\circ.7$  in intervals of  $0^\circ.05$ . From these, we measured the correlation statistics as a function of angular scale. This angular range corresponds to comoving scales of  $\simeq 1.8 - 26h^{-1}\text{Mpc}$  at the expected median redshift of  $\simeq 0.9$  for the full sample (from the model redshift distribution of Xu et al. 2003, in Figure 13). For each cell diameter, 5000 cells were initially thrown at random within a rectangular region encompassing each entire field (Figure 1). We then eliminated cells which fell outside or contained the boundaries of a field as defined by the high coverage regions (dashed boundaries in Figure 1). In the end, the number of independent cells which fell within each field region varied from  $\simeq 2250$  for  $\Theta_d = 0^\circ.05$  (smallest cell) to  $\simeq 1000$  for  $\Theta_d = 0^\circ.7$  (largest cell).

The smallest cell size with  $\Theta_d = 0^\circ.05$  was chosen to avoid severe shot-noise (Poisson) fluctuations, i.e., one with  $\bar{N} > 1$ . For this sized cell, we find  $\bar{N} \simeq 3.5$  which appears to be at the Poisson limit (still consistent with a Poisson distribution; e.g., see Figure 6), but starting to deviate from it. In figure 6 we also show a distribution for  $\Theta_d = 0^\circ.03$  to illustrate the Poisson behavior. The maximum cell diameter,  $\Theta_d = 0^\circ.7$  was chosen to avoid a systematic bias from the finite boundary of the catalog region. We refer to this as “finite-boundary

bias” and describe it in § 4.1.

Using the formalism of § 3 and our 14 angular counts-in-cells distributions, we computed mean counts, variances, skewnesses, medians, RMS fluctuations, relative biases, the “virialization” parameter  $b = -W/2K$ ,  $\bar{w}_2(\Theta_d)$  and  $\bar{w}_3(\Theta_d)$  as a function of angular scale. Some of these statistics are summarized for all samples in Table 1 for our maximum cell diameter of  $0^\circ.7$ . These statistics were estimated by ensemble averaging over 20 bootstrap realizations of  $N_T$  random cell placements within the boundaries of the catalog, where  $N_T$  depends on the cell diameter. Uncertainties in these quantities were computed from the standard deviation of realizations using the “bootstrap resampling method” as described in § 3.4. Although we assumed 20 realizations throughout, the computed averages and standard deviations were insensitive to the number of realizations used, and converged rapidly beyond 11 realizations. After a discussion of systematic biases, these quantities are further analyzed in § 4.2, § 5.2 and § 5.

Table 1. Sample summary and counts-in-cells statistics for  $\theta_{\text{diam}} = 0.7^\circ$ .

Subsample	$N_{\text{tot}}^{\text{a}}$	$\langle N \rangle^{\text{b}}$	$\langle \rho_N \rangle$	$\sigma_N$	skewness	median	$\delta N/N$	$b$
ELAIS-N1								
$f_{24} \geq 450 \mu\text{Jy}$ (full)	12040	596.07	1548.86	51.56	-0.171	599	0.085	0.54
$f_{24}/f_{3.6} \leq 5.5$ (blue)	2460	120.81	313.94	15.01	0.084	120	0.124	0.33
$f_{24}/f_{3.6} \geq 6.5$ (red)	8410	416.61	1082.53	39.74	-0.039	418	0.095	0.49
ELAIS-N2								
$f_{24} \geq 450 \mu\text{Jy}$ (full)	4979	514.89	1337.92	40.39	-0.947	522	0.078	0.42
$f_{24}/f_{3.6} \leq 5.5$ (blue)	1025	97.03	252.13	15.26	-0.185	99	0.157	0.32
$f_{24}/f_{3.6} \geq 6.5$ (red)	3470	370.40	962.47	33.45	-0.505	370	0.090	0.37
Lockman								
$f_{24} \geq 450 \mu\text{Jy}$ (full)	8633	552.03	1434.44	43.56	0.732	543	0.078	0.45
$f_{24}/f_{3.6} \leq 5.5$ (blue)	1780	106.68	277.20	18.98	0.423	103	0.161	0.41
$f_{24}/f_{3.6} \geq 6.5$ (red)	6009	390.55	1014.82	26.38	0.712	387	0.067	0.25

<sup>a</sup>Number of sources within contiguous areas of  $\simeq 8.62 \text{ deg}^2$  (ELAIS-N1),  $\simeq 3.98 \text{ deg}^2$  (ELAIS-N2) and  $\simeq 6.60 \text{ deg}^2$  (Lockman) for each respective subsample.

<sup>b</sup>The listed quantities  $\langle N \rangle$  (mean count),  $\langle \rho_N \rangle$  (mean surface density in  $\text{deg}^{-2}$ ),  $\sigma_N$  (standard deviation), skewness, median,  $\delta N/N$  (RMS fluctuation) and  $b$  ( $\equiv -W/2K$ ) correspond to a circular cell diameter of  $\theta = 0.7^\circ$ . These were estimated by averaging over 20 realizations of  $\simeq 1250$  random cell placements.

#### 4.1. Systematic Biases from Finite Sampling

Below we describe four biases that affect estimates of galaxy clustering from sampling a *finite*-sized survey region. These are often ignored when measuring clustering from counts-in-cells. The first is *finite-boundary bias* which limits the maximum usable cell size; the second is *cosmic variance* (or the “fair sample” approximation); the third is the *integral constraint bias* and the fourth, which affects mostly estimates of higher order moments, is *tail-sampling bias* from incomplete sampling of the high density tail of the CPDF in a finite survey area.

*Finite-boundary bias* arises from the fact that as one makes the cell size larger, there are fewer and fewer independently sampled regions which don’t overlap and fall within the survey area. The maximum cell size is that which fits within the entire region. However, its distribution is a delta function, peaking at the number of galaxies which fall within it. Therefore, as one makes the cell size larger, the mean and variance in galaxy counts from all cell placements approaches a constant and zero respectively. To explore this, we show in Figure 4 the variance,  $\sigma^2(N)$ , as a function of the mean number,  $\bar{N}$ , of galaxies computed from 5000 cell replacements for diameters  $\Theta_d = 0^\circ.03$  to  $2^\circ.50$  in the EN1 field. The solid diagonal line represents the Poisson prediction,  $\sigma^2(N) = \bar{N}$ , and the gradual positive excess in the measured variance above this line is due to real clustering. In other words, galaxy correlations modify the Poisson prediction to  $\sigma^2(N) = \bar{N} + \bar{N}^2 \bar{w}_2(\Theta_d)$  (c.f. eq. [16]), where  $\bar{w}_2(\Theta_d)$  is the area-averaged two-point correlation function. As the cell size increases beyond  $\Theta_d \simeq 1^\circ.2$ , the measured variance starts to turn over since the sampling is influenced by the finite survey boundary. Therefore, our maximum cell diameter of  $0^\circ.7$  (shown by the vertical dashed line), is well below scales on which systematic boundary effects start to dominate. Clustering estimates below this are expected to be unbiased.

*Cosmic variance* effects are most important for catalogs constructed from small fields where it is often assumed that the sample therein is “fair” in the sense that it represents an unbiased realization of a *homogeneous* part of the Universe. This however cannot be guaranteed since we know that galaxies are clustered on a wide range of scales. An example is the study by Coleman et al. (1988) who found that the run of spatial galaxy density as a function of cell size in the CfA catalog had still not reached homogeneity (constant density) on scales  $\simeq 20h^{-1}\text{Mpc}$ . If the mean galaxy number,  $\bar{N}$ , within a surveyed region is biased high or low, then this will bias correlation function estimates in the direction of either low or high respectively. This can be seen for example, from the functional dependence of  $\bar{w}_2(\Omega)$  on  $\bar{N}$  in equation 16.

Our samples, which cover contiguous areas of up to  $\simeq 8.5 \text{ deg}^2$  are expected to probe *comoving* scales of  $\simeq 112h^{-1}\text{Mpc}$  at the expected median redshift of 0.9 (Figure 13), or volumes of  $\simeq 2.5 \times 10^7 h^{-3}\text{Mpc}^3$  out to  $z \simeq 1.5$ . This range is expected to contain  $\gtrsim 90\%$

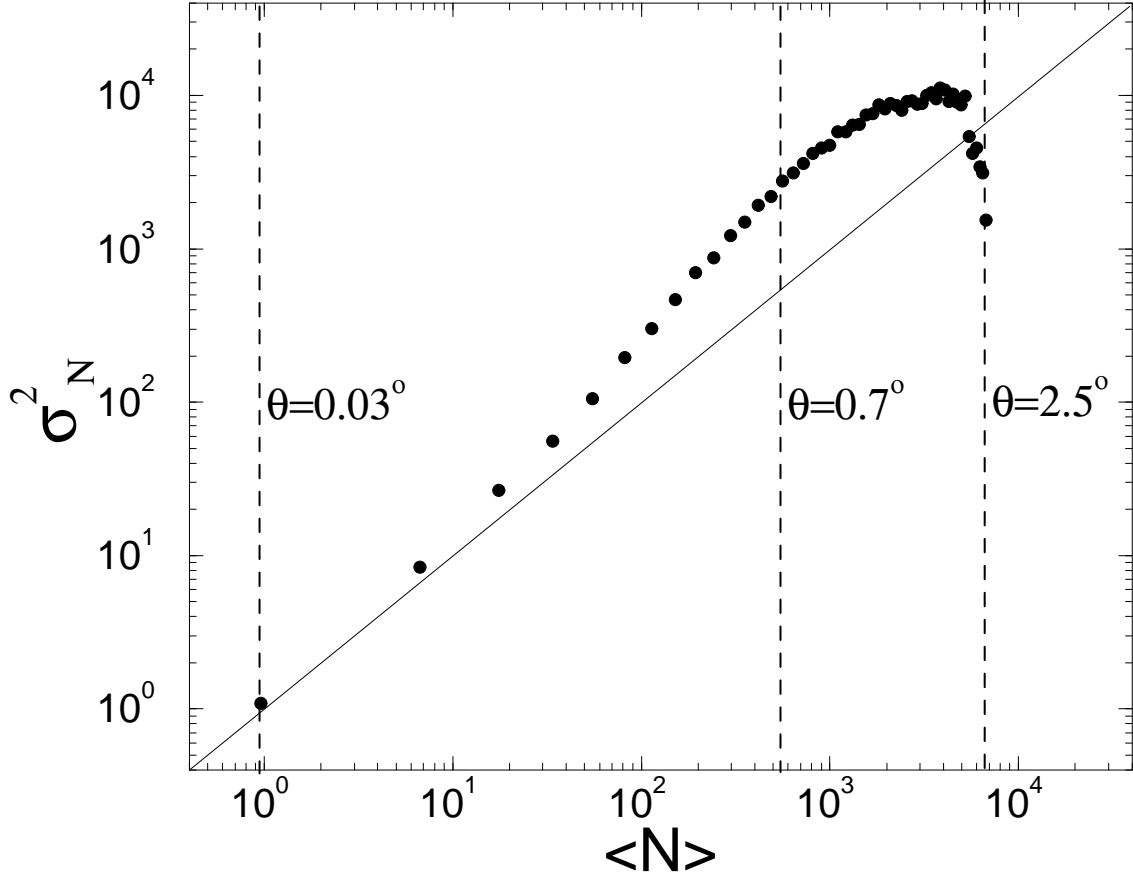


Fig. 4.— Variance ( $\sigma_N^2$ ) in number of sources as a function of the mean number,  $\langle N \rangle$ , within cells of angular diameter  $\theta = 0.03\text{--}2.5^\circ$  (filled circles) in the EN1 field. The solid diagonal line represents the Poisson prediction:  $\sigma_N^2 = \langle N \rangle$ . The gradual deviation from Poisson behavior with increasing  $\theta$  is due to correlations between sources. The maximum cell diameter used in this study,  $\theta = 0.7^\circ$  (shown), is well below scales ( $\gtrsim 1.2^\circ$  where  $\langle N \rangle \gtrsim 1900$ ) on which boundary effects become important.

of the population according to the Xu et al. (2003) model redshift distribution. Thus, the sample may be affected by superclustering. Spatial (3-D) homogeneity is difficult to ascertain from a projected sample due to mixing and randomization of projected scale lengths, which inevitably leads to an “artificial homogenization”. To get a handle on the *cosmic variance*, we compared statistics and angular correlations across all three SWIRE fields. We found that the mean galaxy count in  $0^\circ.7$  diameter cells randomly placed in each of the fields varied by  $\lesssim 15\%$ , the standard deviations by  $\lesssim 23\%$  (see values in Table 1), and the mean relative RMS deviation in  $\bar{w}_2(\theta)$  over all angular scales by  $\simeq 18\%$ . Figure 12 shows the relative RMS deviation in  $\bar{w}_2(\theta)$  as a function of angular scale. This measure is defined as

$$\left(\frac{\delta w_2}{w_2}\right)_\theta \equiv \frac{\sqrt{\langle(\bar{w}_2 - \langle\bar{w}_2\rangle)^2\rangle}}{\langle\bar{w}_2\rangle}, \quad (27)$$

where  $\langle\bar{w}_2\rangle$  is an average of  $\bar{w}_2(\theta)$  over all three fields. Our findings are consistent with the levels of cosmic variance found from number count studies to similar depths, showing that it cannot be neglected when deriving clustering from small area surveys (see Shupe et al. 2005, and references therein).

The *integral constraint bias* Infante (e.g., 1994) arises from the fact that methods used to estimate galaxy clustering (either from counts-in-cells or traditional binning techniques) involve counting the *excess* number of galaxies above a random realization of the same observed number within the survey region. This excess is expected to be biased “low” since the mean density,  $\langle n \rangle$ , itself is likely to be biased “high” from the presence of positive correlations between galaxies at small separations. In other words, the true mean density is unknown since the density is estimated from the same sample from which one measures clustering. If uncorrected, this bias causes all  $n$ -point correlation amplitudes to be underestimated (Hui & Gaztañaga 1999). A sample which satisfies the integral constraint implies that the integral of  $w_2(\theta)$  over the entire survey region vanishes. The integral constraint bias generally decreases in magnitude when the angular size of a survey increases significantly beyond the scale over which  $\bar{w}_2(\Theta)$  is measured, or over which it is relatively large. Since our maximum cell diameter of  $0^\circ.7$  is an appreciable fraction of the field sizes, this bias cannot be ignored.

Using the results from perturbation theory, Hui & Gaztañaga (1999) computed analytical expressions to correct for the integral constraint bias in 3-D clustering estimators. We instead start from the technique used by Infante (1994) who corrected for this bias in projected catalogs, and generalize it for the case of angular-averaged correlations,  $\bar{w}_2(\Theta)$ , computed from counts-in-cells. We first note that *on average*, the effect of  $\bar{w}_2(\Theta)$  is to increase the number of distinct galaxy pairs ( $N_{gg}$ ) found within a region of size  $\Theta$  by a factor of  $\simeq [1 + \bar{w}_2(\Theta)]$  over that expected for a random sample  $N_{rr}$ . In other words, the overdensity

in galaxy pairs with separations  $\theta_i \leq \Theta$  can be written:

$$\begin{aligned} \frac{N_{gg}(\leq \Theta)}{N_{rr}(\leq \Theta)} &= \frac{\int_0^\Theta [1 + w(\theta_i)] n(\theta_i) d\Omega_1 d\Omega_2}{\int_0^\Theta n(\theta_i) d\Omega_1 d\Omega_2} \\ &\simeq \frac{N_{rr}(\leq \Theta) + N_{rr}(\leq \Theta) \int_0^\Theta w(\theta_i) d\Omega_1 d\Omega_2}{N_{rr}(\leq \Theta)} \\ &= 1 + \bar{w}_2(\Theta) \end{aligned} \tag{28}$$

where  $n(\theta_i)$  is the underlying random galaxy pair density, and assumed more-or-less constant on scales above which shot noise fluctuations dominate, i.e., at  $\theta_i \gtrsim 50''$  where  $\bar{N}_{rr} \approx 1$ . Without loss in generality, we can define a bias factor  $\beta$  for a survey with angular extent  $\Theta_s$ , above which the mean pair density is over-estimated:

$$\begin{aligned} \beta &= 1 + \bar{w}_2(\Theta_s), \\ &\simeq 1 + \bar{w}_2(\Theta_{max}) \left( \frac{\Theta_s}{\Theta_{max}} \right)^{1-\gamma}, \end{aligned} \tag{29}$$

where  $\bar{w}_2(\Theta_s)$  applies to the whole survey region. The second line in equation (29) results from the fact that  $\bar{w}_2(\Theta_s)$  cannot be directly measured from the sample due to the *finite boundary* bias. It therefore must be extrapolated from an unbiased measurement on smaller scales, i.e., at  $\Theta_{max} = 0^\circ.7$ . The underlying assumption here is that a power-law, as parameterized by equation (19) applies across a full survey field. For the EN1, EN2 and LH fields,  $\Theta_s \simeq 2^\circ.93$ ,  $2^\circ.00$ , and  $2^\circ.60$  respectively.

All *observed* measurements of  $\bar{w}_2(\Theta)$  for  $\Theta \leq \Theta_s$  can therefore be corrected (upward) for the integral constraint bias by first noting that  $[1 + \bar{w}_2(true)] = \beta [1 + \bar{w}_2(obs)]$ . Hence, the true (corrected)  $\bar{w}_2(\Theta)$  is given by:

$$\bar{w}_2(\Theta) = \beta \bar{w}_2(\Theta)_{obs} + \beta - 1, \tag{30}$$

where  $\beta \bar{w}_2(\Theta)_{obs}$  is computed using the moments methods outlined in § 3.3. Since  $\beta$  (eq. [29]) depends on  $\bar{w}_2(\Theta_s)$  which itself needs to be *corrected* for bias according to equation (30), we compute  $\beta$  iteratively. In the first pass,  $\beta$  is set to unity;  $\bar{w}_2(\Theta_s)$  (or more specifically  $\bar{w}_2(\Theta_{max})$ , see eq. [29]) is then computed from equation (30), and the procedure is repeated until  $|\delta\beta/\beta| \lesssim 10^{-4}$ . We found that this criterion was usually satisfied after the second iteration. The values of  $\beta$  for all our samples are reported in Table 2.

We make no attempt to correct for the integral constraint bias that may affect estimates of  $\bar{w}_3(\Theta)$ . A  $p^{\text{th}}$  higher order moment depends on all lower  $< p$  order moments (see § 3.3) and terms involving  $1/\bar{N}^p$ . Thus, they are subject to more complex (higher order) manifestations of the integral constraint bias. As described by Hui & Gaztañaga (1999), such biases are

difficult to estimate and one usually has to resort to simulations. The associated higher order corrections to  $\bar{w}_{p>2}(\Theta)$  decrease more rapidly with increasing survey area, although they are not necessarily smaller than that for  $\bar{w}_2(\Theta)$ . In view of this, computations involving  $\bar{w}_3(\Theta)$  in this paper, e.g., in testing the hierarchical model and its overall scale invariance (§ 5.3), will be purely qualitative.

The final finite-area sampling bias is that from incomplete sampling of the high density tail of the CPDF, or, *tail-sampling bias*. This was first discussed by Colombi et al. (1994) and can be attributed to the abrupt cutoff in the cell counts distribution at some finite number of galaxies due to the finite area of survey. In other words, there is always a densest region in the finite area of a survey above which the sampled CPDF goes to zero for higher density. High density fluctuations are rare and one generally needs a larger survey to reduce the bias. For a given survey area, this bias can be minimized by ensuring that the survey is densely sampled with a large number of cells (Szapudi & Colombi 1996). The bias mostly affects the high-order moments of the CPDF (e.g., skewness, kurtosis, etc.) since they are heavily weighted by its high density tail. Simulations and modelling have shown that the galaxy CPDF asymptotically approaches an exponential at high densities, and various authors have corrected for this bias by extending the tail CPDF using functional forms calibrated from simulations (e.g., Colombi et al. 1994; Fry & Gaztañaga 1994; Kim & Strauss 1998). Unless the survey area (or volume) is very small, or insufficient sampling used, these studies have shown that the variance of the CPDF, and hence the two-point correlation amplitude derived therefrom is relatively insensitive to the tail of CPDF. From the relatively large sizes of our fields, the dense sampling used, and excellent agreement of the data with high density-tail predictions from model fits (see § 4.2), we make no explicit corrections for this bias.

## 4.2. Distribution Functions and Fits

Galaxy counts-in-cells distributions for the *full* EN1 sample, for nine different cell sizes are shown in Figure 6. The histograms are compared with the predictions of a Poisson distribution (*dashed* curves) given the observed mean count  $\bar{N}$  within each cell (eq. [6]). The Poisson prediction is seen to provide good fits to histograms of cell counts for cell sizes  $\theta \leq 0^\circ.05$ . On these scales, shot noise fluctuations are seen to dominate, since one has a finite probability of finding an empty cell. For  $\bar{N} \gtrsim 10$ , or cell diameters  $\theta \geq 0^\circ.1$ , the Poisson prediction is expected to approach a Gaussian with  $\sigma_N^2 \approx \bar{N}$ . The histograms however start to deviate dramatically from these predictions. For  $\theta \geq 0^\circ.1$ , the results of Kolmogorov-Smirnov tests show that the probabilities that the histograms are consistent with a Poisson distribution are at the  $< 0.02$  per-cent level.

Some statistical quantities of interest as a function of angular scale for the *full* EN1 sample are shown in Figure 5. RMS fluctuations in the counts relative to the mean in each cell are shown in the top panel. These estimates were *not corrected* for shot-noise (Poisson) fluctuations as represented by equation (21). Pure Poisson RMS fluctuations are given by  $\langle(\delta N/N)^2\rangle^{1/2} = \sqrt{\sigma_N^2/\bar{N}^2} \equiv 1/\sqrt{\bar{N}}$ , where  $\sigma_N^2 \equiv \bar{N}$ . This prediction is shown by the solid curve in this plot and represents the fluctuations one would obtain if the galaxy distribution were assumed to be purely random (where by definition  $\bar{w}_2(\theta) = 0$ ). The middle panel in Figure 5 shows *skewness* as a function of angular scale. Its definition and implications are discussed below. The bottom panel shows the mean galaxy surface density,  $\bar{n}_g = \bar{N}/A_c$ , where  $A_c$  is the cell area. The density for a random (Poisson) distribution (not shown) is expected to be more or less uniform and independent of scale, or within shot-noise fluctuations on the smallest scales.

There is significant non-Gaussian behavior when the statistics in Figure 5 or Table 1 are examined. This may not be immediately obvious from the counts-in-cells distributions of Figures 6 and 7. For Gaussian statistics, the (third moment) skewness (and all higher-order odd numbered moments) are exactly zero. Skewness causes the mode and median of the distribution to shift from the mean. A positive skewness implies that the galaxy distribution functions are skewed towards larger source numbers, or, that typically the *median*  $\lesssim \bar{N}$  (as seen in Table 1). The opposite holds for negative values of skewness. Detection of non-zero skewness is of fundamental importance, since assuming evolution of clustering from Gaussian primordial perturbations and linear theory implies that the skewness and all higher order moments should remain zero (see Peebles 1980, and § 1). Non-zero detections may then be a signature of non-linear gravitational clustering and are expected in the framework of “biased” models of galaxy formation (Kaiser 1984; Bardeen et al. 1986).

We have computed the skewness using the conventional (nondimensional) definition:  $\text{skew}(N) = \mu_3/\mu_2^{1.5}$ , where the moments  $\mu_3$  and  $\mu_2$  are computed using the *unbiased* population estimators in equation (12). This skewness is shown as a function of angular scale for the full sample in the *middle panel* of Figure 5, where we also show the Poisson prediction:  $\text{skew}(N)_{Pois} = 1/\sqrt{\bar{N}}$ . We have estimated the standard deviation in the skewness,  $\sigma(\text{skew})$ , using the bootstrap resampling method (eq. [22]) with 20 realizations. Examining the skewness values in Table 1, we find significant non-zero skewnesses at the  $> 5\sigma$  level according to bootstrapped uncertainties in all, but the blue and red subsamples of EN1. Setting aside bootstrapped uncertainties, there is common belief in the statistics literature that a non-zero skewness is statistically significant if its magnitude is larger than  $\sqrt{6/\bar{N}}$  (e.g., Press et al. 1999, p. 612), where  $N$  is the number of samples (i.e., the number of randomly thrown cells). With at least  $N \simeq 1000$  cells falling within each field for  $\theta = 0^\circ.7$ , we have  $\sqrt{6/1000} \simeq 0.077$ , consistent with the skewnesses being significant.

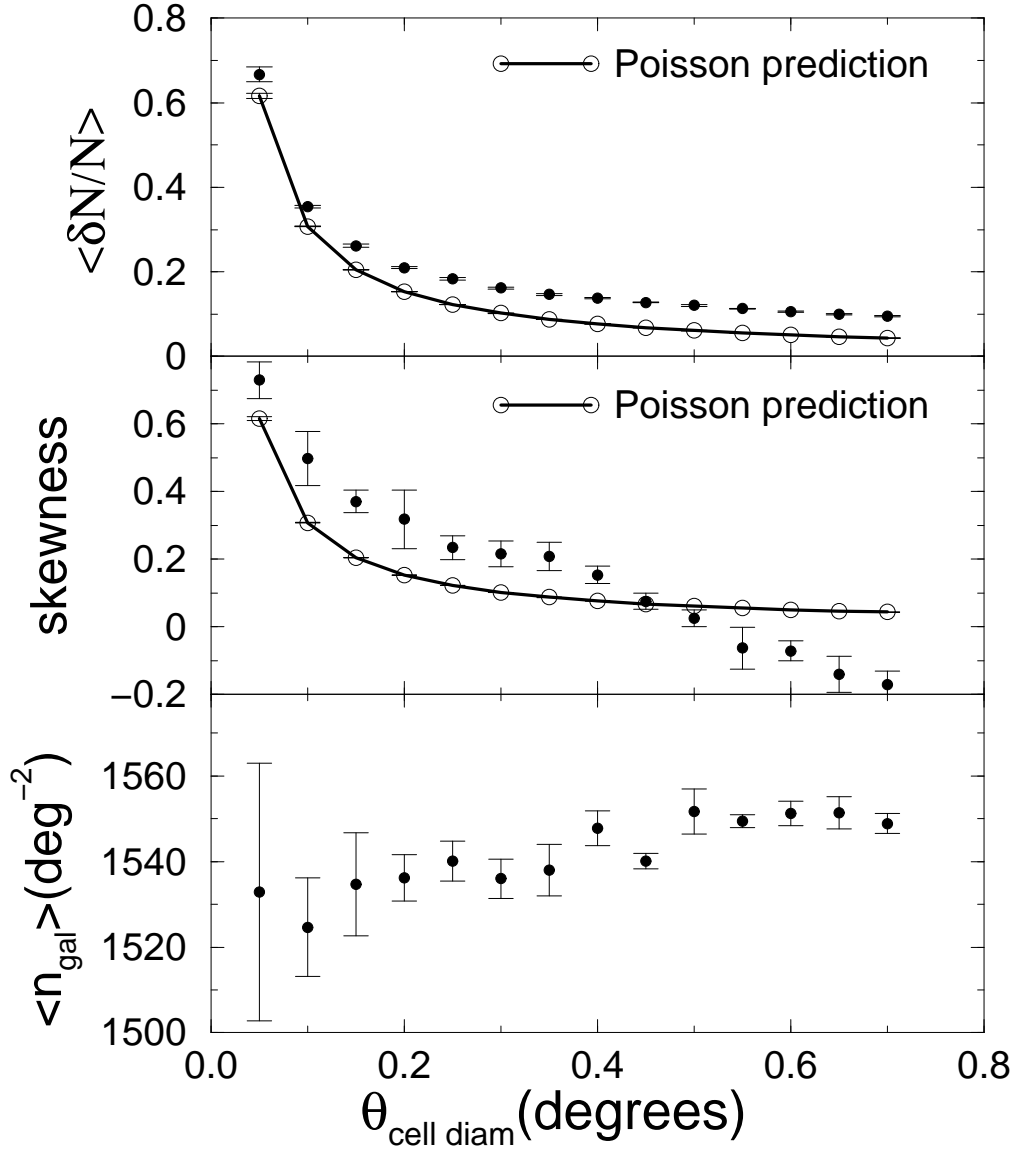


Fig. 5.— Counts-in-cells statistics for the EN1 *full sample* as a function of cell diameter (filled circles): RMS fluctuations (*top*), skewness (*middle*) and surface density (*bottom*). Poisson predictions are shown by open circles connected by solid lines. To facilitate a comparison with Poisson predictions, all measurements (filled circles) are as observed, and have not been corrected for shot-noise (Poisson) fluctuations.

To compare our skewness measurements with other studies, Plionis & Basilakos (2001) found skewness levels of  $\simeq 0.69$  and  $\simeq 0.28$  on scales of 10 and 15 Mpc respectively in the IRAS PSCz catalog. Despite probing similar length scales (albeit in projection), the reduced skewnesses in our study are most likely due to the samples probing a larger redshift range (e.g., Figure 13), where projection effects and mixing of galaxy-galaxy separations significantly reduces the angular clustering at all orders. Nonetheless, the observed skewnesses are likely to be real, and are consistent with models of non-linear gravitational clustering evolved from Gaussian primordial fluctuations. The existence of both *positive* and *negative* skewnesses amongst our samples is also consistent with numerical simulations (Moscardini et al. 1991; Coles et al. 1993), where a negative skewness can be interpreted as an overdensity of voids in the distribution.

The histograms of the cell counts were fitted to the gravitational clustering model of SH84 (eq. [3]) for the observed value of  $\bar{N}$  to determine the dimensionless parameter  $b = -W/2K$  as a free parameter (see § 3.1). These fits are shown as *solid* curves in Figure 6 for the full EN1 sample and the full angular range, and Figure 7 for other samples and a fixed cell diameter of  $0^\circ.4$ . The counts-in-cells on scales of  $0^\circ.05$  to  $0^\circ.7$  are seen to agree very well with the theoretical CPDF of SH84. In previous studies, the model was also seen to provide good fits to counts on larger scales, e.g., from the Zwicky catalog up to  $\theta \simeq 5^\circ$  (Saslaw & Crane 1991), indicating an overall statistical homogeneity in the galaxy distribution from small to large scales. Our results also suggest that  $24\mu\text{m}$  samples probe scales where clustering can still be described as a quasi-equilibrium thermodynamic process, the underlying assumption of the SH84 model. Even though the angular scales in our analysis are relatively small (as limited by the *finite-boundary bias*; see § 4.1), the mean number of galaxies within  $\theta = 0^\circ.1$ ,  $\bar{N} \simeq 10$  is comparable to that seen in the Zwicky catalog on  $3^\circ$  scales to an optical magnitude limit of  $\approx 15$ . If there were any pronounced structures on any particular scale within  $0^\circ.1 \lesssim \theta \lesssim 0^\circ.7$  (where eq. [3] with  $b > 0$  provides a better fit than the Poisson prediction), then they would have led to departures from the CPDF model of SH84.

Figure 7 compares observed distributions between the *blue* and *red* subsamples in EN1 (panels *b* and *d* respectively) for a fixed cell diameter of  $0^\circ.4$ , i.e., a cell size which straddles the full range considered in Figure 6. Two distinguishing features between these histograms are the variance and mean galaxy count. The *red* subsample has  $\approx 3.4\times$  more galaxies and a variance  $\approx 6.7\times$  greater than the *blue* subsample. This may lead one to believe that since the *red* subsample has a larger variance, it has stronger clustering. In general however, clustering is defined as the “excess fraction” above Poisson, and in our case, is effectively measured by the ratio  $\sigma_N^2/\bar{N}^2$  (cf. eq. [16]). This then implies that clustering is actually  $\approx 1.7\times$  stronger in the *blue* subsample on  $0^\circ.4$  scales. In fact, this difference in angular clustering

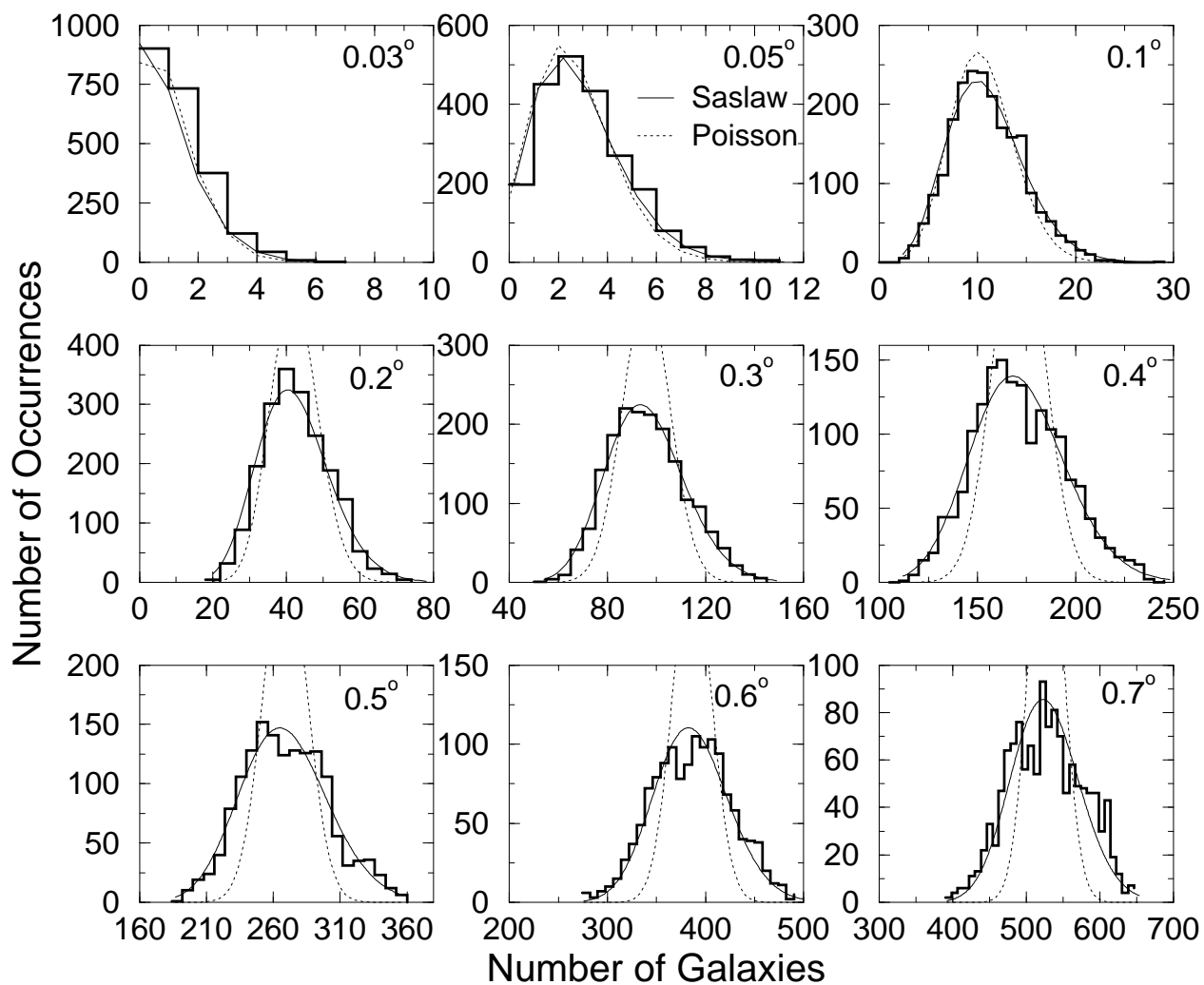


Fig. 6.— Distributions of projected counts-in-cells for the full EN1 sample for nine cell diameters  $0.^{\circ}03$  to  $0.^{\circ}7$ . Poisson predictions are shown by *dashed* curves and fits of the quasi-equilibrium gravitational clustering model of Saslaw & Hamilton (1984) by *solid* curves.

strength between the color subsamples (from each field) is entirely consistent with them probing different redshift ranges. The *blue* subsample members are predominately located at low redshift (see Figure 13) where their intrinsic clustering is less affected by dilution from projected random galaxy-pairs.

In addition to the CPDF model fits of SH84, we also found very good fits of a lognormal distribution to cell counts on all scales, with the quality of fits between these two model CPDFs being largely indistinguishable. The lognormal CPDF is defined by

$$f(N) = \frac{1}{N\sqrt{2\pi\sigma_g^2}} \exp\left[-\frac{(\log N - \mu_g)^2}{2\sigma_g^2}\right], \quad (31)$$

where  $\mu_g$  and  $\sigma_g^2$  are the mean and variance of the underlying *Gaussian* field, not that of the observed distribution. They are related to actual observables  $\bar{N}$  and  $\sigma_N^2$  by  $\mu_g = \log(\bar{N}) - (\sigma_g^2/2)$  and  $\sigma_g^2 = \log[1 + (\sigma_N^2/\bar{N}^2)]$ . The physical motivation for this CPDF was outlined by Coles & Jones (1991). In general, these authors argued that it provides a natural description for density perturbations resulting from Gaussian initial conditions in the weakly non-linear regime ( $\bar{\xi}_2 \gtrsim 1$ ). Kofman et al. (1994) showed that the CDPF of IRAS galaxies is well modelled by a lognormal distribution. Equation (31) however is strictly a *continuous* distribution where it makes better sense to replace  $N$  by the underlying smoothed galaxy mass density  $\rho$ , with  $\rho > 0$  on all scales. In fact, it was shown by Zinnecker (1984) to provide a good description of the mass function resulting from hierarchical fragmentation and merging. Galaxy counts, on the other hand, are expected to be a biased tracer of this underlying matter field, and it is not clear how the two are related on all scales. The SH84 model describes a discrete distribution derived from the thermodynamics of interacting particles, and thus facilitates a more direct comparison with galaxy counts. Furthermore, using CDM N-body simulations, Bernardeau & Kofman (1995) have shown that the lognormal distribution does not naturally arise from mildly non-linear gravitational growth. It only provides a convenient fit in a certain region of parameter space in the linear regime ( $\bar{\xi}_2 \ll 1$ ). Thus, even though equation (31) may provide a better fit than a Gaussian to counts (or mass densities modulo some bias factor) on all scales, its physical interpretation and evidence are still circumstantial.

In Figure 8 we plot the virialization parameter  $b$  as a function of angular scale for all subsamples, derived from fits of equation (3) to the observed distributions. The second and third moments about the mean for this model distribution ( $\langle(N - \bar{N})^2\rangle$  and  $\langle(N - \bar{N})^3\rangle$ ) can be written in terms of  $b$  as follows (Saslaw 1989):

$$\mu_2 = \frac{\bar{N}}{(1-b)^2}; \quad \mu_3 = \frac{\bar{N}(1+2b)}{(1-b)^4}. \quad (32)$$

With a little algebra, we use equations (16) and (17) together with (32) to derive expressions

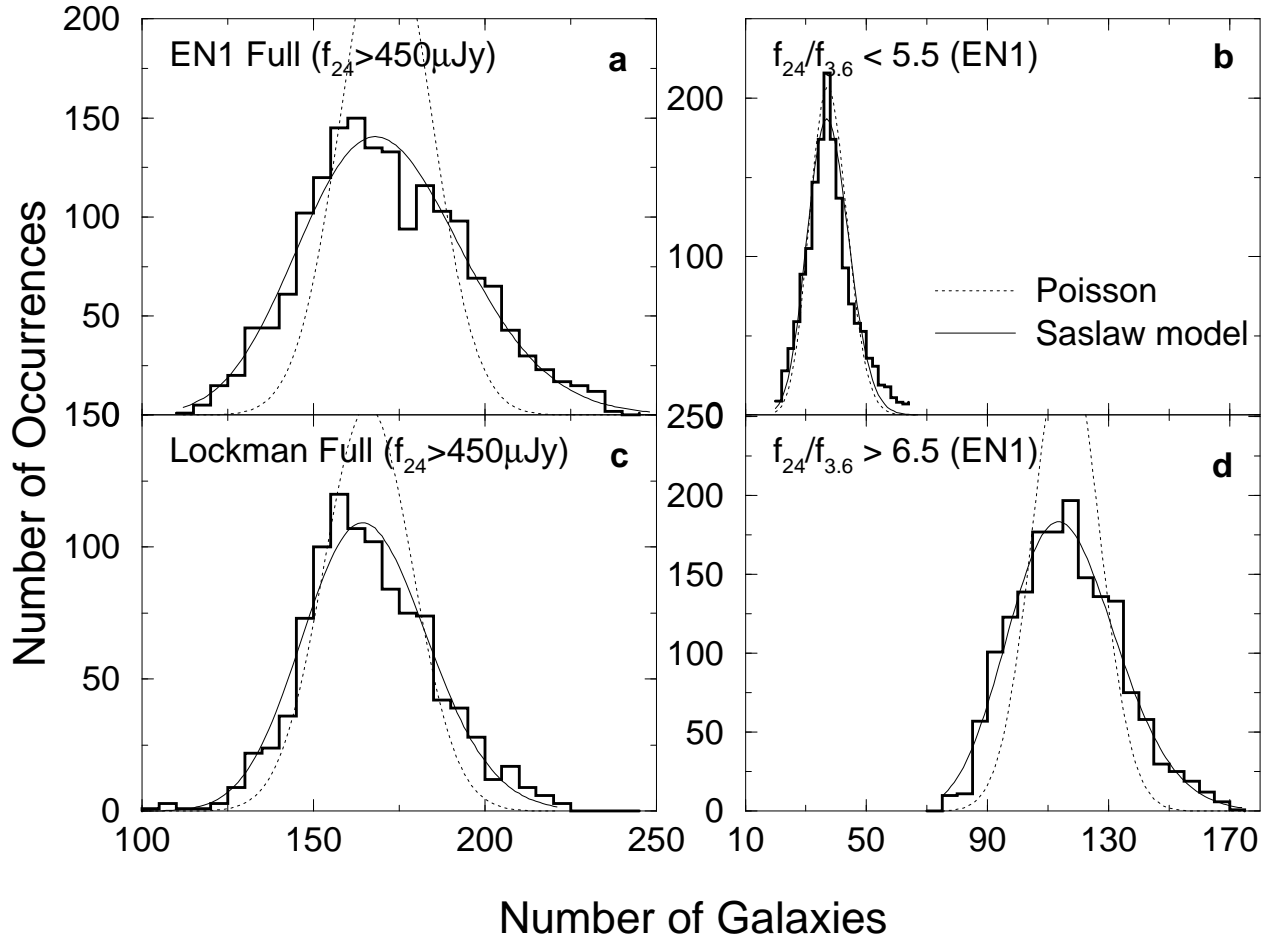


Fig. 7.— Distributions of counts-in-cells for a fixed cell diameter of  $0.4^\circ$  ( $24'$ ) for (a) full EN1 sample, (b) blue EN1 subsample, (c) full Lockman sample and (d) red EN1 subsample. Poisson predictions are shown by *dashed* curves and fits of the quasi-equilibrium gravitational clustering model of Saslaw & Hamilton (1984) by *solid* curves. Pairs of panels (a, c) and (b, d) are plotted with the same abscissae to facilitate comparison.

for the angular averaged two and three point correlation functions in terms of  $b$ ,

$$\bar{w}_2(\theta) = \frac{1}{\bar{N}} \left[ \frac{1}{(1-b)^2} - 1 \right], \quad (33)$$

$$\bar{w}_3(\theta) = \frac{1}{\bar{N}^2} \left[ \frac{(1+2b)}{(1-b)^4} - \frac{3}{(1-b)^2} + 2 \right]. \quad (34)$$

Motivated by the observed power-law dependence for  $\bar{w}_2(\theta)$  (eq. [19]), we write  $\bar{w}_2(\theta) = \alpha\theta^s$  where  $s = 1 - \gamma$ . Using this parameterization, equation (33) can be inverted to write  $b$  as a function of angular scale:

$$b = 1 - [1 + \bar{N}\bar{w}_2(\theta)]^{-1/2} = 1 - (1 + \bar{N}\alpha\theta^s)^{-1/2}. \quad (35)$$

Equation (35) can be linearized in the form  $Y = C + sX$ , where  $Y = \log [(1-b)^{-2} - 1]$ ,  $C = \log(\bar{N}\alpha)$  and  $X = \log \theta$  so that we can fit the  $b$  versus  $\theta$  measurements using linear regression. Here, we are primarily interested in the qualitative functional dependence of  $b(\theta)$  and not the values of the fitted power-law parameters (see § 5 for these). Fits of equation (35) are shown by the solid lines in Figure 8. The uncertainty in  $b$  was estimated indirectly from uncertainties in  $\bar{w}_2(\theta)$ . Propagating errors in the first relation of equation (35), we find

$$\sigma_b = \frac{\bar{N}}{2}(1-b)^3\sigma_{\bar{w}_2}, \quad (36)$$

at each angular scale with measured values of  $b$  and  $\bar{w}_2$ . The  $\sigma_{\bar{w}_2}$  were computed using a “bootstrap resampling” with 20 realizations (see § 3.4). Across all samples, we find  $0.01 \lesssim \sigma_b \lesssim 0.03$  where the lowest and highest values correspond to the smallest and biggest angular scales respectively.

Overall, the dependence of  $b$  on angular scale over  $0.^{\circ}05 \leq \theta \leq 0.^{\circ}7$  agrees rather well with the functional form of equation (35). This is an indication that the assumption of a power-law dependence for  $\bar{w}_2(\theta)$  is a good one. This will be verified using a more direct fitting approach of equation (19) to the data in § 5.1. Figure 8 has two noteworthy features. First, there appear to be regimes for each subsample where  $b$  levels off and approaches a constant on large scales. This is required by the assumptions leading to the derivation of the SH84 distribution function (eq. [3]), where statistical homogeneity in the galaxy distribution has been attained. This was verified in N-body simulations by ?. Put another way, if we assume  $\bar{N} \simeq \bar{n}_g\theta^2$  for an approximately constant mean surface density  $n_g$ , and if  $\bar{w}_2 \simeq \alpha\theta^{1-\gamma}$ , then the product  $\bar{N}\bar{w}_2 \simeq \bar{n}_g\alpha\theta^{3-\gamma}$  in equation (35) must approach a constant on large scales. This implies that on large scales,  $b \sim 1 - (\bar{N}\bar{w}_2)^{-1/2}$  if  $\gamma < 3$ . This constraint on  $\gamma$  is indeed consistent with observations. The second feature in Figure 8 is that the  $b$  values decrease towards the Poisson limit with decreasing  $\theta$  as expected, i.e., as  $\theta \rightarrow 0$ ,  $\bar{N}\bar{w}_2 \rightarrow 0$  and  $b \rightarrow 0$  if  $\gamma < 3$ .

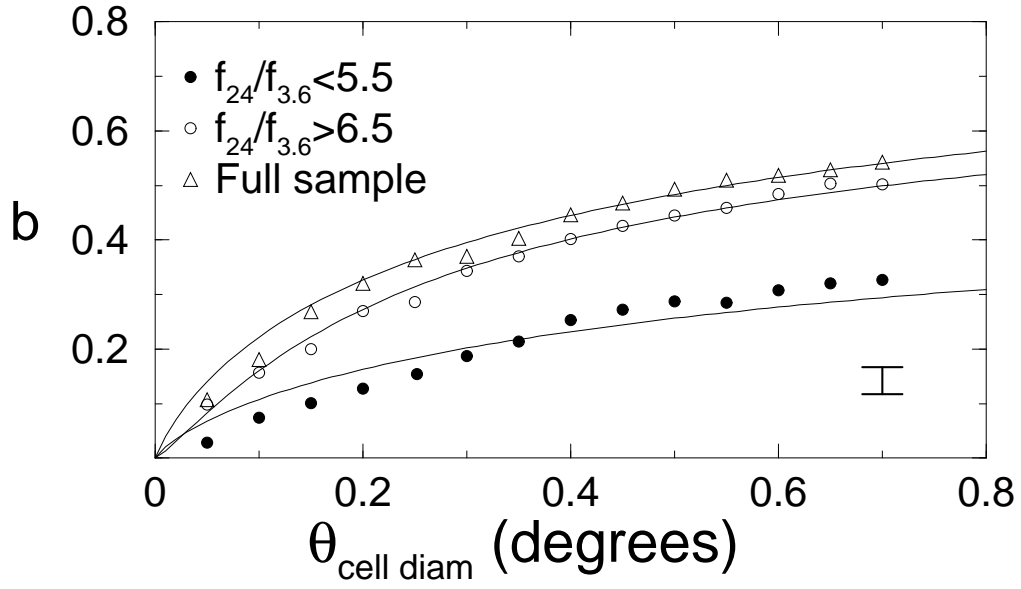


Fig. 8.— Ratio of gravitational correlation energy to twice kinetic energy ( $b = -W/2K$ ) from distribution model fits as a function of cell diameter for all subsamples in the EN1 field. The maximum uncertainty in  $b$  is typically  $\sigma_b \simeq 0.03$  and occurs on the largest sampled scale ( $\theta = 0.7^\circ$ ). This is depicted by the error bar at bottom right in each panel. Solid curves are fits of the form given by equation 35 (see § 4.2). Values of  $b$  on the largest scales for all samples are summarized in Table 1.

Another feature to note is the different asymptotic values of  $b$  for the *blue* and *red* subsamples in each field as shown in Table 1. From equation (35), this is just an interplay between the various values of  $\bar{N}$  and  $\bar{w}_2$  for each subsample so that effectively, the product  $\bar{N}\bar{w}_2$  is different for each. Aside from these intrinsic differences, we can test the hypothesis that each color subsample was selected at random from its full sample, independent of galaxy *neighbor* density (hence clustering strength). We test this using a result from Saslaw (1989), who showed that if the sampling is random, then the value  $b_s$  for a subsample is related to the value  $b$  for the *full* sample by

$$(1 - b_s)^2 = \frac{(1 - b)^2}{1 - (1 - p)(2 - b)b}, \quad (37)$$

where  $p$  is the probability of selecting a subsample member from the full sample (i.e., the ratio of the number of galaxies in the subsample to that in the full sample).

Given the  $p$  and *full-sample*  $b$  values, we can use the random sampling hypothesis (eq. [37]) to predict the values of  $b_s$  for each color subsample in each field. For the EN1, EN2 and LH fields, we find  $b_s(\text{blue/red}) = (0.24/0.47)$ ;  $(0.15/0.35)$ ; and  $(0.17/0.38)$  respectively. We see that the  $b$  values for the blue subsamples estimated from distribution function fits (Table 1) are all significantly larger (at  $> 3\sigma$ ) than the values  $b_s$ , predicted from random sampling. This suggests the blue subsamples, taken separately, exhibit different angular clustering properties than the red subsamples. In other words, the 3.6-24 $\mu\text{m}$  color of a galaxy appears to depend on the number of galaxies in its environment when *seen in projection*. This observation is none other than the redshift-range dependent projection effect discussed above. The lower redshifts for blue galaxies in general (Figure 13) makes their angular clustering less prone to dilutions from random projections relative to red subsamples.

As described by SH84 (and later elucidated by Fry 1985),  $b$  has both a physical and statistical interpretation. These authors suggest that  $b$  measures the “degree of virialization”,  $-W/2K$ , for a gravitating system of point particles in quasi-equilibrium. For a perfect gas  $b = 0$ , while for relaxed clustering,  $b = 1$ . It is also interesting to note that in the quasi-linear regime ( $\bar{\xi}_2 \lesssim 1$ ), linear perturbation theory predicts a hard limit of  $b = 3/4$  (Fry 1985). Overall, our estimates for  $b$  in the “constant” regime agree well with those from previous (*low* redshift) studies where  $b \simeq 0.62 \pm 0.03$  was measured for IRAS galaxies at  $\lesssim 40h^{-1}\text{Mpc}$  (Sheth et al. 1994) and  $0.4 \lesssim b \lesssim 0.8$  for galaxies in the UGC/ESO catalogs (Lahav & Saslaw 1992) and the Zwicky catalog (Crane & Saslaw 1986; Saslaw & Crane 1991) on  $\lesssim 10h^{-1}\text{Mpc}$  scales. This is not surprising since the angular scales and depths of our samples are expected to probe similar scales (i.e.,  $\lesssim 30h^{-1}\text{Mpc}$ ), albeit to redshifts  $z \gtrsim 1.0$ . This supports the notion of that the galaxy population has remained more or less statistically homogeneous (or in a quasi-equilibrium, semi-relaxed state) since  $z \simeq 1.0$ .

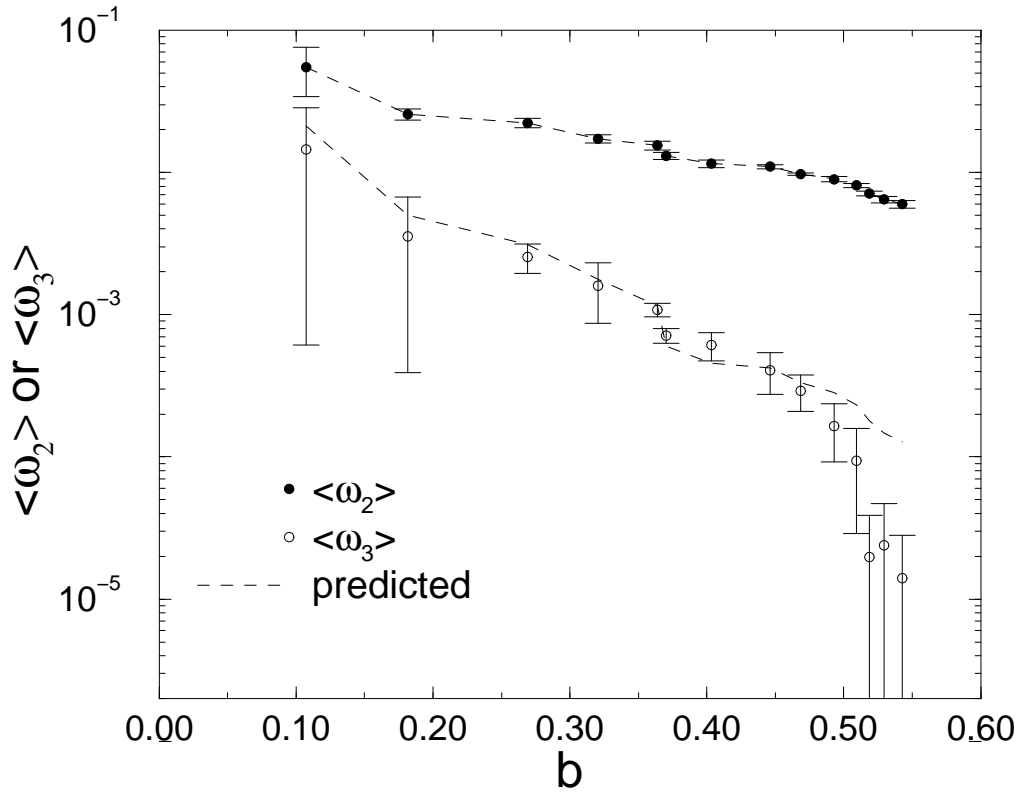


Fig. 9.— Area-averaged two- and three-point correlations as determined from moments of observed counts-in-cells distributions as a function of the fitted parameter  $b = -W/2K$  for the *full* EN1 sample. The dashed curves are predictions derived from moments of the theoretical PDF of Saslaw & Hamilton (1984) (eqs [33] and [34]; see § 4.2).

Recall that from a knowledge of  $\bar{w}_2(\theta)$  and  $\bar{w}_3(\theta)$ , one can derive  $b(\theta)$  and vice versa (e.g., eqs [33] and [34]). In Figure 9, we show actual measured values of  $\bar{w}_2$ ,  $\bar{w}_3$  as a function of  $b$ . From this, it can be seen that larger values of  $b$  do not necessarily mean stronger clustering “in excess” of Poisson sampling as inferred from the  $n$ -point correlations. In fact, we require  $\bar{N}$  to increase with scale faster than  $(1 - b)^{-2}$  in order to keep  $\bar{w}_2$ ,  $\bar{w}_3$  finite. In Figure 9, we also show the values of  $\bar{w}_2$ ,  $\bar{w}_3$  one would obtain directly from the second and third moments of the theoretical CPDF of SH84, given only the fitted  $b$  values (dashed curves). The agreement is very good over the range of angular scales sampled. The discrepancy in  $\bar{w}_3$  at  $b \gtrsim 0.47$  (or  $\theta \gtrsim 0^\circ.6$ ) is due to the skewness estimates being very noisy on these scales, and is most likely due to insufficient sampling. Nonetheless, the parameter  $b$  varies with scale in a manner consistent with the dependence of the two- and three-point correlation functions. This reinforces the fact that the theoretical CPDF of SH84 provides a good description of the observed galaxy distribution.

We summarize the five main points of this section. First, there appear to be significant *non-zero* skewnesses in all observed counts-in-cell distributions on scales  $\theta \gtrsim 0^\circ.1$  (where Poisson effects are expected to be minimal). This supports the LSS paradigm of non-linear gravitational growth of clustering evolved from Gaussian primordial fluctuations. Second, the model of SH84 (eq. [3]) provides a good description of the galaxy distribution over at least an order of magnitude in angular scale. This implies that the three-dimensional galaxy distribution is statistically homogeneous, in quasi-equilibrium and sampled in a representative way to yield *unbiased* two-dimensional distributions. This is reinforced by the similarity in our  $b$  values with those of previous optical/infrared surveys that probe approximately the same volume. Third, comparisons with the previous, shallower studies implies that the galaxy population (selected at optical to far-infrared wavelengths) has remained more or less statistically homogeneous since  $z \simeq 1.0$ . Fourth, values for the virialization parameter  $b$  derived from distribution fits are consistent with those predicted using the observed two- and three-point correlation function estimates and central moments of the SH84 model. This reinforces the generality of the SH84 model. Fifth, the  $b$  values for the *blue* subsamples from all fields are *not consistent* with them being selected at random from their full samples. The higher  $b$  values measured for the blue subsamples are consistent with their higher two-point correlation estimates, and can be explained by redshift-range dependent projection effects affecting the relative angular clustering between the color subsamples.

## 5. Clustering Estimates from Area-averaged Statistics

### 5.1. Angular Two-point Correlation Function

In this section, we estimate the power-law parameters  $(A, \gamma)$  traditionally used for representing the two-point correlation function (eq. [8]). These are estimated using the angular averaged correlations  $\bar{w}_2(\Theta)$ , measured from *counts-in-cells* (eq. [16]) and corrected for the integral constraint bias (eq. [30]).  $\bar{w}_2$  is related to  $(A, \gamma)$  and  $\Theta$  through equation (19), and its derivation is presented in Appendix A. The parameters  $(A, \gamma)$  can be estimated from a *linear* least squares fit to the  $\bar{w}_2$  versus  $\Theta$  data in logarithmic space, i.e., we can re-write equation (19) as

$$y = \alpha + \beta x, \tag{38}$$

where

$$\begin{aligned} y &\equiv \log[\bar{w}_2(\Theta)], \\ x &\equiv \log \Theta, \\ \alpha &\equiv \log \left[ \frac{16}{\pi^2} AC(\gamma) \right], \text{ and} \\ \beta &\equiv 1 - \gamma. \end{aligned} \tag{39}$$

We used a generalized linear  $\chi^2$ -minimization procedure to fit for  $\alpha$  and  $\beta$  in equation (38) which allowed for correlations between the  $\bar{w}_2$  on different scales. Recall that the average two-point correlation estimate from the *counts-in-cells* technique combines information coming from different scales, as opposed to the traditional estimator for  $w_2(\theta)$  where the distribution of angular separations is binned into relatively small intervals. Thus, one does not really measure  $w_2(\theta)$ , but rather its average over the distribution of separations between all possible pairs of points that lie within a cell,  $\bar{w}_2(\Theta)$ , of diameter  $\Theta$ . Therefore in general, the estimated  $\bar{w}_2$  on different scales are not independent since there is significant overlap amongst the randomly thrown cells of different size within the same *finite* survey region. This causes the errors in the  $\bar{w}_2$  estimates at different angular separations to be strongly correlated. If correlations between cells are ignored and only *bootstrapped* variances on the  $\bar{w}_2(\theta_i)$  are used (eq. [23]) in model fitting, then uncertainties on the fitted parameters  $(A, \gamma)$  are likely to be severely overestimated. Furthermore, ignorance of correlations will affect values of the expected  $\chi^2$  and the best fit parameters which minimize it since the variances (and covariances) in  $\bar{w}_2$  for all angular bins represent weights in the  $\chi^2$  function (see below).

The  $\chi^2$  function we minimize, which uses the full error-covariance matrix for  $N$  estimates

of  $\bar{w}_2(\Theta_i)$  at  $N$  different angular scales  $\Theta_i$ , is defined to be

$$\chi^2(\alpha, \beta) = \sum_{k=1}^N \sum_{l=1}^N [y_k - \alpha - \beta x_k] B_{kl} [y_l - \alpha - \beta x_l], \quad (40)$$

where the variables follow from the definitions in equation (39), i.e.,

$$(x_k, y_k) = (\log \Theta_k, \log \bar{w}_k); \quad (x_l, y_l) = (\log \Theta_l, \log \bar{w}_l), \quad (41)$$

and  $B_{kl}$  are matrix elements of the *inverse* of the covariance matrix  $\mathbf{C}$ :

$$\mathbf{B} \equiv \mathbf{C}^{-1}; \quad C_{kl} \equiv \text{cov}(y_k, y_l). \quad (42)$$

The  $C_{kl}$  therefore represent (co)variances between the logarithmic values of  $\bar{w}_k$  and  $\bar{w}_l$ , corresponding to the logarithmic angular bins  $\log \Theta_k$  and  $\log \Theta_l$  respectively. The elements of  $\mathbf{C}$  are estimated using the bootstrap resampling method (§ 3.4) with 20 realizations for each separate bin, i.e.,

$$C_{kl} \equiv \langle (y_k - \langle y_k \rangle)(y_l - \langle y_l \rangle) \rangle_{\text{realizations}}. \quad (43)$$

Since the parameterization of our power-law model in terms of  $(\alpha, \beta)$  is linear (eq. [38]), the minimization of  $\chi^2$  is analytic, and these parameters (hence  $A, \gamma$ ) can be evaluated explicitly. This procedure is straightforward if  $\mathbf{C}$  has a non-vanishing determinant, or, is far from being singular, since otherwise, the  $\chi^2$  minimization either cannot be performed (in the singular case), or be highly unstable to changes in model parameters (in the quasi-singular case). We computed covariance matrices  $C_{kl}$  from the  $y = \log \bar{w}_2(\Theta)$  estimates and found that the covariance between angular bins is nearly as large as the variances in the single bins for all subsamples. We can quantify this through the correlation coefficient  $\rho(y_k, y_l) = C_{kl} / \sqrt{C_{kk} C_{ll}}$ . We found that typically,  $-0.63 \lesssim \rho \lesssim 0.68$  over  $0^\circ.05 \lesssim \Theta \lesssim 0^\circ.7$ , with the closest (furthest) angular bins exhibiting larger (smaller) correlations. As suggested from the size of these correlations, we also found that the covariance matrices are indeed very close to singular (i.e.,  $\det(\mathbf{C}) \lesssim 10^{-40}$ ), rendering a direct minimization of equation (40) unsuitable. This is no surprise, since generally a singular covariance matrix is a consequence of satisfying the integral constraint over the survey area  $\Omega_S$ :  $\int_{\Omega_S} w_2(\theta) d\Omega = 0$  (§ 4.1). To circumvent this problem, we used a more stable version of equation (40) obtained using the method of principal-component analysis (e.g., Kendall 1980). This method, as well as the procedure used to determine  $(A, \gamma)$  and corresponding uncertainties are described in Appendix B.

Results for the power-law parameters  $(A, \gamma)$  and corresponding 1- $\sigma$  uncertainties for all subsamples are summarized in columns 2 and 3 of Table 2. The correlation amplitudes  $A$  are

in broad agreement with values from optical surveys to  $R \lesssim 23.5$  (e.g., Couch et al. 1993),  $K$ -band surveys to  $K \lesssim 20.5$  (Roche et al. 2003, and references therein) and the FIRST radio survey to  $f_{1.4\text{GHz}} \gtrsim 1\text{mJy}$  (Magliocchetti et al. 1998). Our amplitude range for the full samples,  $0.6 \lesssim A/10^{-3} \lesssim 1.6$  is also consistent with recent  $3.6\mu\text{m}$  surveys with *Spitzer* (Fang et al. 2004; Oliver et al. 2004; Waddington et al. 2005) over the  $3.6\mu\text{m}$  flux interval  $30\text{--}110\mu\text{Jy}$  (see the  $A$  versus  $3.6\mu\text{m}$  flux plot in Fig. 2 of Fang et al. 2004). This flux interval is consistent with the  $3.6\mu\text{m}$  flux distribution of our  $24\mu\text{m}$  samples (Fig. 2).

Fits of equation (19) using the  $\chi^2$  minimization procedure described above are shown in Figure 10 for the EN1 samples, and in Figure 11 for all full sample fields. As a consistency check, we also computed  $\bar{w}_2(\Theta)$  (dashed line in Fig. 10) using estimates of  $A, \gamma$  from a direct fit of  $w_2(\theta) = A\theta^{1-\gamma}$  to angular correlations derived using a traditional two-point binning method on the full EN1 sample. For this, we used the Landy & Szalay (1993) estimator,

$$w_2(\theta) = \frac{DD - 2DR + RR}{RR}, \quad (44)$$

where  $DD$ ,  $DR$ , and  $RR$  are the normalized number of distinct data-data pairs, data-random pairs and random-random pairs respectively with angular separation  $(\theta, \theta + d\theta)$ . We used angular bins spanning the range  $0^\circ.005$  to  $0^\circ.5$ , and the  $w_2(\theta)$  estimates were corrected (upward) for an integral constraint bias offset of  $\simeq 1.50 \times 10^{-3}$ . A simple Poisson error model was used for the error in each bin,  $\delta w_2(\theta) = \{[1 + w_2(\theta)]/DD\}^{1/2}$  (Hewett 1982). The power-law parameters found for the full EN1 sample from the direct binning method are  $[A = (1.39 \pm 0.51) \times 10^{-3}, \gamma = 1.89 \pm 0.27]$  compared to  $[A = (1.61 \pm 0.05) \times 10^{-3}, \gamma = 1.88 \pm 0.03]$  from *counts-in-cells*. Note that the uncertainties in the direct binning method are likely to be overestimated due to the ignorance of correlations between bins. These estimates are marginally consistent (dashed and solid lines in Fig. 10), implying the two methods more or less converge on the scales of interest.

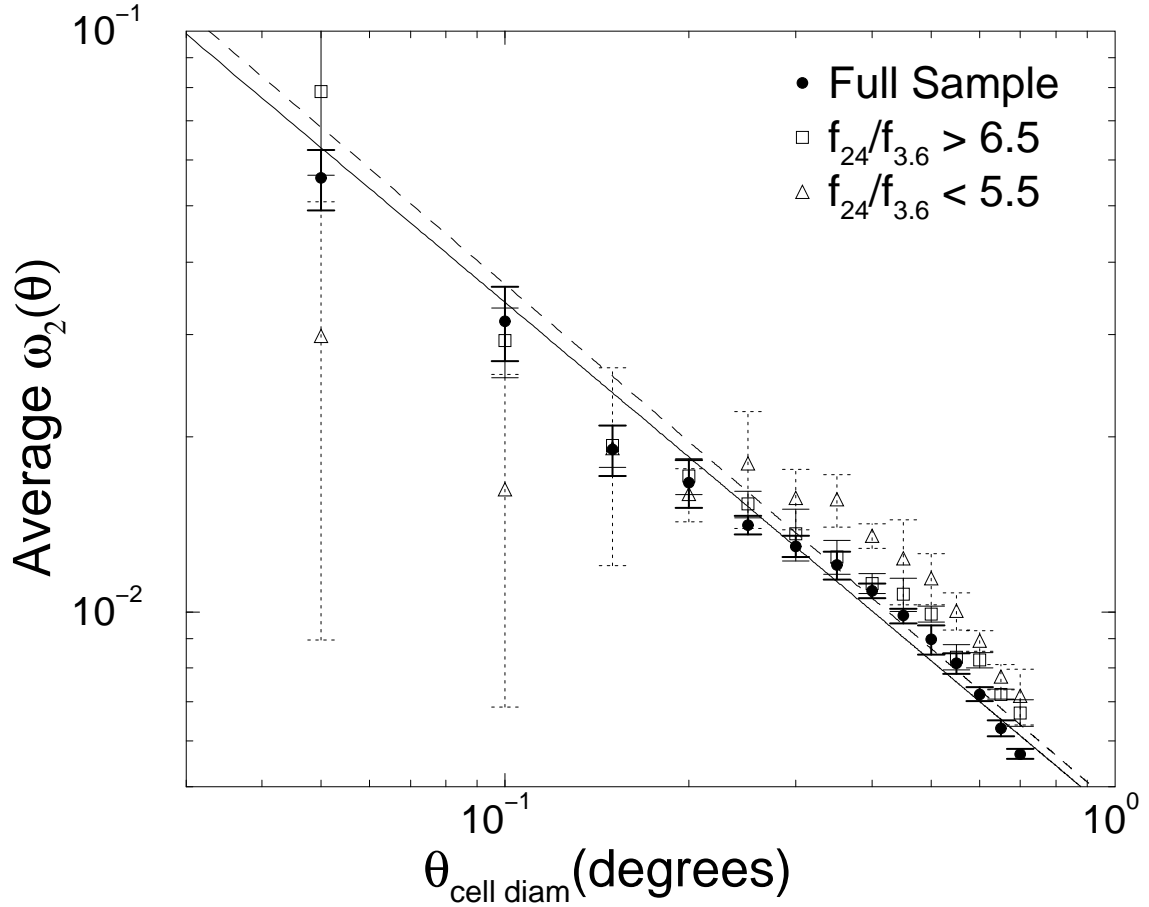


Fig. 10.— Area-averaged two-point correlation function versus cell diameter for subsamples in the EN1 field. The solid line represents a  $\chi^2$ -minimization fit of equation (19) to the *full sample* results, and the dashed line is that predicted using the fit parameters  $[A, \gamma] = [(1.39 \pm 0.51) \times 10^{-3}, 1.89 \pm 0.27]$ , derived using the traditional two-point binning estimator for  $w_2(\theta)$  (eq. [44]). Similar qualitative differences in  $\bar{w}_2(\theta)$  between the *blue* and *red* subsamples are also seen in the EN2 and Lockman fields.

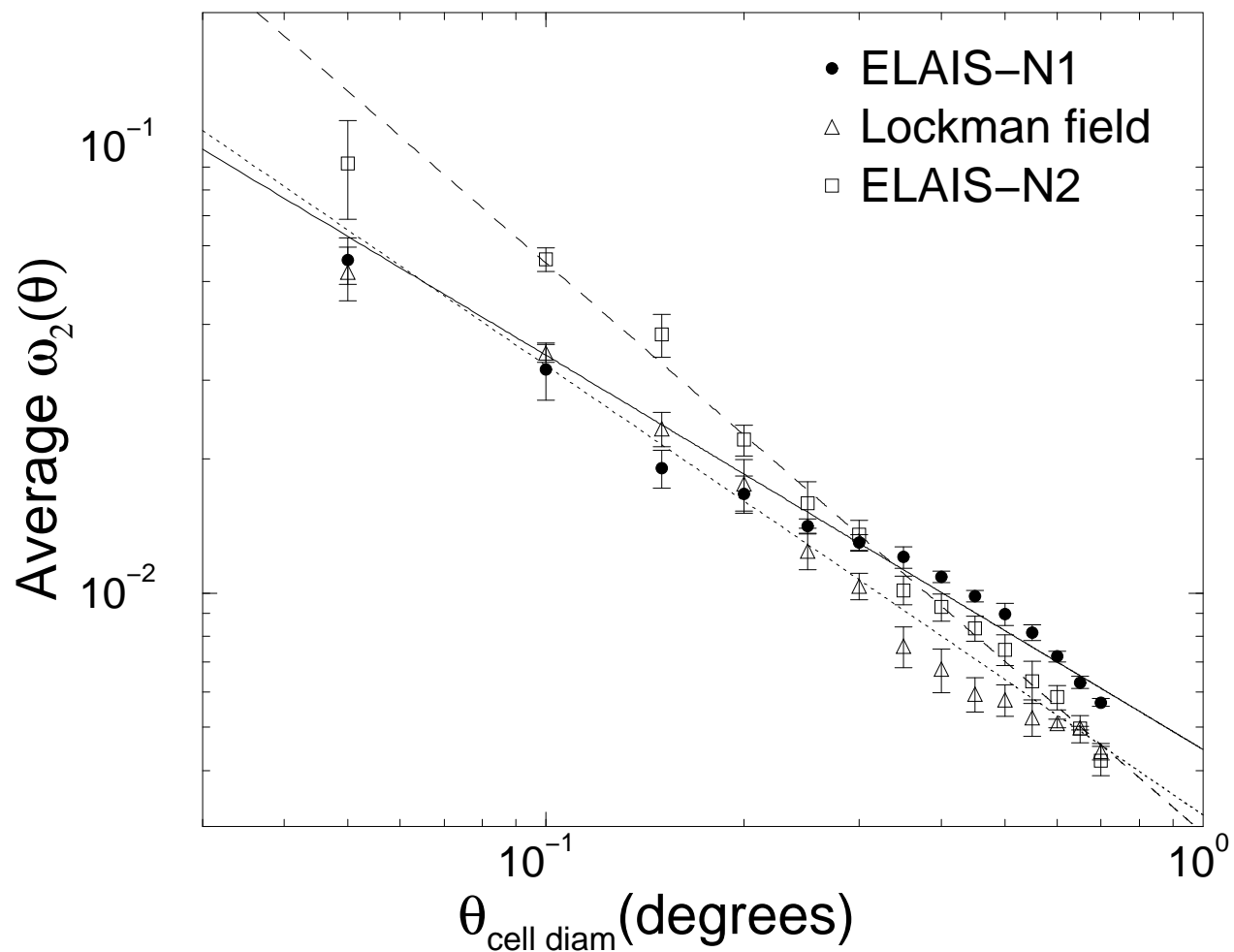


Fig. 11.— Area-averaged two-point correlation functions versus cell diameter across three SWIRE fields (*full samples* with  $f_{24} \geq 450\mu\text{Jy}$ ). Solid, dashed and dotted lines represent  $\chi^2$ -minimization fits of equation (19) to the EN1, EN2 and Lockman data respectively. See Table 2 for fit results.

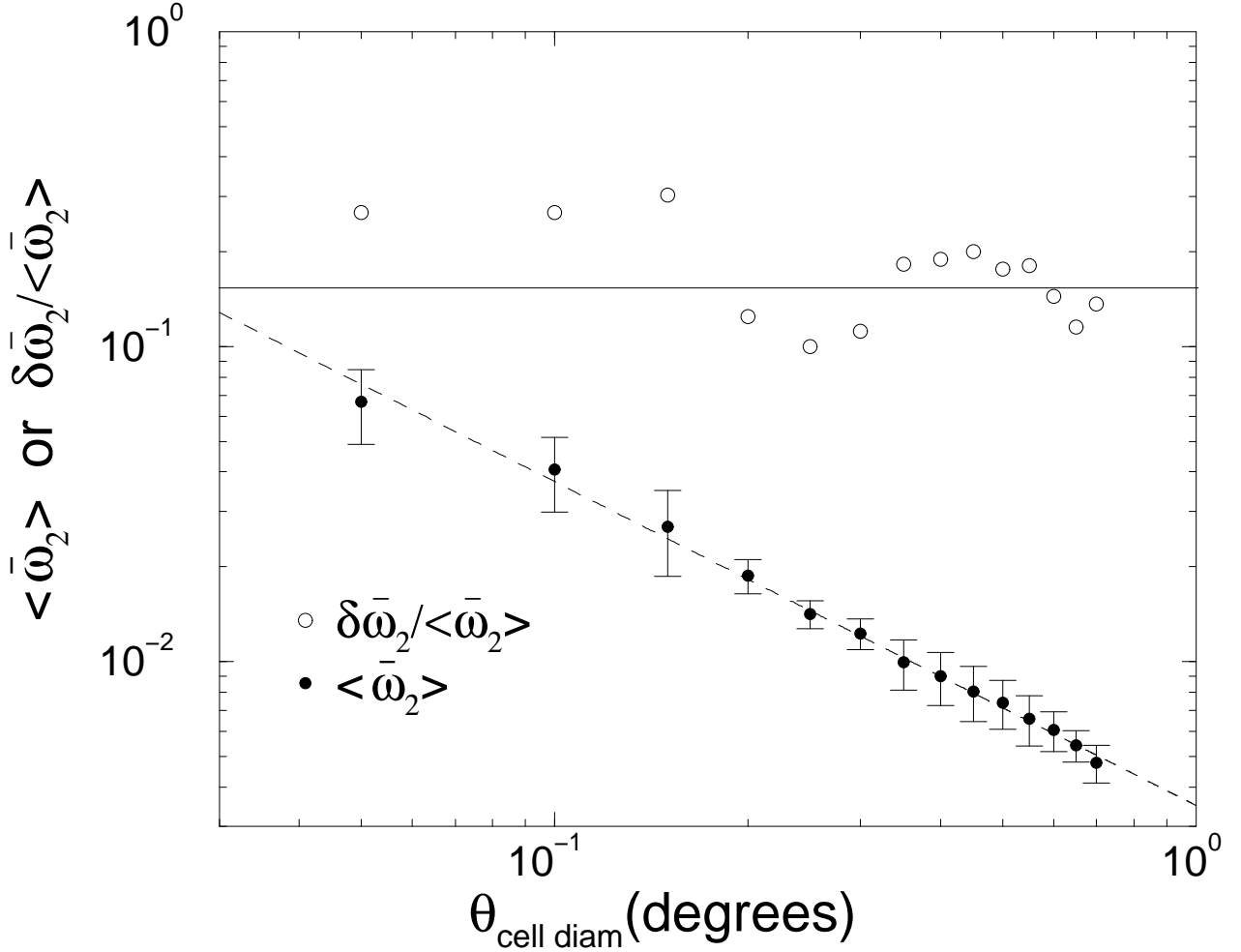


Fig. 12.— *Open circles*: cosmic variance represented by the relative RMS fluctuation in area-averaged two-point correlation over the three SWIRE fields shown in Figure 11. The mean is  $\approx 18\%$  and is indicated by the horizontal solid line. *Solid circles*: the mean area-averaged two-point correlation across all three SWIRE fields. Dashed line represents a  $\chi^2$ -minimization fit of equation (19) yielding  $[A, \gamma] = [(1.05 \pm 0.08) \times 10^{-3}, 2.03 \pm 0.07]$ .

Table 2. Clustering analysis results.

Subsample	$A (\times 10^{-3})^a$	$\gamma$	$\beta^b$	$z_{med}^c$	$r_0 (h^{-1}\text{Mpc})^d$	$r_0 (h^{-1}\text{Mpc})^e$
ELAIS-N1						
$f_{24} \geq 450\mu\text{Jy}$ (full)	$1.61 \pm 0.05$	$1.88 \pm 0.03$	1.00160	0.91, 1.09	$4.86 \pm 0.22$	$6.86 \pm 0.31$
$f_{24}/f_{3.6} \leq 5.5$ (blue)	$2.57 \pm 0.13$	$1.77 \pm 0.07$	1.00238	0.26 ( <i>phot-z</i> )	...	...
$f_{24}/f_{3.6} \geq 6.5$ (red)	$2.33 \pm 0.06$	$1.75 \pm 0.04$	1.00227	0.55 ( <i>phot-z</i> )	...	...
ELAIS-N2						
$f_{24} \geq 450\mu\text{Jy}$ (full)	$0.66 \pm 0.02$	$2.27 \pm 0.03$	1.00110	0.91, 1.09	$4.62 \pm 0.23$	$6.04 \pm 0.30$
$f_{24}/f_{3.6} \leq 5.5$ (blue)	$3.69 \pm 0.15$	$2.05 \pm 0.04$	1.00477	0.26 ( <i>phot-z</i> )	...	...
$f_{24}/f_{3.6} \geq 6.5$ (red)	$0.72 \pm 0.03$	$2.26 \pm 0.03$	1.00145	0.55 ( <i>phot-z</i> )	...	...
Lockman						
$f_{24} \geq 450\mu\text{Jy}$ (full)	$0.95 \pm 0.02$	$2.01 \pm 0.02$	1.00118	0.91, 1.09	$4.35 \pm 0.15$	$5.98 \pm 0.21$
$f_{24}/f_{3.6} \leq 5.5$ (blue)	$6.48 \pm 0.21$	$1.85 \pm 0.03$	1.00731	0.26 ( <i>phot-z</i> )	...	...
$f_{24}/f_{3.6} \geq 6.5$ (red)	$0.36 \pm 0.02$	$2.57 \pm 0.04$	1.00025	0.55 ( <i>phot-z</i> )	...	...

<sup>a</sup>Correlation amplitude on one degree scales. All errors are  $1\sigma$ .

<sup>b</sup>Integral constraint bias correction parameter (see § 4.1).

<sup>c</sup>The median redshift for the *full* samples is that predicted by the XU, LAG model redshift distributions respectively, and the *blue* and *red* subsample values are from photometric redshift distributions derived exclusively from the ELAIS-N1 data (see Figure 13).

<sup>d</sup>Assumes the XU model redshift distribution with stable clustering ( $\epsilon = 0$ ; see figure 15).

<sup>e</sup>Assumes the LAG model redshift distribution with stable clustering ( $\epsilon = 0$ ; see figure 15).

## 5.2. Blue versus Red Color Subsamples

The color subsamples, defined on the basis of the *observed* ratios  $f_{24}/f_{3.6} \leq 5.5$  (*blue*), and  $\geq 6.5$  (*red*) are of particular interest, since each is expected to be composed of galaxies exhibiting different levels of star-formation and/or morphologies. Each may therefore exhibit different intrinsic clustering properties and evolution thereof. This section takes a closer look at the relative angular clustering between these subsamples and its relation to their possible morphological mix and redshift distributions.

We examined a subregion of our EN1 field covering  $\simeq 6.6 \text{ deg}^2$  which was also surveyed in the UgrIZ bands (T. Babbedge et al. 2005, in preparation). Our 3.6, 24 $\mu\text{m}$  detections were associated with this optical catalog as discussed in Rowan-Robinson et al. (2005) and Surace et al. (2005). To get some insight into the various galaxy types, we used the results of Rowan-Robinson et al. (2005) who classified sources using a photometric redshift code that allowed for varying amounts of optical extinction in model fits with the latest optical/IR templates. Based on spectral fits to sources with four or more detections in UgrIZ, 3.6 $\mu\text{m}$  and 24 $\mu\text{m}$ , and good  $\chi^2$  values (comprising  $\simeq 81\%$  of the full sample), we found that  $\simeq 14\%$  were well fit with an (elliptical) “E”-type optical template,  $\simeq 70\%$  with spirals,  $\simeq 9.3\%$  with starbursts (SBs) and  $\simeq 6.7\%$  with an AGN optical template. Separating these by  $f_{24}/f_{3.6}$  flux ratio, we find that “E”-type galaxies comprised  $\simeq 20.8\%$  and  $6.5\%$  of the *blue* and *red* subsamples respectively. The remaining proportions consisted of the forementioned types. This is not surprising since early-type galaxies generally do not exhibit strong mid-IR emission (e.g., see also Yan et al. 2004). The photometric redshift code also reported the “IR-spectral type” from either of the following classes: cirrus dominated galaxies, M82 or Arp 220-like SBs, and AGN tori. For our *blue* (*red*) subsamples in EN1, we found the following proportions of these types respectively:  $\simeq 22\%$  (5%), 47% (60%) and 21% (20%). The remainder could not be classified. It appears that starbursts dominate the near-to-mid IR SEDs to  $f_{24} = 450\mu\text{Jy}$ , and even more so for the *red* subsample.

The top panel in Figure 13 shows *photometric* redshift distributions for the *blue*, *red* and *full* samples in EN1. Rowan-Robinson et al. (2005) broke this down as a function of the optical-SED template classes discussed above, and found the number of sources with E-type best fitting templates exhibited a sharp cutoff at  $z \simeq 1$ , while spirals and SBs extended beyond this. In particular, it is believed that a secondary peak in the distribution at  $z \simeq 0.9$ -1.3 is due to the 10 – 12 $\mu\text{m}$  PAH emission feature and, that a generic cutoff at  $z \simeq 1.4$  is due to redshifted 10 $\mu\text{m}$  silicate absorption. The latter is most pronounced for the *red* subsample, further suggesting that a large fraction of 24 $\mu\text{m}$  sources detected at  $z \gtrsim 0.5$  are dusty SBs. It is important to note the percentage of  $f_{24} \geq 450\mu\text{Jy}$  sources with missing photometric redshifts due to either less than four band-detections or a poor  $\chi^2$  in the template fits is

$\simeq 19\%$ . These photometric redshift distributions are thus not representative of our full  $24\mu\text{m}$  sample. Most of the optically-faint (or non-) detections could be at higher redshift as predicted by various models (see § 6.1). Nonetheless, these distributions are accurate enough to illustrate limiting trends and overall morphological content with redshift of the color subsamples.

Comparing the angular correlation estimates for the *blue* and *red* subsamples across all fields in Table 2, we see that the blue galaxies (as a class) exhibit clustering amplitudes  $\simeq 1.5\text{-}20\times$  greater than the red galaxies. This can be explained by their different redshift distributions as seen in Figure 13. The *blue* subsample angular clustering is less affected by random line-of-sight projections since its members are predominately at low redshift. On the other hand, the *red* and *full* samples which contain galaxies distributed across larger a redshift range will have their angular fluctuations smoothed out. Since the *red* subsample galaxies are detected to slightly higher redshift, this suggests they are a slightly more luminous population than the *blue* galaxies. This is consistent with the near-to-mid-IR color versus mid-IR luminosity correlation found for SBs in the IRAS galaxy surveys (e.g., Carico et al. 1986; Goldader et al. 1997), or the ELAIS (ISO) surveys (Väisänen et al. 2002).

### 5.3. Hierarchical Scaling

As outlined in § 3.5, the hierarchical model of galaxy clustering predicts that the three-point angular-averaged correlation function can be written in terms of the two-point function as  $\bar{w}_3(\Theta) = S_3 \bar{w}_2^2(\Theta)$  (eq. [25]), where the *hierarchical amplitude*  $S_3$  has the property of being scale invariant. This scaling relation is a consequence of the evolution of an initially Gaussian distribution of density perturbations growing under gravity on linear to mildly non-linear scales (see references in § 3.5).

Figure 14 shows the angular-averaged three-point versus two-point correlation function for the *full* EN1 sample. Each estimate is an ensemble average over multiple realizations (i.e.,  $\langle \bar{w}_2 \rangle$  and  $\langle \bar{w}_3 \rangle$ ) with errors estimated using the method of § 3.4. For comparison, we show a linear least-squares fit of  $\bar{w}_3(\theta) = S_3 \bar{w}_2^\alpha(\theta)$  giving  $S_3 = 39.9 \pm 14.2$  and  $\alpha = 2.52 \pm 0.41$  (solid line), and a fit with fixed  $\alpha = 2$ , i.e., the hierarchical model form giving  $S_3 = 3.35 \pm 1.20$  (dashed-line). These fits were performed after discarding data for the four largest angular bins at  $\theta > 0^\circ.5$  where the  $\bar{w}_3$  (skewness) estimates are actually negative and thus, appear to be underestimated when compared to extrapolations from the fits. Over this angular range, the amplitude  $S_3 = \bar{w}_3 / \bar{w}_2^2$  in the EN1 field therefore appears marginally consistent with scale invariance as predicted by the hierarchical model. For the EN2 and LH fields however, the skewness measurements are mostly negative and noisy over all angular bins to allow any

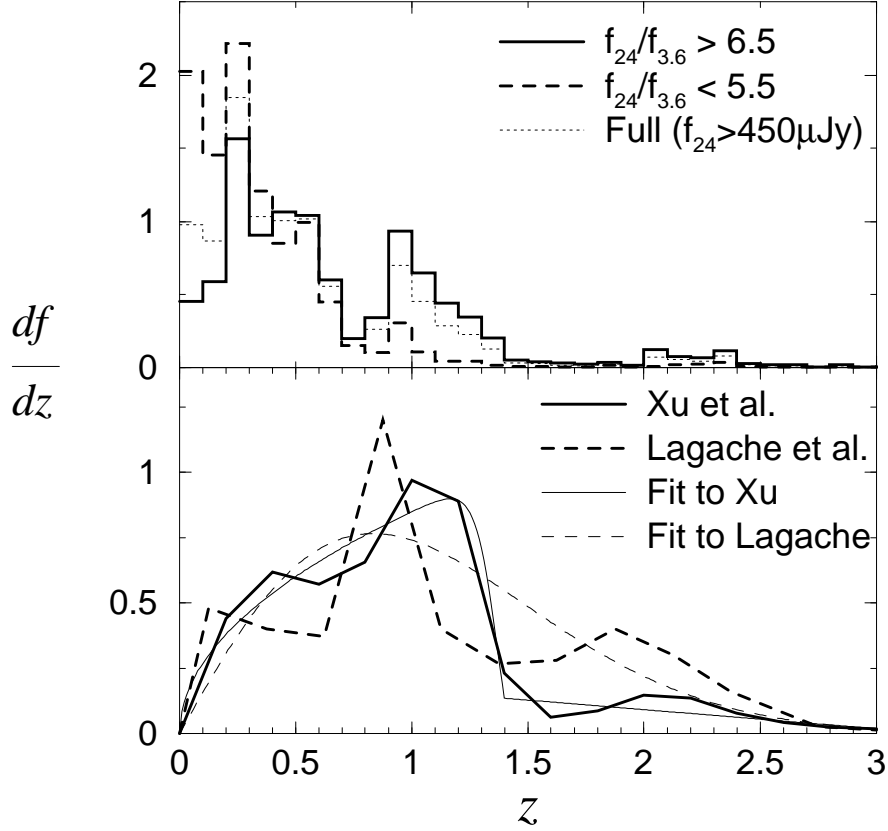


Fig. 13.— *Top panel:* Photometric-redshift distributions for the full and color subsamples in EN1 from the photometric-redshift code of Rowan-Robinson et al. (2005). These are represented as distributions normalized to unity within each subsample. The typical uncertainty in  $z$  is  $\simeq 7\%$ . *Bottom panel:* Model redshift distributions for  $f_{24} \geq 450 \mu\text{Jy}$  from Xu et al. (2003) (*solid thick curve* – “XU” model) and Lagache et al. (2004) (*dashed thick curve* – “LAG” model). Also shown are parametric fits to these model distributions (*thin curves*) as represented by equation (53).

robust test of this model.

One reason for the noisy and/or unreliable  $\bar{w}_3$  estimates is that they were not corrected for the finite-sample biases like those which affect  $\bar{w}_2$  (e.g., see § 4.1), or non-linear biases such as the “ratio bias” which arises from the fact that  $\langle \bar{w}_3 \rangle / \langle \bar{w}_2^2 \rangle \neq \langle \bar{w}_3 / \bar{w}_2^2 \rangle$ , where the angle brackets denote ensemble averaging. A more correct (unbiased) estimate for  $S_3$  would have been from  $\langle \bar{w}_3 / \bar{w}_2^2 \rangle$ . The effects of these biases were quantified by Hui & Gaztañaga (1999) using N-body simulations and were shown to be most significant for scales approaching  $\gtrsim 50\%$  a field size. Furthermore, we did not account for correlated errors between the  $\bar{w}_2$  and  $\bar{w}_3$  measurements on different scales in the least-squares fitting. Our goal here was primarily to test qualitatively the hierarchical scaling relation,  $\bar{w}_p \propto \bar{w}_2^{p-1}$  for  $p = 3$ , and it is encouraging to see that this applies in one of our fields over an angular range where the skewness measurements can be considered reliable.

Studies have found that the value of  $S_3$  is very sensitive (and strongly correlated) to both the fitted slope  $\alpha$  and sample depth. A comparison between various angular and redshift catalogs selected from a number of optical and IRAS studies by Hui & Gaztañaga (1999) indicates a range  $1.4 \lesssim S_3 \lesssim 4.3$ , consistent with our result for EN1. The authors attribute the large scatter to the fact that galaxies selected in different ways might be biased differently with respect to the underlying dark matter. Interestingly, if we assume an effective power-spectrum slope  $n = -1.4$  as found for IRAS galaxies (Fisher et al. 1994), second-order perturbation theory (eq. [26]) predicts  $S_3 = 3.26$ , also consistent with our result.

## 6. Deprojection and Spatial Clustering

To a given depth, the angular two-point correlation function  $w_2(\theta)$ , is dependent upon the redshift distribution of the sources,  $N(z)$  as determined from the survey selection function, their 3-dimensional real space clustering,  $\xi(r, z)$ , and the assumed cosmological model. In turn,  $N(z)$  is dependent on the luminosity and number density evolution, and  $\xi(r, z)$  on the clustering evolution of galaxies (both of which could also be correlated). In this section, we use the cosmological Limber equation (Limber 1953) to estimate spatial correlation lengths,  $r_0$ , by deprojecting  $w_2(\theta)$  into  $\xi(r, z)$  assuming model redshift distributions consistent with previous studies, and a simple evolutionary model for clustering. Results are also discussed in comparison to previous studies.

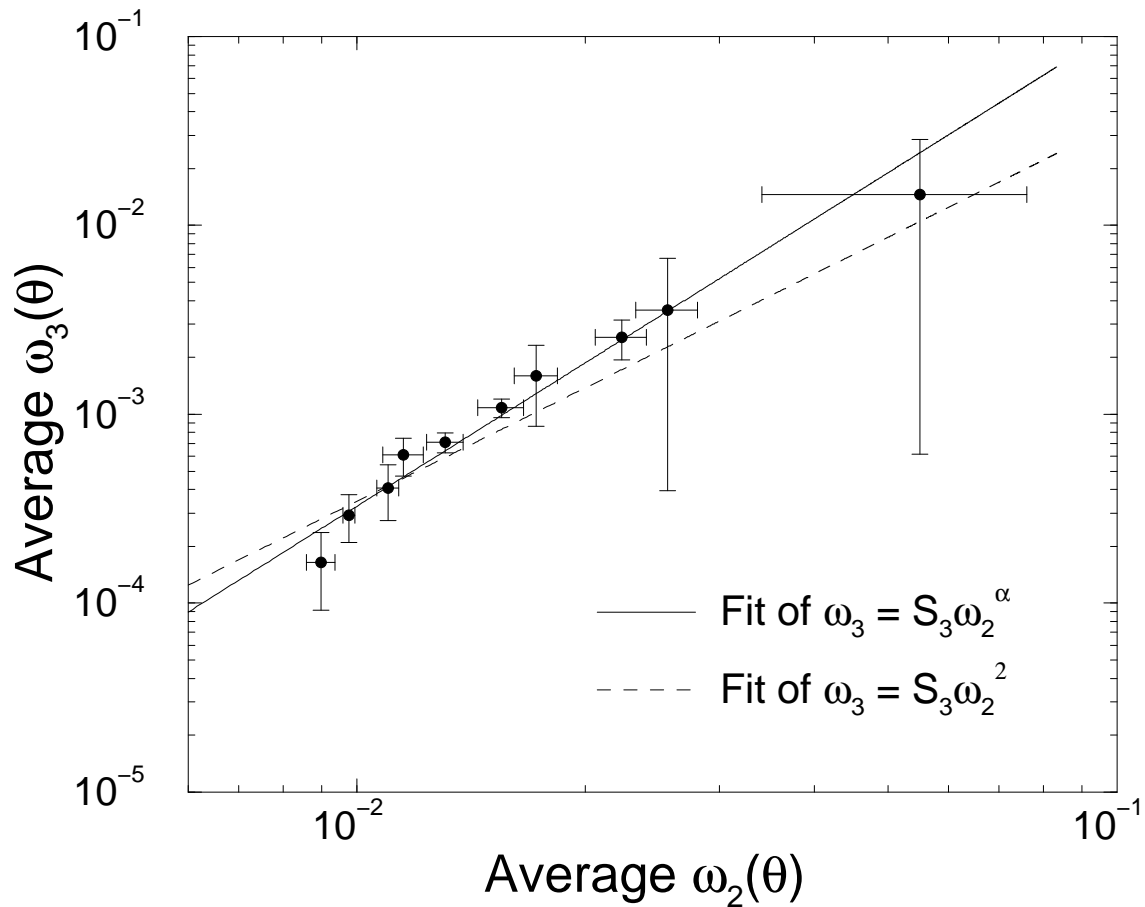


Fig. 14.— Area-averaged three-point versus two-point correlation function for *full* EN1 sample for the angular range  $0^\circ.05 \leq \theta \leq 0^\circ.5$ . The solid line is a linear least squares fit of  $\bar{\omega}_3(\theta) = S_3 \bar{\omega}_2^\alpha(\theta)$  giving  $S_3 = 39.9 \pm 14.2$  and  $\alpha = 2.52 \pm 0.41$ . The dashed line is the hierarchical model fit with fixed  $\alpha = 2$ , giving  $S_3 = 3.35 \pm 1.20$  (see § 5.3).

### 6.1. Inversion of Limber’s Equation

From a multitude of past galaxy surveys, the two-point *spatial* correlation function,  $\xi(r)$ , is well approximated by a power-law of the form  $\xi(r) = (r/r_0)^{-\gamma}$  over  $10h^{-1}\text{kpc} \lesssim r \lesssim 10h^{-1}\text{Mpc}$ . We assume the following parameterization for the evolution of  $\xi(r)$ :

$$\xi(r, z) = \left(\frac{r}{r_0}\right)^{-\gamma} (1+z)^{-(3+\epsilon)}, \quad (45)$$

(e.g., Groth & Peebles 1977) where  $r$  is a *proper* distance,  $r_0$  is a spatial correlation length at  $z = 0$ , and  $\epsilon$  parameterizes the redshift evolution for the clustering (see below for interpretation). We can express  $\xi(r, z)$  in terms of *comoving* coordinates,  $r_c = r(1+z)$ , as

$$\xi(r_c, z) = \left(\frac{r_c}{r_0}\right)^{-\gamma} (1+z)^{\gamma-(3+\epsilon)}, \quad (46)$$

which can be rewritten as

$$\xi(r_c, z) = \left(\frac{r_c}{r_z}\right)^{-\gamma}, \quad (47)$$

where

$$r_z = r_0(1+z)^{1-\frac{3+\epsilon}{\gamma}} \quad (48)$$

is now the *comoving* correlation length at some redshift  $z$ . It is important to note that  $r_0$  is not a physical length scale in the 3D galaxy distribution, but the length at which  $\xi(r) = 1$ . In other words, the chance of finding a galaxy at distance  $r = r_0$  from another galaxy is twice that expected by chance from a random (Poissonian) distribution (cf. eq [7]).

Equipped with an evolution model for  $\xi(r)$  and assuming the parameterization  $w_2(\theta) = A\theta^{1-\gamma}$ , the amplitude  $A$  can be derived from Limber’s functional relation between  $w_2(\theta)$  and  $\xi(r, z)$  (e.g., Phillipps et al. 1978; Loan et al. 1997), giving

$$A = Cr_0^\gamma \frac{\int_0^\infty D^{1-\gamma}(z)g^{-1}(z)(1+z)^{-(3+\epsilon)}(dN/dz)^2 dz}{[\int_0^\infty (dN/dz)dz]^2}, \quad (49)$$

where  $D(z)$  is the angular-diameter distance,  $g(z)$  is the derivative of proper distance with respect to  $z$  (see below), and

$$C = \sqrt{\pi} \frac{\Gamma[(\gamma-1)/2]}{\Gamma(\gamma/2)}. \quad (50)$$

Following previous studies, a crucial assumption leading to the derivation of equation (49) is that angles  $\theta$  subtended by projected galaxy separations,  $D(z)\theta$ , are small. In other words, a physical galaxy separation at  $z$  is approximated as  $r \simeq [u^2 + D(z)^2\theta^2]^{1/2}$ , where  $u$  is the line of sight separation. This approximation assumes  $\cos \theta \simeq 1 - \theta^2/2$ , and is adequate for angular

correlation measurements at  $\theta \lesssim 2^\circ$ .  $D(z)$  and  $g(z)$  depend on the assumed cosmology. We specialize here for the general case of a spatially flat Friedmann-Walker metric with non-vanishing cosmological constant where  $\Omega_m + \Omega_\Lambda = 1$ . For this case, the angular-diameter distance  $D(z)$  and derivative of proper distance with respect to  $z$ ,  $g(z)$  can be written

$$D(z) = \frac{c}{H_0} \frac{1}{(1+z)} \int_0^z dz' [\Omega_m(1+z')^3 + \Omega_\Lambda]^{-1/2} \quad (51)$$

and

$$g(z) = \frac{c}{H_0} [\Omega_m(1+z)^5 + \Omega_\Lambda(1+z)^2]^{-1/2} \quad (52)$$

respectively. We assume  $\Omega_m = 0.3$ ,  $\Omega_\Lambda = 0.7$  and scale all distance measures by  $h^{-1}$  (where  $h = H_0/100 \text{ km s}^{-1} \text{ Mpc}^{-1}$ ) in all calculations.

The evolution parameter  $\epsilon$  (eqs [45]-[48]) can represent a variety of physical clustering models. Three important ones are as follows (e.g., Phillipps et al. 1978). (1) *Stable (constant) clustering in proper coordinates* ( $\epsilon = 0$ ): if galaxy clustering is gravitationally bound on small scales, then clusters have fixed physical sizes (i.e., they neither contract nor expand with  $z$ ) and  $\xi(r_c, z)$  will vary as  $(1+z)^{\gamma-3}$ . Since usually  $\gamma < 3$ , this means  $\xi(r_c)$  will decrease with  $z$ . (2) *Stable clustering in comoving coordinates* ( $\epsilon = \gamma - 3$ ): galaxies and clusters expand with the Universe so that  $\xi(r_c, z) = \text{constant}$ . This case may be a good approximation in a low  $\Omega_m$  Universe where there is not enough gravitational pull to overcome expansion and requires that structures have formed very early. (3) *Growth of clustering* (generally  $\epsilon > 0$ ): more specifically, for linear growth in an Einstein-de Sitter Universe ( $\Omega_m = 1$ ,  $\Omega_\Lambda = 0$ ),  $\epsilon = \gamma - 1$  (Peebles 1980), while for linear growth in a  $\Lambda$ -dominated cosmology, we can only approximate the corresponding value of  $\epsilon$ . For the Einstein-de Sitter case, the linear growth rate of density fluctuations ( $\delta \equiv \delta\rho/\rho$ ) is analytic and given by  $\delta(z) = \delta(0)/(1+z)$ . For  $\Omega_m = 0.3$ ,  $\Omega_\Lambda = 0.7$ , we find that  $\delta(z) \simeq \delta(0)/(1+z)^{0.8}$  to within 6% of the true numerical result over  $0 \lesssim z \lesssim 2$  (Figure 2 in Lahav & Suto 2004). Since  $\xi(r_c, z)$  is by definition  $\langle \delta_i(z)\delta_j(z) \rangle \propto (1+z)^{-1.6}$ , where  $i$  and  $j$  are two cells separated by some comoving separation  $r_c$  at redshift  $z$ , we can identify  $\gamma - (3 + \epsilon) \simeq -1.6$  using equation (46). Thus, linear growth in a  $\Omega_m = 0.3$ ,  $\Omega_\Lambda = 0.7$  cosmology implies  $\epsilon \simeq \gamma - 1.4$ . This means that structure is required to form earlier in a *flat*  $\Lambda$ -dominated cosmology.

It is important to note that the “ $\epsilon$ -models” above (eqs [45]-[48]) only provide a working framework to quantify the relative, on-average rates of clustering evolution between different galaxy subsamples over restricted redshift ranges. They have been shown to be inconsistent with predictions from N-body  $\Lambda$ CDM simulations and semi-analytic models which primarily trace clustering of the underlying mass. Studies have shown that the observed clustering evolution is a strong function of the evolution in galaxy biasing, halo mass, and non-linear processes operating on small scales (e.g., Benson et al. 2001; Somerville et al. 2001). In

general, the simulations show that the correlation length (in comoving units) is expected to decrease at first with increasing redshift to  $z \simeq 1.5$ , imitating  $\epsilon \simeq 0$ , but then increases again thereafter following a  $\epsilon \simeq -1.4$  trend (Baugh et al. 1999). No single  $\epsilon$  can therefore parameterize the evolution. These predictions are consistent with Hubble Deep Field (HDF) observations probing  $0 \lesssim z \lesssim 4.5$  (Connolly et al. 1998; Arnouts et al. 1999), a recent study of the clustering of red galaxies in the Wide-Field Survey to  $z \simeq 1$  (Brown et al. 2003), QSOs to  $z \simeq 2.5$  (Croom et al. 2001), and a multitude of other studies as summarized by Foucaud et al. (2003). Overall, observations and models indicate a slow-to-moderate rate of evolution over  $0 \lesssim z \lesssim 2$  in *comoving* coordinates, all bracketing  $-1.2 \lesssim \epsilon \lesssim 0.8$ .

To compute  $r_0$  from equation (49), we need the redshift distribution,  $dN/dz$ , of our sources. We assume two broadly different model redshift distributions from the literature for  $f_{24} \geq 450\mu\text{Jy}$ , which span different redshift ranges. These were generated from empirical “backward” luminosity/density evolution models which use libraries of spectral templates covering UV to IR-submillimeter wavelengths. These models are shown in the *bottom panel* of Figure 13 and are from (Xu et al. 2003, hereafter XU), and Lagache et al. (2004, hereafter LAG). Their median  $z$  values are shown in Table 2. The  $24\mu\text{m}$  source counts as a function of flux predicted by these models appear to be in broad agreement and consistent with *Spitzer* observations (Chary et al. 2004; Marleau et al. 2004; Papovich et al. 2004; Shupe et al. 2005); however, the LAG model appears to be inconsistent with counts from Chary et al. (2004) down to  $\simeq 20\mu\text{Jy}$ . More importantly, as shown by Lagache et al. (2004), the LAG model predicts that the contribution to counts at  $f_{24} \geq 450\mu\text{Jy}$  is from galaxies distributed almost uniformly with redshift to  $z \simeq 2.5$  (see Fig. 13). This is very difficult to reconcile with our available *photometric* redshift data (Fig. 13), even if we allow for its  $\simeq 19\%$  incompleteness. The XU model is likely to provide a better match with this level of incompleteness. We have included the LAG model as an extreme case to explore the dependence of spatial clustering on the assumed  $dN/dz$ . Despite being initially defined from fits to data in the mid-to-far infrared, the XU model also provides excellent fits to source counts at optical, near-infrared, and sub-millimeter wavelengths, further confirming its versatility in reproducing counts over a broad range of galaxy types. Another model worth noting which comes close to the XU model (and covers more or less the same redshift range) is that of King & Rowan-Robinson (2003).

For convenience in carrying out the integrations in equation (49), we have parameterized the shape of the model redshift distributions shown in the *bottom panel* of Figure 13 as

$$\left(\frac{df}{dz}\right)_{\text{XU}} = \begin{cases} 0.85 z \exp[-(4.4 \times 10^{-4}) z^{25.0}] & \text{for } 0 \leq z \leq 1.4 \\ -0.073 z + 0.238 & \text{for } 1.4 < z \leq 3.0 \\ 0 & \text{for } z > 3.0. \end{cases}$$

$$\left(\frac{df}{dz}\right)_{\text{LAG}} = \begin{cases} 1.6 z \exp[-0.77 z^{1.80}] & \text{for } 0 \leq z \leq 3.0 \\ 0 & \text{for } z > 3.0. \end{cases} \quad (53)$$

All these are normalized to unity, i.e.,  $\int_0^\infty (df/dz)dz = 1$ . The actual number of galaxies per unit redshift is then given by

$$\frac{dN}{dz} = \Omega_s \mathcal{N} \left(\frac{df}{dz}\right), \quad (54)$$

where  $\mathcal{N}$  is the mean surface density over a solid angle  $\Omega_s$ . The parameterizations defined in equations (53) are shown in the *bottom panel* of Figure 13.

Note that the predicted correlation amplitude from Limber’s inversion (eq. [49]) is dependent only on the shape of  $dN/dz$  (or  $df/dz$ ), not its normalization. Furthermore, the angular amplitude  $A$  is sensitive to the width (or dispersion) of  $dN/dz$ ,  $\Delta z$ . For faint flux limits for instance,  $dN/dz$  is broader, and thus the clustering signal is diluted because of the large number of randomly projected pairs.  $A$  is therefore approximately inversely proportional to the width of the distribution over which it is averaged:  $A \propto 1/\Delta z$ . This then implies that a fixed value of  $A$  would require stronger intrinsic clustering (larger  $r_0$ ) on average over  $\Delta z$  to offset this dilution as  $\Delta z$  increases. More specifically, equation (49) implies  $r_0 \propto (\Delta z)^{1/\gamma}$ . This dependence will be explored in more detail in the next section.

## 6.2. Inversion Results and Discussion

With a knowledge of  $A$ ,  $\gamma$ ,  $dN/dz$ ,  $\epsilon$ , and a cosmological model, the value of the  $z = 0$  comoving correlation length,  $r_0$ , is directly fixed by equation (49). In Figure 15 we show  $r_0$  as a function of  $\epsilon$  for all three *full* sample fields and assuming the XU and LAG model redshift distributions for inversion of Limber’s equation. The rectangles enclose those regions in  $(r_0, \epsilon)$  parameter space consistent with predictions from N-body simulations, other observational studies (see references in § 6.2 for  $\epsilon$  and Table 3 for  $r_0$ ), and various physical  $\epsilon$ -models as represented by the three broad scenarios in § 6.1. More specifically, the range shown for  $\epsilon$  (for each sample with given  $\gamma$ ) corresponds to  $(\gamma - 3) \lesssim \epsilon \lesssim (\gamma - 1.4)$ . The lower bound represents constant clustering in *comoving* coordinates and the upper bound to linear growth in a  $\Omega_m = 0.3$ ,  $\Omega_\Lambda = 0.7$  cosmological model. These rectangular regions safely bracket our  $r_0$  estimates using the XU and LAG models in all fields.

The trends in Figure 15 can be used to explore the dependencies amongst each of the main model parameters ( $\epsilon$ ,  $r_0$  and  $dN/dz$ ) that are necessary to match our observed angular amplitudes. First, an increasing value of  $\epsilon$  corresponds to an increase in the growth rate of clustering, i.e., towards higher  $z$  the intrinsic clustering becomes weaker relative to  $z = 0$ . This means that we require a larger  $r_0$  value (stronger local clustering) to achieve the same

observed amplitude  $A$  for the same redshift range over which it is averaged. The dependence of  $r_0$  on  $dN/dz$  is a consequence of the  $r_0 \propto (\Delta z)^{1/\gamma}$  scaling for a fixed  $A$  and  $\epsilon$ , where  $\Delta z$  is the effective width of  $dN/dz$  (see § 6.1). This is well illustrated by the LAG  $z$ -model which has a (pseudo-FWHM)  $\Delta z \approx 2$ , compared to  $\Delta z \approx 1.1$ - $1.2$  for the XU model. Overall, a factor of two change in  $\Delta z$  results in an  $\approx 25\%$  change in  $r_0$ , while the same change in  $\epsilon$  results in a  $\lesssim 15\%$  change in  $r_0$  for  $-1.3 \lesssim \epsilon \lesssim 0.5$ . Thus, the inferred intrinsic clustering is most sensitive on the width of  $dN/dz$ .

As was discussed in § 6.1, the LAG  $z$ -distribution model is unlikely to be a good representation for our  $24\mu\text{m}$  selected samples down to  $450\mu\text{Jy}$ . The XU model-predicted  $r_0$  values are in better agreement with the  $(r_0, \epsilon)$  concordant ranges from other studies for all fields (rectangular regions in Fig. 15). Table 2 summarizes the best fitting  $r_0$  values for all *full* samples assuming  $\epsilon = 0$ , i.e., *stable clustering* in proper coordinates. The assumption of stable clustering on which to base our best  $r_0$  estimates is not unreasonable since the physical clustering sampled in this study is on typical scales of  $\simeq 1.8 - 26h^{-1}\text{Mpc}$  over  $0 \lesssim z \lesssim 1.5$  where galaxies may have already virialized and detached from the Hubble expansion. Note that  $r_0$  values for the blue and red subsamples were not estimated due to their uncertain  $z$ -distributions. This will be deferred to a later paper.

Comparing our spatial clustering to that derived exclusively from previous *shallow* surveys (Table 3), we see that our  $r_0$  values for all *full* sample fields,  $r_0 \simeq 4.35 - 4.86h^{-1}$  Mpc (predicted using the XU  $z$ -model), are more consistent with those from mid-to-far IR surveys (e.g., IRAS and ISO) than the optical, which find canonical values of  $r_0 \simeq 5.0 - 5.7h^{-1}$  Mpc. From local samples, the values derived from IR-surveys are lower on average than those derived from optical (and also near-IR) surveys. This is expected since *local* optical surveys contain a significantly higher proportion of early-types which are more strongly clustered (e.g., Loveday et al. 1995), while IR-surveys detect a larger fraction of spirals, such as that reported by the morphological study of an IRAS subsample by de Jong et al. (1984). This distinction in  $r_0$  between IR and optical surveys however disappears amongst deeper ( $z \gtrsim 0.3$ ) flux limited samples, for example, if we compare our results to the optical HDF and CNOC2 surveys or the SWIRE  $3.6\mu\text{m}$  (near-IR) surveys. This is believed (as suggested by Brainerd et al. 1995) to be due to the deeper samples being dominated by bursting gas-rich late-type spirals and irregulars, such as that reported in a number of deep HST surveys (e.g., Driver et al. 1995; Abraham et al. 1996). As discussed in § 5.2, our results of spectro-photometric modelling are indeed consistent with this scenario where  $\simeq 70\%$  of the sources are best fit with spiral galaxy templates in the optical/near-IR, and a majority have IR SEDs resembling cirrus-dominated and starbursting types over  $0 \lesssim z_{\text{phot}} \lesssim 1.5$ . Thus, despite the differences in clustering between *local* optical and IR samples, our results are broadly consistent with those of optical surveys to similar depths, indicating that we are

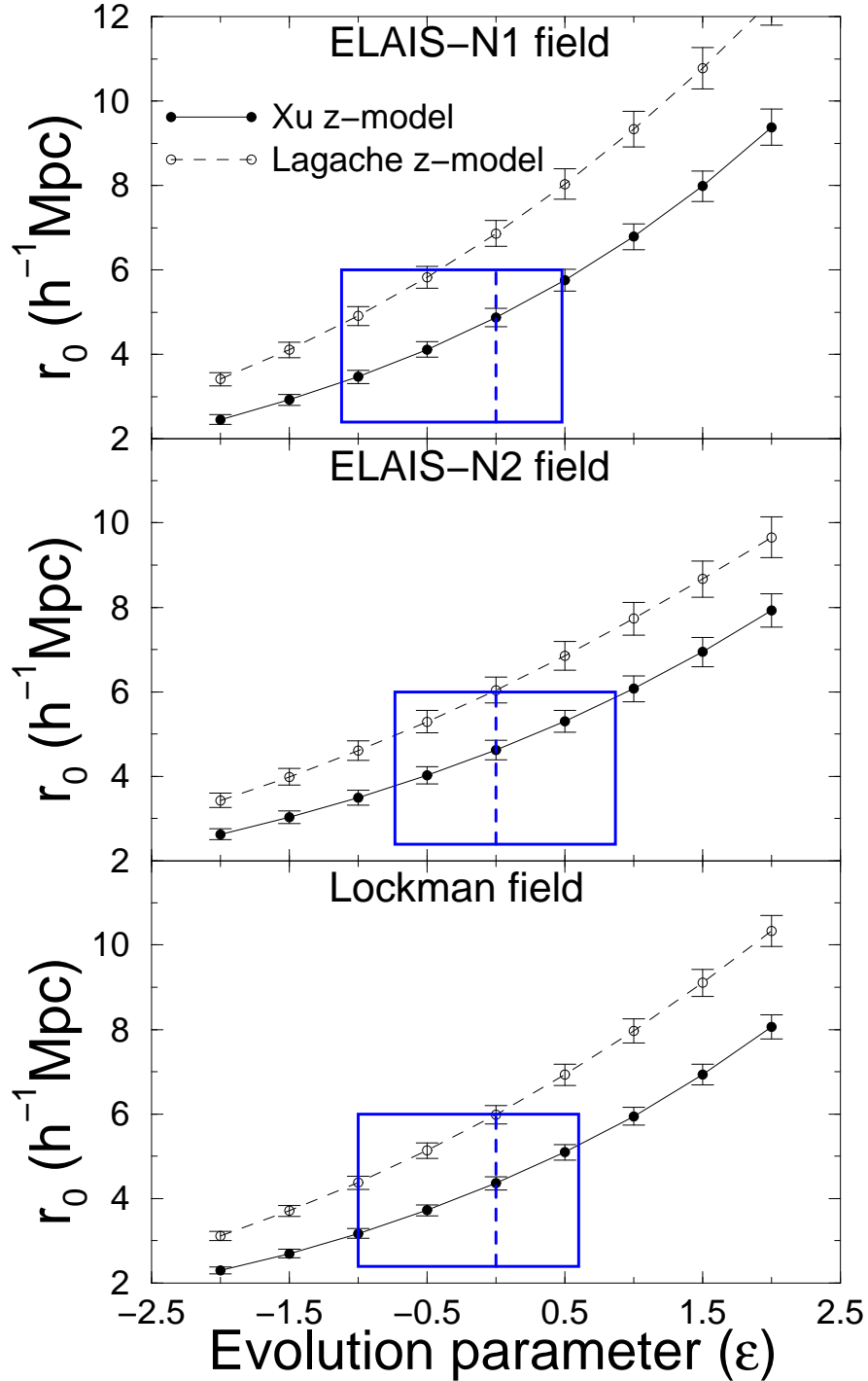


Fig. 15.— Correlation length  $r_0$  as a function of the evolution parameter  $\epsilon$  for the full EN1 (*top*), EN2 (*middle*) and Lockman (*bottom*) samples (all  $f_{24} \geq 450 \mu\text{Jy}$ ). Limber’s equation was inverted using the two model redshift distributions shown in the bottom panel of Figure 13 and parameterized by equations (53). The rectangles enclose regions in  $(r_0, \epsilon)$  parameter space most consistent with predictions from N-body simulations and other observations (see references in § 6.2). The dashed vertical lines delineate  $\epsilon = 0$  (*stable clustering*).

more or less sampling similar (dominant) populations at high redshift.

The redshift range spanned by our sample,  $0 \lesssim z_{phot} \lesssim 1.5$  (with median  $z \simeq 0.9$ ) is expected to probe epochs where a large fraction of gas has not yet been converted into stars, distinct morphological types of the bulk population not yet established, and galaxy clustering much less pronounced. However, despite our sample being considerably deeper than the *local* IRAS surveys, our full sample  $r_0$  estimates are in remarkable agreement under the assumption of stable ( $\epsilon = 0$ ) clustering. Thus, one may conclude this is consistent with no clustering evolution over  $0 \lesssim z_{phot} \lesssim 1.5$ . However, due to the weak dependence of  $r_0$  on  $\epsilon$  for a fixed  $z$ -distribution (see Fig. 15), a range of  $-0.7 \lesssim \epsilon \lesssim 0.2$  is allowed for consistency (within the quoted errors) with local IR surveys. Similar conclusions are reached if we compare our  $r_0$  estimates with the 95% confidence range of  $r_0 = 3.6 - 4.7h^{-1}$  Mpc reported for the ISO  $15\mu\text{m}$  ( $z_{med} \simeq 0.2$ ) ELAIS-S1 survey (Gonzalez-Solares et al. 2004). This sample is of particular interest since our  $24\mu\text{m}$  survey is expected to effectively sample the  $15\mu\text{m}$  rest frame at  $z \simeq 0.5 - 0.7$ , i.e., close to peak of the expected  $f_{24} \geq 450\mu\text{Jy}$  redshift distribution. Indeed, by comparing the near-to-mid IR colors of ISO  $15\mu\text{m}$  sources with a deep  $24\mu\text{m}$  *Spitzer* survey to  $f_{24} \simeq 20\mu\text{Jy}$  ( $z \simeq 3$ ), Chary et al. (2004) show that the  $24\mu\text{m}$  detections are likely to be an extension of the ISO- $15\mu\text{m}$  population seen to  $z \simeq 0.8$ .

Table 3. Comparison of three-dimensional clustering estimates across different surveys.

Survey	$\lambda$ ( $\mu\text{m}$ )	$z_{med}$	$\gamma$	$r_0$ ( $h^{-1}\text{Mpc}$ )
This study <sup>a</sup>	24	0.91	1.88-2.27	4.35-4.86
<i>Spitzer</i> -SWIRE <sup>b</sup>	3.6	0.6(0.75)	$2.03 \pm 0.10$	$3.3(4.4) \pm 0.1$
ISO-ELAIS-S1 <sup>c</sup>	15	0.2	$2.04 \pm 0.18$	$4.3^{+0.4}_{-0.7}$
IRAS <sup>d</sup>	60	0.02	$1.57 \pm 0.03$	$3.79 \pm 0.14$
IRAS-PSCz <sup>e</sup>	60	0.02	1.69	3.7
2dFGRS <sup>f</sup>	0.43	0.08	$1.71 \pm 0.06$	$4.92 \pm 0.27$
SDSS <sup>g</sup>	0.76	0.2	$1.84 \pm 0.02$	$5.77 \pm 0.10$
APM <sup>h</sup>	0.43	0.05	1.67	5.7
CNOC2 <sup>i</sup>	0.60	0.1-0.5	$1.59 \pm 0.08$	$3.95 \pm 0.12$
HDF-N <sup>j</sup>	0.81	0.4-1.6	1.8	$2.37 \pm 0.40$
FIRST <sup>k</sup>	20 <u>cm</u>	$\sim 1.0$	$2.2 \pm 0.1$	$9.7 \pm 0.10$
2dF-QSOs <sup>l</sup>	0.43	1.49	$1.58^{+0.09}_{-0.10}$	$3.99^{+0.34}_{-0.28}$
2dF-QSOs <sup>m</sup>	0.43	1.49	$1.56^{+0.09}_{-0.10}$	$5.69^{+0.42}_{-0.50}$

<sup>a</sup>Quoted  $\gamma$  and  $r_0$  ranges cover our *full* EN1, EN2 and Lockman samples and assume the XU model redshift distribution (see Table 2).

<sup>b</sup>From selected validation fields in the ELAIS-N1 and Lockman fields covering  $\sim 2 \text{ deg}^2$  (Oliver et al. 2004).

<sup>c</sup>Gonzalez-Solares et al. (2004).

<sup>d</sup>Saunders et al. (1992).

<sup>e</sup>Jing et al. (2002) and also independently Fisher et al. (1994)

<sup>f</sup>Norberg et al. (2001).

<sup>g</sup>Budavári et al. (2003).

<sup>h</sup>Maddox et al. (1990).

<sup>i</sup>Shepherd et al. (2001), we quote their results for *late*-type galaxies only.

<sup>j</sup>Connolly et al. (1998), the  $\pm 0.4$  error corresponds to a 95% confidence estimated from their Fig. 3. See also Arnouts et al. (1999).

<sup>k</sup>Magliocchetti et al. (1998).

<sup>l</sup>Croom et al. (2001) assuming  $\Omega_\Lambda = 0.7$ ,  $\Omega_m = 0.3$ .

<sup>m</sup>Croom et al. (2001) assuming an Einstein-de Sitter cosmology.

## 7. Summary, Conclusions and Future Work

We have presented initial results of galaxy clustering at  $24\mu\text{m}$  by analyzing statistics of the projected galaxy distribution from *counts-in-cells*. Our study has focussed on three fields in the SWIRE program, and is the first of its kind at this wavelength and sensitivity. The samples cover separate contiguous areas of 3.98, 6.60 and 8.62  $\text{deg}^2$  and are highly complete down to a  $9\sigma$  sensitivity of  $f_{24} = 450\mu\text{Jy}$ . *Spitzer*-IRAC  $3.6\mu\text{m}$  data were used to correct for stellar contamination and maximize the reliability of detections. The largest sample area probes *comoving* projected scales of  $\simeq 112h^{-1}\text{Mpc}$  at the expected median redshift of 0.9, or a volume of  $\simeq 2.5 \times 10^7 h^{-3}\text{Mpc}^3$  over the expected redshift range  $0 \lesssim z \lesssim 1.5$ . This corresponds to epochs spanning  $\gtrsim 80\%$  of the star-formation history and evolution of LSS in the Universe.

We explored angular clustering statistics using the full samples and subsamples defined by cuts in *observed*  $3.6 - 24\mu\text{m}$  color, paying particular attention to systematic biases from finite sampling and finite field sizes. We compared observed counts-in-cells distributions to predictions of the quasi-equilibrium gravitational clustering model of SH84, and used the second and third moments to explore qualitatively the hierarchical-scaling model. We then estimated power-law fit parameters to angular two-point correlation functions using a numerical method which inverts the angular-averaged variance from counts-in-cells with allowance for covariances between bins. These were then deprojected using empirically derived model-redshift distributions to invert Limber’s equation and obtain estimates of the three-dimensional clustering.

Our main conclusions are as follows:

1. Distributions of counts-in-*circular* cells with diameters in the range  $0^\circ.1 \leq \theta_d \leq 0^\circ.7$  (corresponding to comoving projected scales of  $\simeq 1.8-26h^{-1}\text{Mpc}$  at  $z \simeq 0.9$ ) reveal significant non-Poisson and non-Gaussian behavior in the large mean cell-count limit. Both positive and negative skewnesses are present at the  $> 5\sigma$  level in all full samples on the largest angular scales. The inconsistency in the sign of the skewness between fields can be attributed to cosmic variance, but nonetheless, the levels are consistent with the paradigm of *non-linear* gravitational growth of clustering evolved from Gaussian primordial fluctuations.
2. The quasi-equilibrium gravitational clustering model of SH84 provides a good description of the  $24\mu\text{m}$  galaxy distribution over at least an order of magnitude in scale. This suggests the three-dimensional galaxy distribution is statistically homogeneous, in quasi-equilibrium and sampled in a representative way to yield *unbiased* two-dimensional (projected) distributions. We find values for the “virialization” pa-

parameter  $b = -W/2K$ , i.e., the ratio of gravitational correlation energy to kinetic energy of peculiar velocities of  $\simeq 0.42$ - $0.55$  across all full samples. This is consistent with previous optical/infrared surveys that probe approximately the same volume to  $z \simeq 1.0$  and reinforces the overall statistical homogeneity of the galaxy population. Furthermore,  $b$  is found to vary with scale in a manner consistent with that predicted indirectly from the scale dependence of the observed two and three-point correlations and central moments of the SH84 model distribution.

3. The  $b$  values for the *blue* subsamples are *not consistent* with these samples being selected at random from their full samples. This suggests that the number of galaxies in the environment of a given galaxy depends on its  $3.6 - 24\mu\text{m}$  color *when seen in projection*. The larger  $b$  values for the *blue* subsamples compared to those predicted from random sampling suggests blue galaxies display greater angular variance as a population than the red or full samples. This is consistent with the lower on-average photometric redshifts for blue galaxies since dilution to their angular clustering from random projections is reduced relative to samples spanning a larger redshift range.
4. We assessed the level of *cosmic variance* by comparing statistics and angular correlations across all three SWIRE fields. We found that the mean galaxy count in  $0^\circ.7$  diameter cells randomly placed in each of the fields varied by  $\lesssim 15\%$ , the standard deviations by  $\lesssim 23\%$ , and the mean relative RMS deviation in  $\bar{w}_2(\theta)$  over all angular scales by  $\simeq 18\%$ . This is consistent with the levels of cosmic variance found from number count studies to similar depths, showing that it cannot be neglected when deriving clustering from small area surveys.
5. Values for the two-point correlation power-law fit parameters  $(A, \gamma)$  for all samples were summarized in Table 2. The amplitudes are in broad agreement with those found from optical surveys (e.g., to  $R \lesssim 23.5$ ; Couch et al. 1993), and recent  $3.6\mu\text{m}$  *Spitzer* surveys (Fang et al. 2004; Oliver et al. 2004) to similar depths. This implies that we are probing more or less the same LSS at optical-to-mid-IR wavelengths to this depth, given the available (although weakly constrained) SEDs of the dominant populations.
6. The phenomenological hierarchical-scaling ansatz for gravitational clustering in the linear to mildly non-linear regime,  $\bar{w}_3(\theta) = S_3\bar{w}_2^2(\theta)$ , is marginally satisfied in only the EN1 field where  $S_3 = 3.35 \pm 1.20$ . The skewness estimates in the EN2 and LH field samples are too noisy and unreliable to allow a robust test of this model.
7. We used two (extreme) model redshift distributions: the XU and LAG models (§ 6.1), empirically derived from mid-IR data to infer the three-dimensional clustering from an inversion of Limber’s equation. The  $r_0$  estimates are sensitive to the assumed

$z$ -model, however, the XU-model has attained overwhelming success at reproducing source counts for a broad range of galaxy types from optical to sub-millimeter wavelengths. It also appears closer to the photometric redshift distribution of  $24\mu\text{m}$  sources in EN1, despite the latter being incomplete by  $\simeq 19\%$ . It would be difficult to reconcile these observations with the LAG model. We found spatial correlation lengths of  $r_0 \simeq 4.35$  to  $4.86 h^{-1}$  Mpc across all (full-sample) fields assuming the XU-model and stable clustering in proper coordinates ( $\epsilon = 0$ ). These are smaller than the canonical  $r_0 \sim 5.4h^{-1}$  value derived from shallow optical surveys, but in agreement with results from previous *local* mid-to-far IR surveys (e.g., IRAS and ISO). This agreement is consistent with no clustering evolution over  $0 \lesssim z \lesssim 1.5$ , although it does allow evolutionary rates in the range  $-0.7 \lesssim \epsilon \lesssim 0.2$  for the quoted uncertainties in  $r_0$  across all studies.

8. Our three-dimensional clustering estimates are also consistent with deep optical surveys from HST and near-IR surveys from *Spitzer*. There is widespread belief that these deeper surveys are dominated by bursting gas-rich late-type spirals and irregulars which are intrinsically less clustered. This is consistent with the results of spectro-photometric modelling of our  $24\mu\text{m}$  sources by Rowan-Robinson et al. (2005), where  $\simeq 70\%$  to  $z_{\text{phot}} \simeq 1.5$  are best fit with spiral (late-type) galaxy templates in the optical/near-IR, and with cirrus-dominated and/or starburst-type SEDs in the mid-IR.

The greatest limiting factor in this study has been knowledge of the redshift distribution for estimating the three-dimensional clustering of various subsamples. We have resorted to using simple phenomenological backward evolution models, although these may not be accurate enough to describe the morphological mix of galaxies as a function redshift. This is important since it is becoming more apparent from large area surveys that galaxy clustering is sensitive to the intrinsic properties of the galaxy samples under consideration, including their morphological types, colors, luminosities, and environment.

A more definitive study will be possible when data from all SWIRE fields become available, including more complete redshift information (photometric or otherwise). The sheer number of galaxies will significantly reduce statistical errors and allow us to subdivide samples to probe the dependence of the clustering signal on intrinsic galaxy properties and environment density in much more detail. Good statistics will also allow an estimation of the higher-order moments of the IR-galaxy distribution and their hierarchical scaling for each galaxy type. We will be able to explore the evolution of clustering for different morphological types, relative bias factors, and how IR-luminous matter is related to the underlying dark matter. The preliminary results of this paper, obtained with only  $\approx 1.5\%$  of the total two million galaxies expected in the full SWIRE survey to greater depths, shows the potential of

SWIRE to constrain models of LSS and galaxy evolution at wavelengths and depths never before sampled.

FJM is indebted to John Fowler for proofreading this manuscript and for suggesting the method of principal component analysis in the model fitting procedure. Support for this work, part of the *Spitzer Space Telescope* Legacy Science Program, was provided by NASA through an award issued by the Jet Propulsion Laboratory, California Institute of Technology under NASA contract 1407. We thank the anonymous referee for constructive comments.

### A. Numerical Estimation of $C(\gamma)$

The function  $C(\gamma)$  is used to relate the traditional power-law fit parameters for the parameterization of the two-point correlation function  $w_2(\theta)$  (eq. [8]) in terms of area-averaged correlations as represented by equation (19). Here we provide the derivation leading to equation (19) and method used to compute  $C(\gamma)$ . This function was computed analytically for fixed values of  $\gamma$  by Totsuji & Kihara (1969), and evaluated numerically using Monte Carlo methods by Lahav & Saslaw (1992) for *square cells* only. No closed-form integral representations for  $C(\gamma)$ , however, were provided. We believe the derivation below is not a new result, but is offered for the interested reader because we were unable to find one that can be generalized for any cell shape in the literature. No doubt it exists, but there are times when re-inventing the wheel is the fastest way to proceed.

We start from the integral representation for  $\bar{w}_2(\Omega)$  (see eq. [18]). We discretize this double integral in a rectangular coordinate system as shown by the schematic in Figure 16. Since we considered circular cells in this paper, this integral actually represents a two dimensional sum over all possible *distinct* pairs of solid angle elements  $d\Omega_1$  and  $d\Omega_2$  separated by  $\theta_{12}$  in a region bounded by a circle with some angular diameter  $\Theta_d$ . Without loss in generality, we replace the solid angle elements by projected area elements:  $\Delta A_1 \propto d\Omega_1$  and  $\Delta A_2 \propto d\Omega_2$ , and re-cast equation (18) in terms of a double summation over all elements within a circular region covering an area  $(\pi/4)\Theta_d^2 \propto \Omega$ :

$$\bar{w}_2(\Theta_d) = \frac{16}{\pi^2} A \Theta_d^{-4} \sum_{\Delta A_1} \sum_{\Delta A_2} \theta_{12}^{1-\gamma} \Delta A_1 \Delta A_2. \quad (\text{A1})$$

For a circular region containing  $N$  discrete elements, we will need to sum over a possible total number of  $N(N-1)/2$  distinct pairs of elements  $\Delta A_1$  and  $\Delta A_2$  separated by  $\theta_{12}$ . In

rectangular coordinates (see Figure 16), this separation can be written as:

$$\begin{aligned}\theta_{12} &= [(i\Delta x - i'\Delta x)^2 + (j\Delta y - j'\Delta y)^2]^{1/2} \\ &= \frac{\Theta_d}{N} [(i - i')^2 + (j - j')^2]^{1/2},\end{aligned}\tag{A2}$$

where  $1 \leq [i, j] \leq N$  and  $1 \leq [i', j'] \leq N$  are the cartesian (integer) coordinates of two arbitrary elements and  $\Delta x = \Delta y = \Theta_d/N$ . Furthermore,  $\Delta A_1 \Delta A_2 = (\Delta x \Delta y)^2 = \Theta_d^4/N^4$ , so that combining equations (A1) and (A2), we can write:

$$\bar{w}_2(\Theta_d) = \frac{16}{\pi^2} A \Theta_d^{1-\gamma} C(\gamma),\tag{A3}$$

where

$$\begin{aligned}C(\gamma) &= \frac{1}{N^{5-\gamma}} \sum_{\Delta A_1} \sum_{\Delta A_2} [(i - i')^2 + (j - j')^2]^{(1-\gamma)/2} \\ &\equiv \frac{1}{N^{5-\gamma}} \sum_{i=1}^N \sum_{j=1}^N \sum_{i'=1}^N \sum_{j'=1}^N [(i - i')^2 + (j - j')^2]^{(1-\gamma)/2}.\end{aligned}\tag{A4}$$

The sums in equation (A4) must be evaluated by imposing two relational constraints on the  $i, j, i'$  and  $j'$ : first, we must ensure that we only count *distinct* pairs of cells at coordinates  $(i, j)$  and  $(i', j')$ , i.e., we must satisfy:

$$(i - i')^2 + (j - j')^2 > 0.\tag{A5}$$

and second, since we are working with a circular cell, we must only count pairs whose coordinates  $(i, j)$  and  $(i', j')$  fall within a circular region defined by:

$$\begin{aligned}\left(i - \frac{N}{2}\right)^2 + \left(j - \frac{N}{2}\right)^2 &\leq \left(\frac{N}{2}\right)^2 \quad \text{and} \\ \left(i' - \frac{N}{2}\right)^2 + \left(j' - \frac{N}{2}\right)^2 &\leq \left(\frac{N}{2}\right)^2,\end{aligned}\tag{A6}$$

where  $N$  is the number of elements along a side length of the rectangular grid in Figure 16. The larger the  $N$ , the more accurate will be the estimate for  $C(\gamma)$ .

The computation of  $C(\gamma)$  from equation (A4) can be generalized to any cell shape since all that needs to be defined is the bounded region over which the indices  $i, j, i'$  and  $j'$  are summed (e.g., eq. [A6] for circular cells). For square cells, for example, the bounded region is simply that represented by the square grid in Figure 16. Comparing square to circular cells, we find that the ratio of  $C(\gamma)$  for square cells to that for circular cells,  $R(\gamma) =$

$C(\gamma)_{square}/C(\gamma)_{circ}$ , for some values of  $\gamma$  are:  $R(1.0) = 1.621$ ,  $R(1.8) = 1.460$ ,  $R(2.0) = 1.424$  and  $R(3.0) = 1.303$ . Thus, the assumption of whether square or circular cells are used to estimate correlation amplitudes from counts-in-cells makes a difference of at most  $\simeq 30\%$  for values  $\gamma \simeq 2$ .

Figure 17 shows  $C(\gamma)$  for a  $\gamma$  range extending beyond that commensurate with observations. This was evaluated from equation (A4) (coupled with eqs. [A5] and [A6] for circular cells) assuming  $N^2 = (300)^2$  elements for the base grid in Figure 16. We can get an estimate of the uncertainty in  $C(\gamma)$  by using the fact that  $C(1.0) = (\pi/4)^2 (\approx 0.616850\dots)$  exactly for circular cells, i.e., when  $\gamma = 1$  in equation (A4), this simplifies to the square of the ratio of elements (or area) bounded by a circle to that bounded by a square grid with the same diameter. From the numerical sums, we find that  $C(1.0) \simeq 0.616843$ , implying that our estimates for  $C(\gamma)$  are likely to be good to 1 part in  $10^5$  for the observed  $\gamma$  range.

## B. $\chi^2$ Minimization with Correlated Errors

Here we present the method used to estimate the parameters and uncertainties of our *linear* model:  $(\alpha, \beta)$  where  $y = \alpha + \beta x$  (see eqs. [38] and [39]). As discussed in § 5.1, a determination of these parameters by directly minimizing the  $\chi^2$  function in equation (40) is not possible due to the *quasi-singular* nature of the covariance matrix  $\mathbf{C}$ . The mathematics of linear fits with correlated data points is not new. In fact, Fisher et al. (1994) and Bernstein (1994) have discussed this in the context of fitting models to the two-point correlation function with “bootstrap” derived covariance matrices which in general could be singular, or close to it. We expand on the methods presented therein below.

First, we recast equation (40) in matrix form:

$$\chi^2(\alpha, \beta) = (\tilde{y} - \tilde{y}_m)^T \mathbf{C}^{-1} (\tilde{y} - \tilde{y}_m), \quad (\text{B1})$$

where  $\tilde{y}$  is a column vector of the data  $y_i = y_1 \dots y_N$ , and  $\tilde{y}_m$  the corresponding vector of “expected” model values  $y_{m_i} = \alpha + \beta x_i$ . The first step of *principal component analysis* (PCA; e.g., Kendall 1980) is to find a set of linear combinations of the measured values  $y_i$  which are linearly independent. In other words, the goal is to find a new “basis” (coordinate system) in which correlations are non-existent. This amounts to finding a matrix  $\mathbf{M}$  that diagonalizes the covariance matrix  $\mathbf{C}$ :

$$\mathbf{M}^T \mathbf{C} \mathbf{M} = \mathbf{D}, \quad (\text{B2})$$

where  $\mathbf{D}$  is diagonal. In particular, the symmetry of  $\mathbf{C}$  ( $\equiv \mathbf{C}^T$ ) guarantees the existence of a diagonalizing matrix  $\mathbf{M}$  whose columns form an *orthogonal* set of  $N$  eigenvectors for  $\mathbf{C}$  with corresponding eigenvalues along the diagonal of  $\mathbf{D}$ . Once  $\mathbf{C}$  is diagonalized, the power of

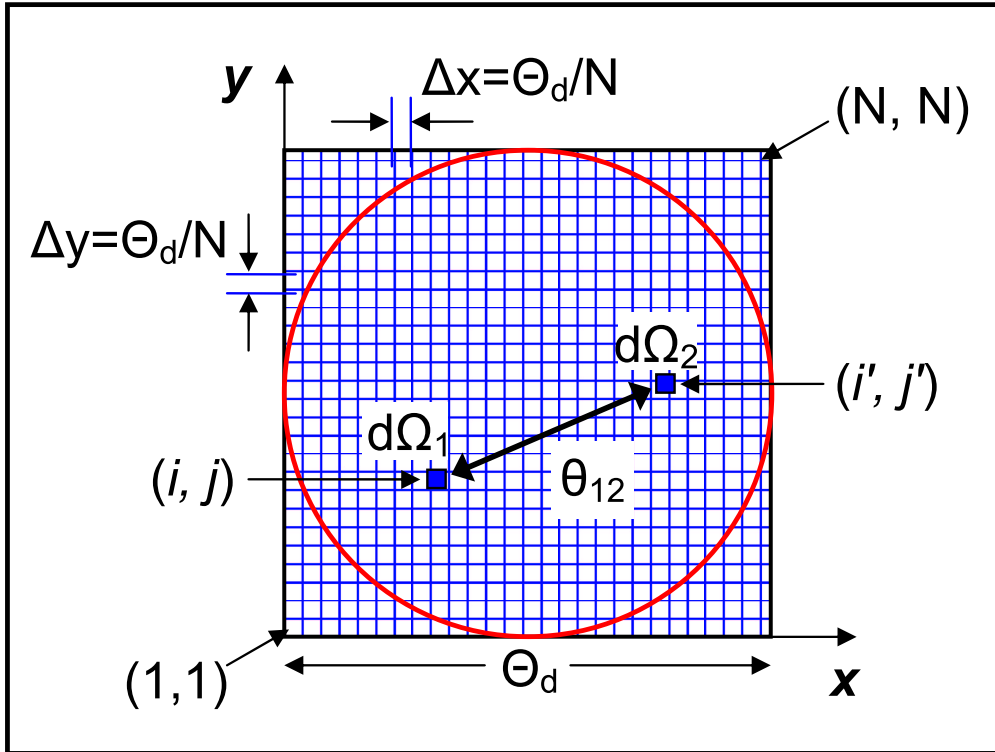


Fig. 16.— Configuration of discretized coordinate system used to solve the double integral in equation (18) for *circular cells*.

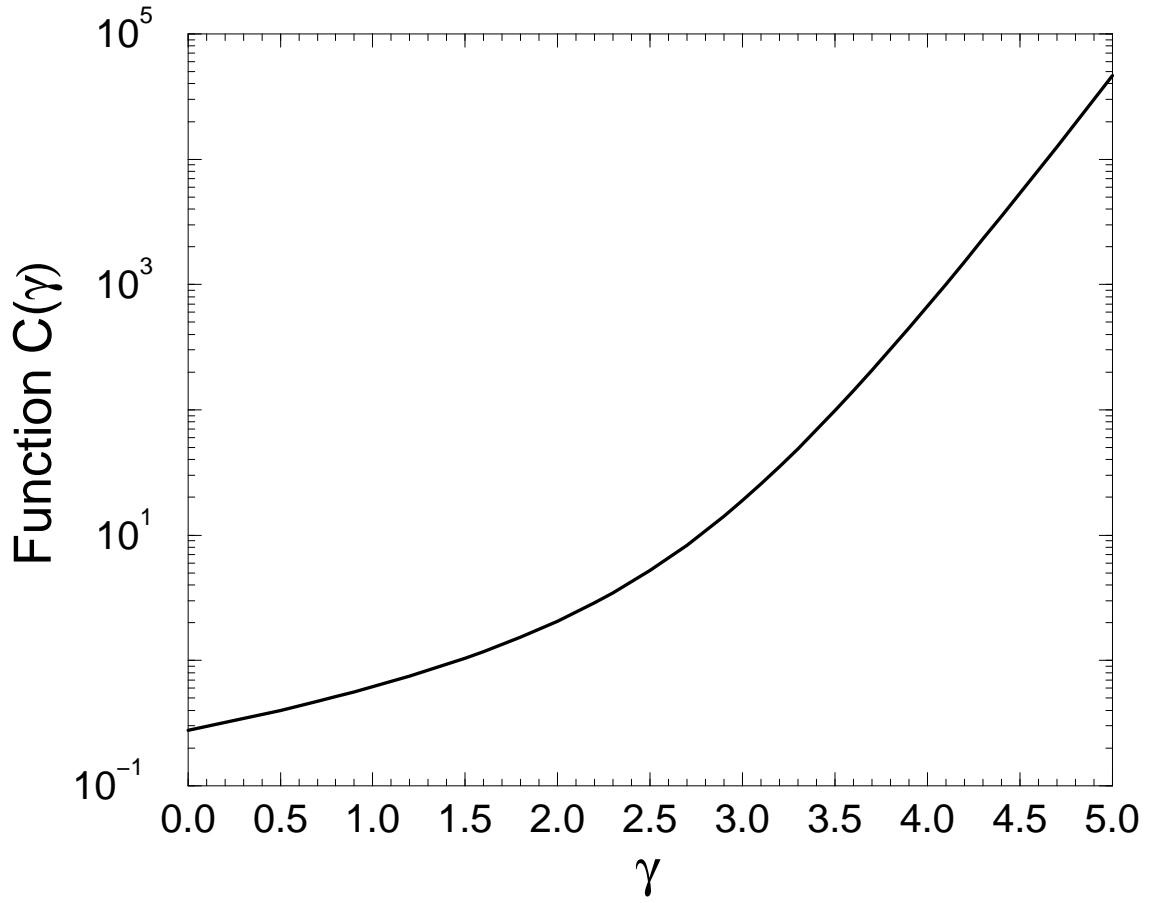


Fig. 17.— The function  $C(\gamma)$  used for the two-point correlation power-law fitting in § 5.1.

PCA is in the second step where we select only those eigenvectors (basis components) which are the most stable, or have relatively large eigenvalues to ensure stability in  $\chi^2$ . This will become more apparent below.

The specific procedure is as follows. If there are  $N$  elements in  $\tilde{y}$ , we form the  $N \times M$  matrix  $\mathbf{M}$  from the  $M$  stable eigenvectors of  $\mathbf{C}$ . We then define a new dataset (of  $M$  “observables”) and corresponding expected (model) values in this new basis,

$$\tilde{z} = \mathbf{M}^T \tilde{y}; \tag{B3}$$

and

$$\tilde{z}_m = \mathbf{M}^T \tilde{y}_m, \tag{B4}$$

respectively, where the new components are guaranteed to be linearly independent with a covariance matrix which is diagonal (i.e., with vanishing covariances) given by  $\mathbf{D}$  (eq. [B2]). We can now define a new “simplified”  $\chi^2$  function,

$$\chi^2(\alpha, \beta) = (\tilde{z} - \tilde{z}_m)^T \mathbf{D}^{-1} (\tilde{z} - \tilde{z}_m). \tag{B5}$$

As discussed above, stability in  $\chi^2$  is ensured by selecting only those eigenvectors of  $\mathbf{C}$  with the largest eigenvalues. The eigenvalues (diagonal elements of  $\mathbf{D}$ ) are also actually the variances for the new dataset  $\tilde{z}$ ,  $\sigma_i^2 \equiv D_{ii}$ . In other words,  $\mathbf{D}^{-1}$  in equation (B5) is none other than

$$\begin{pmatrix} \frac{1}{\sigma^2(z_1)} & 0 & \cdots & 0 \\ 0 & \frac{1}{\sigma^2(z_2)} & \cdots & 0 \\ \vdots & \vdots & \ddots & \vdots \\ 0 & 0 & \cdots & \frac{1}{\sigma^2(z_M)} \end{pmatrix}, \tag{B6}$$

and on expanding equation (B5), the  $\chi^2$  reduces to the simple definition:

$$\chi^2(\alpha, \beta) = \sum_{i=1}^M \frac{[z_i - z_{m_i}(\alpha, \beta)]^2}{\sigma^2(z_i)}. \tag{B7}$$

By selecting the largest eigenvalues (variances), we therefore avoid erroneously inflating  $\chi^2$  and making it unstable against changes in  $\alpha$  and  $\beta$ .

Since the model for  $y_k = \log \bar{w}(\theta_k)$  is linear (eq. [38]), the minimization of  $\chi^2$  is analytic. From equations (B3) and (B4), components of the new data vectors  $\tilde{z}$  and  $\tilde{z}_m$  can be expanded as:

$$z_i = \sum_{k=1}^N M_{ki} y_k, \tag{B8}$$

and

$$\begin{aligned}
 z_{m_i} &= \sum_{k=1}^N M_{ki} y_{m_k} \\
 &= \alpha \sum_{k=1}^N M_{ki} + \beta \sum_{k=1}^N M_{ki} x_k \\
 &\equiv \alpha u_i + \beta v_i,
 \end{aligned} \tag{B9}$$

respectively, where the  $M_{ki}$  represent the matrix elements of the diagonalizing matrix  $\mathbf{M}$  and  $i = 1 \dots M$ . We use  $u_i$ ,  $v_i$  as shorthand notation to represent the coefficient sums of  $\alpha$  and  $\beta$ . Applying the minimization conditions to equation (B7):  $\partial\chi^2/\partial\alpha = 0$ ;  $\partial\chi^2/\partial\beta = 0$ , and solving the simultaneous system for  $\alpha$  and  $\beta$ , we have

$$\begin{aligned}
 \alpha &= \frac{S_1 S_5 - S_3 S_4}{S_2 S_5 - S_3^2}; \\
 \beta &= \frac{S_2 S_4 - S_1 S_3}{S_2 S_5 - S_3^2}; \\
 \sigma_\alpha^2 &= \frac{S_5}{S_2 S_5 - S_3^2}; \\
 \sigma_\beta^2 &= \frac{S_2}{S_2 S_5 - S_3^2}; \\
 \text{cov}(\alpha, \beta) &= \frac{-S_3}{S_2 S_5 - S_3^2},
 \end{aligned} \tag{B10}$$

where the variances and covariance follow from the inverse of the coefficient matrix representing the simultaneous system with determinant  $S_2 S_5 - S_3^2$ . The  $S_n$  are defined by

$$\begin{aligned}
 S_1 &= \sum_{i=1}^M D_{ii}^{-1} u_i z_i \\
 S_2 &= \sum_{i=1}^M D_{ii}^{-1} u_i^2 \\
 S_3 &= \sum_{i=1}^M D_{ii}^{-1} u_i v_i \\
 S_4 &= \sum_{i=1}^M D_{ii}^{-1} v_i z_i \\
 S_5 &= \sum_{i=1}^M D_{ii}^{-1} v_i^2,
 \end{aligned} \tag{B11}$$

where  $u_i$ ,  $v_i$ , and  $z_i$  were defined in equations (B8) and (B9) and as discussed above,  $D_{ii} \equiv \sigma^2(z_i)$  (the diagonal elements of  $\mathbf{D}$ ).

Having determined  $\alpha$  and  $\beta$  (eq. [B10]), the power-law parameters  $A$  and  $\gamma$ , where  $w_2(\theta) = A\theta^{1-\gamma}$  are given by (inverting eq. [39]):

$$A = \frac{\pi^2}{16} \frac{1}{C(\gamma)} \exp(\alpha), \quad (\text{B12})$$

$$\gamma = 1 - \beta. \quad (\text{B13})$$

The variance in  $\gamma$  is simply equal to the variance in  $\beta$  from the above minimization procedure (eq. [B10]),  $\sigma_\gamma^2 \equiv \sigma_\beta^2$ , while the variance in  $A$  is not as straightforward due to the non-linear  $C(\gamma)$  function. Applying standard error propagation to first order in  $\alpha$  and  $C(\gamma)$  in equation (B12), we have the general expression for the variance,

$$\sigma_A^2 = \left(\frac{\partial A}{\partial \alpha}\right)^2 \sigma_\alpha^2 + \left(\frac{\partial A}{\partial C}\right)^2 \sigma_C^2 + 2\text{cov}(C, \alpha) \left(\frac{\partial A}{\partial C}\right) \left(\frac{\partial A}{\partial \alpha}\right), \quad (\text{B14})$$

where  $C = C(\gamma) = C(1 - \beta)$ . The procedure now is to estimate each term in equation (B14). First, we have  $\partial A/\partial \alpha = A$  and  $\partial A/\partial C = -A/C(\gamma)$ . We determine the terms  $\sigma_C^2$  and  $\text{cov}[C(\gamma), \alpha]$  using a local linear approximation:

$$C(\gamma) \simeq \frac{dC(\gamma)}{d\gamma} \gamma + \kappa, \quad (\text{B15})$$

or

$$C(1 - \beta) \simeq \frac{dC(\gamma)}{d\gamma} (1 - \beta) + \kappa, \quad (\text{B16})$$

where  $\kappa$  is a constant which will cancel out later, and

$$\frac{dC(\gamma)}{d\gamma} \approx \frac{C(\gamma_0 + \Delta\gamma) - C(\gamma_0)}{\Delta\gamma}, \quad (\text{B17})$$

which is computed assuming  $\Delta\gamma = 0.1$  for some fitted value  $\gamma_0$ . The covariance term can be written:

$$\begin{aligned} \text{cov}[C(\gamma), \alpha] &\equiv \text{cov}[C(1 - \beta), \alpha] \\ &= \langle C(1 - \beta)\alpha \rangle - \langle C(1 - \beta) \rangle \langle \alpha \rangle. \end{aligned} \quad (\text{B18})$$

Using the functional form for  $C(1 - \beta)$  in equation (B16) and expanding the expectation values in equation (B18),

$$\begin{aligned} \text{cov}[C(\gamma), \alpha] &= -\frac{dC(\gamma)}{d\gamma} [\langle \alpha\beta \rangle - \langle \alpha \rangle \langle \beta \rangle] \\ &\equiv -\frac{dC(\gamma)}{d\gamma} \text{cov}[\alpha, \beta], \end{aligned} \quad (\text{B19})$$

where  $\text{cov}[\alpha, \beta]$  is given by the  $\chi^2$  minimization solution (eq. [B10]). Furthermore, the  $\sigma_C^2$  term can be estimated using:

$$\sigma_C^2 \simeq \left[ \frac{dC(\gamma)}{d\gamma} \right]^2 \sigma_\gamma^2. \quad (\text{B20})$$

Combining equations (B19), (B20) and results for other terms above in equation (B14), we have the final result for the variance in the correlation amplitude,

$$\sigma_A^2 \simeq A^2 \left[ \sigma_\alpha^2 + \frac{1}{C(\gamma_0)^2} \left( \frac{dC}{d\gamma} \right)_{\gamma_0}^2 \sigma_\beta^2 + \frac{2}{C(\gamma_0)} \left( \frac{dC}{d\gamma} \right)_{\gamma_0} \text{cov}(\alpha, \beta) \right], \quad (\text{B21})$$

where the derivative ( $dC/d\gamma$ ) is evaluated at some specific fitted value  $\gamma = \gamma_0$ . Equation (B21) is used to compute the 1- $\sigma$  uncertainty in the correlation amplitude for all subsamples in this paper.

Note that the above  $\chi^2$  minimization procedure (eq. [B7]) does not depend in any way on the errors in the  $y_i$  (or residuals  $z_i - z_{m_i}$ ) being Gaussian. It is only important if one wants to treat the  $\chi^2$  function as having a *true*  $\chi^2$ -distribution (with two degrees of freedom) with a likelihood  $L = \exp(-\chi^2/2)$  for the purpose of setting confidence limits on model parameters, or, to assign a probability for the goodness of fit. Nonetheless, the central limit theorem ensures that the underlying distribution of errors in the original  $\bar{w}_2(\Theta_i)$  will be approximately Gaussian. Assuming that the  $\sigma[\bar{w}_2(\Theta_i)]$  are Gaussian, what about the errors in  $y_i = \log \bar{w}_2(\Theta_i)$ , or, linear combinations thereof (eq. [B8]) used to define the  $\chi^2$  in equation (B7)?

We find that the normalized PDF for the logarithm of a Gaussian random variable  $\bar{w}_{2_i} = \bar{w}_2(\Theta_i)$ , can be written:

$$\begin{aligned} P(y_i) &= \frac{1}{\sqrt{2\pi\sigma^2(\bar{w}_{2_i})}} \exp \left[ y_i - \frac{1}{\sigma^2(\bar{w}_{2_i})} (e^{y_i} - \langle \bar{w}_{2_i} \rangle)^2 \right], \\ &= \frac{1}{\sqrt{2\pi\sigma^2(\bar{w}_{2_i})}} \bar{w}_{2_i} \exp \left[ -\frac{1}{\sigma^2(\bar{w}_{2_i})} (\bar{w}_{2_i} - \langle \bar{w}_{2_i} \rangle)^2 \right], \\ &\approx \langle \bar{w}_{2_i} \rangle G(\bar{w}_{2_i}) \text{ for } \frac{\sigma(\bar{w}_{2_i})}{\bar{w}_{2_i}} \ll 1, \end{aligned} \quad (\text{B22})$$

where the  $\langle \bar{w}_{2_i} \rangle$ , is a boot-strapped ensemble average of some  $\bar{w}_{2_i}$  with variance  $\sigma^2(\bar{w}_{2_i})$ . The last expression follows from the substitution  $y_i = \log \bar{w}_{2_i}$  where  $G(\bar{w}_{2_i})$  is the Gaussian form, and the approximation in the last step is valid when the  $\bar{w}_{2_i}$  are close to their ensemble averages (i.e., the variance is small). At all angular separations, we typically have  $\sigma(\bar{w}_{2_i})/\bar{w}_{2_i} \lesssim 0.05$ , so that this approximation is justified to reasonable accuracy. In fact, we find that the approximation  $P(y_i) \approx \langle \bar{w}_{2_i} \rangle G(\bar{w}_{2_i})$  differs from the true expression for  $P(y_i)$

(first line in eq. [B22]) by at most 10% in the tails, i.e., at  $\gtrsim 3\sigma(\bar{w}_{2i})$ . Since any linear combination of a Gaussian random variable is also Gaussian (e.g., the  $z_i$  in eq. [B8]), we can then treat the simple  $\chi^2$  function in equation (B7) as a *true*  $\chi^2$ -distribution for the purpose of computing goodness-of-fit probabilities and assigning confidence limits.

The quantity in equation (B7) is then distributed like  $\chi^2$  with  $\nu = M - 2$  degrees of freedom about its minimum value. The absolute goodness of fit is given by the probability  $Q(\chi_{min}^2|\nu)$  that some measured realization of the data,  $z_i$ , will yield a  $\chi^2$  which exceeds the observed value  $\chi_{min}^2$  by chance (i.e., expected on the basis of random Gaussian fluctuations alone). This probability is given by the incomplete gamma function (e.g., Press et al. 1999, p. 216):

$$Q(\chi_{min}^2|\nu) = \frac{1}{\Gamma(\nu/2)} \int_{\chi_{min}^2/2}^{\infty} e^{-t} t^{\nu/2-1} dt \quad (\text{B23})$$

For the full sample all subsamples, we have the range  $\nu = 7 - 10$  (or  $M = 9 - 12$  principle components; see above) with  $\chi_{min}^2 \simeq 5.8 - 12.6$  respectively. This range corresponds to  $Q \simeq 0.56 - 0.24$ , indicating that our power-law models for  $\bar{w}_2(\theta)$  are an adequate representation of the data. Also, the values of  $\chi_{min}^2$  are in good agreement with those expected from the  $\chi^2$  statistic, i.e.,  $\langle \chi_{min}^2 \rangle \approx \nu$ , and within standard deviation  $\sqrt{2\nu}$ .

## REFERENCES

- Abraham, R. G., Tanvir, N. R., Santiago, B. X., Ellis, R. S., Glazebrook, K., & van den Bergh, S., 1996, *MNRAS*, 279, 47
- Arnouts, S., Cristiani, S., Moscardini, L., Matarrese, S., Lucchin, F., Fontana, A., Giallongo, E. 1999, *MNRAS*, 310, 540
- Balian, R., & Schaeffer, R. 1989, *A&A*, 220, 1
- Bardeen, J. M., Bond, J. R., Kaiser, N., & Szalay, A. S. 1986, *ApJ*, 304, 15
- Baugh, C. M., Benson, A. J., Cole, S., Frenk, C. S., & Lacey, C. G., 1999, *MNRAS*, 305, 21
- Benson, A. J., Frenk, C. S., Baugh, C. M., Cole, S., & Lacey, C. G. 2001, *MNRAS*, 327, 1041
- Bernardeau, F. 1994, *A&A*, 291, 697
- Bernardeau, F., & Kofman, L. 1995, *ApJ*, 443, 479
- Bernardeau, F., Colombi, S., Gaztañaga, E., & Scoccimarro, R. 2002, *Phys. Rep.*, 367, 1
- Bernstein, G. M. 1994, *ApJ*, 424, 569
- Borgani, S. 1996, in *Dark Matter in the Universe*, Italian Physical Society, Proceedings of the International School of Physics Course CXXXII, ed. S. Bonometto, J.R. Primack, & A. Provenzale (Oxford, GB: IOS Press), 209
- Bouchet, F. R., Strauss, M. A., Davis, M., Fisher, K. B., Yahil, A., & Huchra, J. P. 1993, *ApJ*, 417, 36
- Brainerd, T. G., Smail, I., & Mould, J. 1995, *MNRAS*, 275, 781
- Budavári, T., et al. 2003, *ApJ*, 595, 59
- Brown, M. J. I., Dey, A., Jannuzi, B. T., Lauer, T. R., Tiede, G. P., & Mikles, V. J. 2003, *ApJ*, 597, 225
- Carico, D. P., Soifer, B. T., Beichman, C., Elias, J. H., Matthews, K., & Neugebauer, G. 1986, *AJ*, 92, 1254
- Carruthers, P., & Shih, C. C. 1983, *Phys. Lett. B*, 127, 242
- Chary, R., et al. 2004, *ApJS*, 154, 80

- Coleman, P. H., Pietronero, L., & Sanders, R. H. 1988, *A&A*, 200, 32
- Coles, P., & Frenk, C. S. 1991, *MNRAS*, 253, 727
- Coles, P., & Jones, P. 1991, *MNRAS*, 248, 1
- Coles, P., Moscardini, L., Lucchin, F., Matarrese, S., & Messina, A. 1993, *MNRAS*, 264, 749
- Colless, M., et al. 2001, *MNRAS*, 328, 1039
- Colombi, S., Bouchet, F. R., & Schaeffer, R. 1994, *A&A*, 281, 301
- Connolly, A. J., Szalay, A. S., & Brunner, R. J. 1998, *ApJ*, 499, 125
- Couch, W. J., Jurcevic, J. S., & Boyle, B. J. 1993, *MNRAS*, 260, 241
- Crane, P., & Saslaw, W. C. 1986, *ApJ*, 301, 1
- Crane, P., & Saslaw, W. C. 1988, Proc. of the Twenty-third Rencontre de Moriond (Eighth Moriond Astrophysics Workshop), Dark Matter, (Gif-sur-Yvette, France, Editions Frontieres), 171
- Croom, S. M., Shanks, T., Boyle, B. J., Smith, R. J., Miller, L., Loaring, N. S., & Hoyle, F. 2001, *MNRAS*, 325, 483
- de Jong, T., et al. 1984, *ApJ*, 278, 67
- Driver, S. P., Windhorst, R. A., & Griffiths, R. E. 1995, *ApJ*, 453, 48
- Efstathiou, G., Kaiser, N., Saunders, W., Lawrence, A., Rowan-Robinson, M., Ellis, R. S., & Frenk, C. S. 1990, *MNRAS*, 247, 10
- Fang, F., & Zou, Z. 1994, *ApJ*, 421, 9
- Fang, F., et al. 2004, *ApJS*, 154, 35
- Fazio, G. G., et al. 2004, *ApJS*, 154, 10
- Fisher, K. B., Davis, M., Strauss, M. A., Yahil, A., & Huchra, J. 1994, *MNRAS*, 266, 50
- Fosalba, P., & Gaztañaga, E. 1998, *MNRAS*, 301, 503
- Foucaud, S., et al. 2003, *A&A*, 409, 835
- Fry, J. N. 1985, *ApJ*, 289, 10

- Fry, J. N., & Gaztañaga, E. 1994, *ApJ*, 425, 1
- Gaztañaga, E. 1994, *MNRAS*, 268, 913
- Goldader, J. D., Joseph, R. D., Doyon, R., & Sanders, D. B. 1997, *ApJ*, 474, 104
- Gonzalez-Solares, E. A., Oliver, S., Gruppioni, C., Pozzi, F., Lari, C., Rowan-Robinson, M., Serjeant, S., La Franca, F., & Vaccari, M. 2004, *MNRAS*, 352, 44
- Groth, E. J., & Peebles, P. J. E. 1977, *ApJ*, 217, 385
- Hamilton, A. J. S. 1993, *ApJ*, 417, 19
- Hewett, P. C. 1982, *MNRAS*, 201, 867
- Hubble, E. 1934, *ApJ*, 79, 8
- Huchra, J., Davis, M., Latham, D., & Tonry, J. 1983, *ApJS*, 52, 89
- Hui, L., & Gaztañaga, E. 1999, *ApJ*, 519, 622
- Infante, L. 1994, *A&A*, 282, 353
- Itoh, M., Inagaki, S., & Saslaw, W. C. 1988, *ApJ*, 331, 45
- Jing, Y. P., Börner, G., & Suto, Y. 2002, *ApJ*, 564, 15
- Juszkiewicz, R., Bouchet, F. R., & Colombi, S. 1993, *ApJ*, 412, 9
- Juszkiewicz, R., Weinberg, D., Amsterdamsky, P., Chodorowski, M., & Bouchet, F. R. 1995, *ApJ*, 442, 39
- Kaiser, N. 1984, *ApJ*, 284, L9
- Kendall, M. G. 1980, *Multivariate Analysis* (2nd ed.; London: C. Griffin & Company)
- Kenney, J. F., & Keeping, E. S. 1962, *Mathematics of Statistics*, Pt. 1 (3rd ed.; Princeton, NJ: Van Nostrand), 99
- Kim, R. S., & Strauss, M. A. 1998, *ApJ*, 493, 39
- King, A. J., & Rowan-Robinson, M. 2003, *MNRAS*, 339, 260
- Kofman, L., Bertschinger, E., Gelb, J. M., Nusser, A., & Dekel, A. 1994, *ApJ*, 420, 44
- Komatsu, E. 2003, *ApJS*, 148, 119

- Kurosawa, R., Harries, T., Bate, M., & Symington, N. H. 2004, *MNRAS*, 351, 1134
- Lada, C. J. 1987, in *Proc. IAU Symp. 115, Star Forming Regions*, ed. M. Peimbert, & J. Jugaku (Reidel, Dordrecht), 1
- Lagache, G., et al. 2004, *ApJS*, 154, 112
- Lahav, O., Itoh, M., Inagaki, S., & Suto, Y. 1993, *ApJ*, 402, 387
- Lahav, O., & Saslaw, W. C. 1992, *ApJ*, 396, 430
- Lahav, O., & Suto, Y. 2004, *Living Reviews in Relativity*, 7, 8
- Landy, S. D., & Szalay, A. S. 1993, *ApJ*, 412, 64
- Limber, D. N. 1953, *ApJ*, 117, 134
- Ling, E. N., Barrow, J. D., & Frenk, C. S. 1986, *MNRAS*223, 21
- Loan, A. J., Wall, J. V., & Lahav, O. 1997, *MNRAS*, 286, 994
- Lockman, F. J., Jahoda, K., & McCammon, D. 1986, *ApJ*, 302, 432
- Lonsdale, C. J., et al. 2003, *PASP*, 115, 897
- Lonsdale, C. J., et al. 2004, *ApJS*, 154, 54
- Loveday, J., Maddox, S. J., Efstathiou, G., & Peterson, B. A. 1995, *ApJ*442, 457
- Lucchin, F., Matarrese, S., Melott, A. L., & Moscardini, L. 1994, *ApJ*, 422, 430
- Maddox, S. J., Efstathiou, G., Sutherland, W. J., & Loveday, J. 1990, *MNRAS*, 242, 43
- Magliocchetti, M., Maddox, S. J., Lahav, O., & Wall, J. V. 1998, *MNRAS*, 300 257
- Marleau, F., et al., 2004, *ApJS*, 154, 66
- Moore, B., Frenk, C. S., Efstathiou, G., & Saunders, W. 1994, *MNRAS*, 269, 742
- Moscardini, L., Matarrese, S., Lucchin, F. & Messina, A. 1991, *MNRAS*, 248, 424
- Norberg, P., et al. 2001, *MNRAS*, 328, 64
- Olive, K. A. 1990, *Phys. Rep.*, 190, 307
- Oliver, S., et al. 2004, *ApJS*, 154, 30

- Papovich, C., et al. 2004, *ApJS*, 154, 70
- Peacock, J. A. 2003, *Royal Society of London Transactions Series A*, 361, 2479
- Peebles, P. J. E. 1980, *The Large Scale Structure of the Universe* (Princeton, NJ: Princeton Univ. Press)
- Phillipps, S., Fong, R., Fall, S. M., Ellis, R. S., & MacGillivray, H. T. 1978, *MNRAS*, 182, 673
- Plionis, M., & Basilakos, S. 2001, *MNRAS*, 327, 32
- Press, W. H., Teukolsky, S. A., Vetterling, W. T., & Flannery, B. P. 1999, *Numerical Recipes in C: the art of scientific computing* (2nd ed.; Cambridge, UK: CUP)
- Rieke, G. H., et al. 2004, *ApJS*, 154, 25
- Roche, N. D., Dunlop, J., & Almaini, O. 2003, *MNRAS*, 346, 803
- Rowan-Robinson, M., et al. 1999, in *The Universe as Seen by ISO*, ed. P. Cox & M. F. Kessler (ESA-SP 427), 1011
- Rowan-Robinson, M., et al. 2005, *AJ*, 129, 1183
- Saunders, W., Frenk, C., Rowan-Robinson, M., Lawrence, A., Efstathiou, G. 1991, *Nature*, 349, 32
- Saslaw, W. C., & Hamilton, A. J. S. 1984, *ApJ*, 276, 13 (SH84)
- Saslaw, W. C. 1989, *ApJ*, 341, 588
- Saslaw, W. C., Chitre, S. M., Itoh, M., & Inagaki, S. 1990, *ApJ*, 365, 419
- Saslaw, W. C., & Crane, P. 1991, *ApJ*, 380, 315
- Saslaw, W. C., & Fang, F. 1996, *ApJ*, 460, 16
- Saunders, W., Rowan-Robinson, M., & Lawrence, A. 1992, *MNRAS*, 258, 134
- Schaeffer, R. 1985, *A&A*, 144, 1
- Sharp, N. A., Bonometto, S. A., & Lucchin, F. 1984, *A&A*, 130, 79
- Shepherd, C. W., et al. 2001, *ApJ*, 560, 72
- Sheth, R. K., Mo, H. J., & Saslaw, W. C. 1994, *ApJ*, 427, 562

- Shupe, D. L., et al. 2005, AJ, submitted
- Somerville, R. S., Lemson, G., Sigad, Y., Dekel, A., Kauffmann, G., & White, S. D. M. 2001, MNRAS, 320, 289
- Spergel, D. N. 2003, ApJS, 148, 175
- Surace, J. A., et al. 2005, The SWIRE Data Release 2: Image Atlases and Source Catalogs for ELAIS-N1, ELAIS-N2, XMM-LSS, and the Lockman Hole, (Pasadena: *Spitzer* Science Center), <http://data.spitzer.caltech.edu/popular/swire>
- Szapudi, I., Szalay, A. S., & Boschan, P. 1992, ApJ, 390, 350
- Szapudi, I., Meiksin, A., & Nichol, R. C. 1996, ApJ, 473, 15
- Szapudi, I., & Colombi, S. 1996, ApJ, 470, 131
- Totsuji, H., & Kihara, T. 1969, PASJ, 21, 221
- Väisänen, P., et al. 2002, MNRAS, 337, 1043
- Waddington, I., et al. 2005, to appear in ASP Conf. Ser., The Spitzer Space Telescope: New Views of the Cosmos, ed. Lee Armus (San Francisco: ASP), in press
- White, S. D. M. 1979, MNRAS, 186, 145
- Xu, C. K., Lonsdale, C. J., Shupe, D. L., Franceschini, A., Martin, C., & Schiminovich, D. 2003, ApJ, 587, 90
- Yan, L., et al. 2004, ApJS, 154, 60
- York, D. G. 2000, AJ, 120, 1579
- Zehavi, I. 2004, ApJ, 608, 16
- Zinnecker, H. 1984, MNRAS, 210, 43